Synthesis of noble metal based nanocatalysts for PEM fuel cell applications

Dissertation

Zur Erlangung des akademischen Grades

Doktor der Ingenieurwissenschaften.

(Dr.-Ing.)

Der Technischen Fakultät

Der Christian-Albrecht-Universität zu Kiel

Ayoub Laghrissi

Kiel, 2020

This work was supervised by Prof. Dr. Mohammed Es-Souni, and carried out at the Institute for Materials and Surface Technology/IMST - University of Applied Sciences Kiel

1. Gutachter: Prof. Dr. Franz Faupel

2. Gutachter: Prof. Dr. Mohammed Es-Souni

Tag der mündlichen Prüfung: 16.02.2021

Abstract

Electrocatalysts for energy conversion and power generation systems such as fuel cells are mostly based on Pt-group metals. Because Pt is a strategic metal, is expensive and scarce, any reduction of its load in catalyst electrodes can result in cost-reduction of fuel cells and electrodes for other Pt-catalyzed reactions, e.g. for the hydrogen evolution reaction (HER). This thesis is devoted to the study of 0D and 1D noble-metal-based nanostructures with reduced Pt-load for the electrooxidation of formic acid and methanol, and the HER. The effect of different parameters on the electrocatalytic activity is examined with the aim of reducing the mass loading of platinum-group metals while boosting performance of catalysts.

0D nanoparticles (NPs) are synthesized using sonochemistry in aqueous solutions of noble metal ions and mixtures thereof. With the help of a simple laboratory ultrasonic device nanoparticles of AuPd, and PtPd are deposited on nanocarbon and TiN substrates. The mechanisms of noble metal NP formation on the aforementioned substrates are investigated and discussed in terms of reduction of noble metal ions by organic radicals that form at cavitation- substrate interface. After microscopic and structural characterization, the supported NPs are subsequently used for the electrooxidation of formic acid. It is shown that the electrocatalytic performance very much depends on the nanoalloy composition with AuPd22 nanoalloy exhibiting highest activity of 400 A/g, and a direct reaction path due to the presence of gold that can prevent catalyst poisoning with CO.

Crossing over the dimensionality, 1D nanostructures of different morphologies and chemistries were processed with the aim to boost electrocatalytic activities still more. Self-standing layered Au/Pd/Au and Au/Pd nanorods with different Pd-layer thickness were synthesized using sequential electrodeposition in porous anodic aluminum oxide (AAO) template thin films. It is shown that the electrooxidation of formic acid very much depends on the Pd-layer thickness with thinner layers, down to 15 nm, being most active. This is explained in terms of the formation of near interface AuPd alloys via Pd-diffusion into Au, based on the shift of the PdO reduction peak toward more noble values with decreasing Pd thickness. All the nanostructures show a direct path, suggesting no poisoning of Pd with CO or other carbonaceous species. Density functional theory (DFT)

calculations were conducted, and provide insights into the role of Au as an oxidant of CO adsorbed on Pd in the near-interface alloys.

Pt/C is the best and most widely used catalyst for direct methanol fuel cells (DMFCs) that enjoy an ever-increasing attention for energy conversion. In this thesis, the Pt-loading is reduced first by adopting a nanotube morphology that is realized via electrodeposition at negative voltages, and second by alloying Pt with Pd. These approaches permitted the increase in the electrocatalytic activity to 932 A/g_{Pt} (in 0.5 M H_2SO_4) for an extremely low Pt content of 10 at.% as well as in the electrochemical surface area (ECSA) to 1358 m^2/g. These results are at the upper end of what was published so far, and were achieved via the enormously higher surface area in contact with the electrolyte (nanotube morphology) and the ligand effect (alloying Pt with Pd). The results are rationalized using DFT calculations which show that CO preferentially adsorbs on Pd, thus keeping the active Pt sites free from poisoning species.

Hydrogen production via water electrolysis using wind and solar power is a promising way for energy storage from renewables. Hydrogen is produced from aqueous electrolytes via HER in which noble metal electrocatalysts, prominent among them is Pt, play a key role. In this thesis, Pt and Pd nanostructures, monolithic and supported on Au-NRs, are processed either via electrodeposition or magnetron sputtering, and compared as to their electrocatalytic activity. While the electrodeposited and sputtered monolithic and layered nanostructures show only a moderate activity towards HER, sputtered Pt and Pd on Au-NRs are characterized by a largely higher activity. This is explained by the formation of finely distributed Pt(Pd)-NPs on the entire surface of the Au-NRs thus maximizing the interfacial interaction area between Pt(Pd) and Au. Surprisingly, sputtered Pd on Au-NRs is shown to surpass sputtered Pt on Au-NRs (Pt is known to be the best catalyst for HER). For similar nanostructures, the gravimetric current density measured in 0.5 M H_2SO_4 is 313 $mA/mg.cm^2$ at -0.1 V for Pt against 480 $mA/mg.cm^2$ for Pd. The performance could be boosted still more by choosing longer Au-NRs as supports for Pd. The mechanisms of HER are discussed using Tafel-Plots and Tafel slopes. The sputtered Pd/Au nanostructure is characterized by the lowest Tafel slope suggesting a fast Volmer discharge step followed by a Heyrovsky recombination mechanism. DFT calculations show that the electronic interactions at Pd/Au interfaces lead to a more even hydrogen adsorption energies on all sites considered, in contrast to Au/Pt. This is thought to promote barrier-free hydrogen diffusion and recombination on Au/Pd surfaces, and should explain the higher activity of sputtered Pd/Au nanostructures. Using

the calculated hydrogen adsorption energies and the exchange current densities obtained from the linear sweep voltammograms of all the nanostructures investigated, a volcano plot is suggested.

Kurzdarstellung

Elektrokatalysatoren für Energieumwandlungs- und Stromerzeugungssysteme wie Brennstoffzellen basieren meist auf Metallen der Pt-Gruppe. Da Pt ein strategisch wichtiges, teures und knappes Metall ist, kann jede Verringerung seiner Beladung in Katalysatorelektroden zu einer Kostenreduzierung von Brennstoffzellen und Elektroden für andere Pt-katalysierte Reaktionen führen, z.B. für die Wasserstoffentwicklungsreaktion (HER). Diese Arbeit widmet sich der Untersuchung von 0D- und 1D-Nanostrukturen auf Edelmetallbasis mit reduzierter Pt- Beladung für die Elektrooxidation von Ameisensäure und Methanol sowie der HER. Der Einfluss verschiedener Parameter auf die elektrokatalytische Aktivität wird mit dem Ziel untersucht, die Massenladung von Platingruppenmetallen zu reduzieren und gleichzeitig die Leistung der Katalysatoren zu erhöhen.

0D-Nanopartikel (NPs) werden mittels Sonochemie in wässrigen Lösungen von Edelmetallionen und deren Mischungen synthetisiert. Mit Hilfe eines einfachen Ultraschallgerätes werden Nanopartikel aus AuPd und PtPd auf Nanokohlenstoff- und TiN-Substraten abgeschieden. Die Mechanismen der Edelmetall-NP-Bildung auf den oben genannten Substraten werden im Hinblick auf die Reduktion von Edelmetallionen durch organische Radikale, die sich an der Kavitations-Substrat-Grenzfläche bilden, untersucht und diskutiert. Nach mikroskopischer und struktureller Charakterisierung werden die beladenen NPs anschließend für die Elektrooxidation von Ameisensäure verwendet. Es wird gezeigt, dass die elektrokatalytische Leistung sehr stark von der Zusammensetzung der Nanolegierung abhängt, wobei die AuPd22-Nanolegierung die höchste Aktivität von 400 A/g und einen direkten Reaktionsweg aufgrund der Anwesenheit von Gold aufweist, der eine Katalysatorvergiftung mit CO verhindern kann.

Über die Dimensionalität hinaus wurden 1D-Nanostrukturen unterschiedlicher Morphologie und Chemie mit dem Ziel verarbeitet, die elektrokatalytischen Aktivitäten noch weiter zu steigern. Selbststehende geschichtete Au/Pd/Au- und Au/Pd-Nanostäbchen mit unterschiedlicher Pd-Schichtdicke wurden mittels sequentieller galvanischer Abscheidung in porösen, anodischen Aluminiumoxid (AAO)-Templat-Dünnfilme synthetisiert. Es konnte gezeigt werden, dass die Elektrooxidation von Ameisensäure sehr stark von der Pd-Schichtdicke abhängt, wobei dünnere Schichten, bis zu 15 nm, am aktivsten sind. Dies wird anhand der Bildung von AuPd-Legierungen

in der Nähe der Grenzfläche durch Pd-Diffusion in Au erklärt, basierend auf der Verschiebung des PdO-Reduktionspeaks zu edleren Werten mit abnehmender Pd-Schichtdicke. Alle Nanostrukturen zeigen einen direkten Weg, was darauf hindeutet, dass Pd nicht mit CO oder anderen kohlenstoffhaltigen Spezies vergiftet wird. Es wurden Dichtefunktionaltheorie (DFT)-Berechnungen durchgeführt, die Einblicke in die Rolle von Au als Oxidationsmittel von an Pd adsorbiertem CO in den grenzflächennahen Legierungen liefern.

Pt/C ist der beste und am weitesten verbreiteten Katalysator für Direktmethanol-Brennstoffzellen (DMFCs), die eine immer größere Bedeutung für die Energieumwandlung genießt. In dieser Arbeit wird die Pt-Beladung erstens durch die Annahme einer Nanoröhren-Morphologie, die durch galvanische Abscheidung bei negativen Spannungen realisiert wird, und zweitens durch die Legierung von Pt mit Pd reduziert. Diese Ansätze ermöglichten die Erhöhung der elektrokatalytischen Aktivität auf 932 A/g_{Pt} (in 0,5 M H_2SO_4) bei einem extrem niedrigen Pt-Gehalt von 10 at.% sowie die Erhöhung der elektrochemischen Oberfläche (ECSA) auf 1358 m^2/g. Diese Ergebnisse liegen am oberen Ende dessen, was bisher veröffentlicht wurde und wurden durch die enorm höhere Oberfläche im Kontakt mit dem Elektrolyten (Nanotube-Morphologie) und den Ligandeneffekt (Legierung von Pt mit Pd) erreicht. Die Ergebnisse Konnten durch DFT-Berechnungen erklärt werden, die zeigen, dass CO bevorzugt an Pd adsorbiert und somit die aktiven Pt-Stellen frei von Vergiftungsspezies gehalten werden.

Die Wasserstoffproduktion durch Wasserelektrolyse mit Wind- und Sonnenenergie ist ein vielversprechender Weg zur Energiespeicherung aus erneuerbaren Energien. Wasserstoff wird über HER aus wässrigen Elektrolyten hergestellt, in denen Edelmetall-Elektrokatalysatoren, unter denen Pt prominent vertreten ist, eine Schlüsselrolle spielen. In dieser Arbeit werden Pt- und Pd-Nanostrukturen, monolithisch und auf Au-NRs gestützt, entweder durch galvanische Abscheidung oder Magnetron-Sputtern verarbeitet und hinsichtlich ihrer elektrokatalytischen Aktivität verglichen. Während die galvanisch abgeschiedenen und gesputterten monolithischen sowie geschichteten Nanostrukturen nur eine mäßige Aktivität gegenüber HER zeigen, zeichnen sich gesputterte Pt und Pd auf Au-NRs durch eine wesentlich höhere Aktivität aus. Dies erklärt sich durch die Bildung von fein verteilten Pt(Pd)-NPs auf der gesamten Oberfläche der Au-NRs, wodurch der Bereich für die Grenzflächenwechselwirkung zwischen Pt(Pd) und Au maximiert wird. Überraschenderweise übertrifft gesputtertes Pd auf Au-NRs nachweislich das gesputterte Pt auf Au-NRs (Pt ist bekanntlich der beste Katalysator für HER). Bei ähnlichen Nanostrukturen

beträgt die in 0,5 M H_2SO_4 gemessene gravimetrische Stromdichte 313 mA/mg.cm^2 bei -0,1 V für Pt gegenüber 480 mA/mg.cm^2 für Pd. Die Leistung könnte noch weiter gesteigert werden, wenn längere Au-NRs als Träger für Pd gewählt worden wäre. Die Mechanismen der HER werden anhand von Tafel-Plots und Tafel-Steigungen diskutiert. Die gesputterte Pd/Au-Nanostruktur ist durch die geringste Tafel-Flanke gekennzeichnet, was auf einen schnellen Volmer-Entladungsschritt hindeutet, gefolgt von einem Heyrovsky-Rekombinationsmechanismus. DFT-Berechnungen zeigen, dass die elektronischen Wechselwirkungen an Pd/Au-Grenzflächen im Gegensatz zu Au/Pt zu gleichmäßigeren Wasserstoff-Adsorptionsenergien an allen betrachteten Stellen führen. Dies soll die barrierefreie Wasserstoff-Diffusion und Rekombination an Au/Pd-Oberflächen fördern und die höhere Aktivität gesputterter Pd/Au-Nanostrukturen erklären. Unter Verwendung der berechneten Wasserstoff-Adsorptionsenergien und der aus den linearen Sweep-Voltammogrammen aller untersuchten Nanostrukturen erhaltenen Austauschstromdichten wird ein Vulkan-Plot vorgeschlagen.

Acknowledgements / Danksagung

I would like to sincerely thank Prof. Dr. Mohammed Es-Souni for the opportunity to conduct this research at his institute. In particular, I would like to acknowledge his constant support, focus on my research, guidance, and Attention, which were essential for the successful completion of my thesis. His energy and confidence were driving forces. I really enjoyed working with him.

I would like to thank Prof. Dr. Franz Faupel for taking over the assessment of my research.

I would like to thank Mrs. Christine Boudin, Director of the International Office at the University of Applied Sciences Kiel, for giving me the opportunity to start my research journey in Kiel as Erasmus+ student.

A big thank you to Mr. Claus-Henning Solterbeck, who has taught me immensely. I appreciate his guidance, enthusiasm, and support.

I would like to thank Dr. Thomas Weyrich, for his immense help and for helping me through the abstract translation.

Of course, achieving these work goals would not have been possible without the help of the Institute for Materials and Surface Technology members. I would like to thank Dr. Martha Es-Souni, Dr. Matthias Dietze, and Mr. Andreas Dreher, as well as all my colleagues for their support and friendship. I had a lot of fun working with them, and the working environment was ideal.

Finally, I would like to thank my parents, wife, brothers, and friends for their support during this journey, without which I would not be here today. Thank you for your love, patience, understanding, and the several wonderful hours together.

Table of content

1 Introduction

Nanomaterials form the basis of nanotechnology and exhibit key properties that are significantly different from those on the macroscopic scale, leading to the development of nanoscience in physics, chemistry, and biology. Nanomaterials demonstrate several applications in wide areas, such as energy, electronics, and medicine [1,2]. Among all nanomaterials, noble-metal nanomaterials exhibit unique properties and high stability, making them more attractive for applications [3-6]. Moreover, noble-metal nanomaterials demonstrate the best electrocatalytic performance for the oxidation of fuels and the production of clean energy. This electrocatalytic activity of noble metals can be exploited in energy-conversion devices such as fuel cells, which convert chemical energy into electric energy, with no pollution, and exhibit efficiency greater than that exhibited by classical energy production [6-9].

Fuel cells, especially proton-exchange membrane (PEM) fuel cells, are thought to be an effective solution for preventing greenhouse gases, where hydrogen fed from a hydrogen source (pure H_2 or a hydrogen-containing solution) is oxidized at one electrode, and oxygen from air is reduced at the other electrode [10]. This oxidation/reduction process is accompanied by charge transfer and subsequently current density arises. Recent studies revealed that in terms of the activity of active-metal electrocatalysts, noble metals are on the top of the volcano-like diagram; in particular, platinum is the most active metal [11], but it is also one of the most expensive, rare electrocatalysts, which limits its use in fuel cells for large-scale applications; hence, there is an increased research interest toward the minimization of fuel cell costs [12-14]. Researchers worldwide are suggesting several solutions to minimize the loading of noble metals and preserve the same activity as that of platinum.

Hydrogen is mainly produced from fossil fuels, natural gas, or hydrocarbons (such as gasoline, methanol, etc.); these production methods afford low-purity hydrogen with a high concentration of impurities (e.g., CO, CO_2, etc.) and require additional purification [15,16]. The use of fossil fuels as a source for hydrogen production limits the advantages of hydrogen as a green energy source, which depends on hydrogen production methods. Electrolysis of water is a green route for hydrogen production via the hydrogen evolution reaction (HER); it is a highly attractive method, which can serve as a powerful technique for energy storage that is clean and sustainable, as well as permit use in even remote and desertic regions.

Electrocatalytic properties of nanomaterials are considerably affected by their size, shape, dimension, and composition [17]. The size of nanomaterials can vary from a few nanometers to hundreds of nanometers, and, as the electrocatalytic activity of nanomaterials is related to the nanomaterial surface, a small size leads to the increased surface per mass of the nanomaterial. In addition, the shape of the nanomaterials plays a prominent role in their activity. The use of nanotubes instead of nanorods can double the active surface of the electrocatalysts [18]. The use of porous structures also leads to the considerable improvement in the electrocatalytic properties [19]. Nanomaterials can be classified as 0D (i.e., nanospheres, nanocubes, nanostars), 1D (i.e., nanotubes, nanowires, nanorods), and 2D (i.e., thin layers) materials. The ability of 1D nanostructures to grow in an anisotropic manner permits the exposition of low index planes (such as 111 and 100 planes), thereby strengthening their activity. Hence, 1D nanostructures are more advantageous than 0D materials, as the cathode and anode in PEMs [20]. The nanostructure composition (i.e., alloys, core–shell structure, layered structures) is another key factor. The ligand effect arises in case of multimetallic nanostructures, which changes the electronic environment of the active materials and decreases the loading of expensive materials.

Nanomaterials can be prepared by two approaches: Top-down (lithography) and bottom-up (electrodeposition, physical vapor deposition (PVD), chemical vapor deposition, sol-gel, sonochemistry). The top-down approach involves reduction by the successive cutting of a macroscale material to achieve a nanoscale material [21]. The bottom-up approach involves the synthesis of nanomaterials via the stacking of atoms over each other (atom by atom) [21]; this approach is more advantageous than the former one due to its flexibility in controlling the size and shape of nanomaterials. In this thesis, the nanostructures were synthesized by three bottom-up methods: sonochemistry, electrodeposition and magnetron sputtering.

Sonochemistry has been employed in the past and continues to be of immense interest for the processing of nanoparticles of different materials, which occurs in aqueous solutions containing an ionic species, a surfactant, and an alcohol (to facilitate the reduction of noble-metal ions) by using high-power ultrasonic sources [22]. During sonochemistry, the reduction of nanoparticles occurs via the development of cavitation bubbles in a solution subjected to ultrasonic waves, where high pressure and temperature in this cavitation bubble afford the best conditions for reactions to occur via the use of radicals to reduce metal precursors to nanoparticles. Sonochemistry was well investigated in the past; its general mechanisms are well known and described previously [22].

Another cost-effective method is the direct deposition of nanomaterials in solid templates. The dimension, shape, and homogeneity of the nanostructure are controlled by the template. In this work, anodic aluminum oxide (AAO) template thin films were used to grow noble metal nanorods (NRs), layered NRs and nanotubes from aqueous electrolytes. As the electrochemical deposition of nanomaterials into AAO templates was reported in several previous studies [18,23], extension of the method to nanoalloys and porous nanotubes thereof was attempted and successfully achieved from appropriate mixtures of the metal precursors, and a set of suitable deposition parameters. The AAO template manufacturing steps on a substrate (such as glass/silicon) involve the PVD of heterostructures (adhesion layers and an Al layer), followed by Al-layer anodization, pore widening, and barrier layer removal [23-25].

The combination of electrodeposition and PVD was employed to synthesize NR supports for nanocatalysts. Subsequently, the NR supports were introduced into a sputtering chamber, where small quantities of target materials (nanocatalysts) were magnetron-sputtered under argon. Magnetron sputtering led to nanoparticle formation and their distribution on top and lateral surfaces of the NR support, thus maximizing the interfacial contact between the support and nanocatalyst.

Nanostructures are characterized by several techniques, including scanning electron microscopy, X-ray diffraction, and energy-dispersion spectroscopy. Electrochemical characterization includes cyclic voltammetry and polarization.

For the in-depth understanding of the electrocatalytic behavior resulting from different nanostructures, the electronic structure of key contributors in the electrocatalytic process should be investigated theoretically. The electronic structure is determined from the resolution of Schrödinger equations for the system (involving interactions between every electron and nuclei in the system) called several body systems. Density functional theory is a powerful tool for reducing the Schrodinger equation problem from a large number of variables to one variable, i.e., density. DFT provides insights into different interactions in materials, particularly charge distribution in systems, and the interaction between materials and the adsorbate, which could be poisoning intermediates (CO) or the active molecule (H). The examination and comparison of changes in the interaction between molecule and materials provide ground explanations for the modification of the electrocatalytic behavior.

The present work is divided into the following chapters:

- Chapter 1: Introduction to the basics of electrocatalysts and the general concept of fuel cells.
- Chapter 2: Presentation of the nanomaterial synthesis methods, i.e., sonochemistry, AAO template preparation, and nanostructure electrodeposition into AAO templates. A brief presentation of different characterization methods.
- Chapter 3: General concept of density functional theory calculation.
- Chapter 4: *"Noble metal NPs and nanoalloys by sonochemistry directly processed on nanocarbon and TiN substrates from aqueous solutions."*
  A. Laghrissi, C.-H. Solterbeck, D. Schopf and M. Es-Souni
  Ultrasonics - Sonochemistry, 2018, 51, 138-144, DOI 10.1016/j.ultsonch.2018.10.034
- Chapter 5: *"Layered Au-Pd-Au nanorod catalysts: Pd-layer thickness effects on catalyst performance."*
  A. Laghrissi and M. Es-Souni
  International Journal of Hydrogen Energy, 2019, 44, 14918-14926, DOI 10.1016/j.ijhydene.2019.04.105
- Chapter 6: *"Porous PtPd alloy nanotubes. Towards high performance electrocatalysts with low Pt-loading."*
  A. Laghrissi and M. Es-Souni
  Catalysis Science & Technology, 2019, 9, 4355, DOI: 10.1039/c9cy01145e
- Chapter 7: *"Au-Nanorods supporting Pd and Pt nanocatalysts for the hydrogen evolution reaction: Pd is revealed a better catalyst than Pt."*
  A. Laghrissi and M. Es-Souni
  *****Under Submission*****

1.1 References

[1] Z. H. Khan, Nanomaterials and Their Applications, *Springer Singapore* (2018), ISBN 9789811062148.

[2] M. H. Chaudhery, Handbook of Nanomaterials for Industrial Applications, *Elsevier* (2018), ISBN 9780128133514.

[3] Z. Cai, F. Li, M. Rong, L. Lin, Q. Yao, Y. Huang, X. Chen, X. Wang, Novel Nanomaterials for Biomedical, Environmental and Energy Applications, *Elsevier* (2019), ISBN 9780128144978.

[4] T. Pradeep, Anshup, Noble Metal Nanoparticles for Water Purification: A critical review, *Thin Solid Films* 517 (2009) 6441.

[5] I. Capek, Noble Metal Nanoparticles, *Springer Japan* (2017), ISBN 9784431565567.

[6] J. Yang, Noble Metal-Based Nanocomposites: Preparation and Applications, *Wiley* (2019), ISBN 9783527344529.

[7] V. Hasannaeimi, S. Mukherjee, Noble-Metal based Metallic Glasses as Highly Catalytic Materials for Hydrogen Oxidation Reaction in Fuel Cells. *Scientific Reports* 9 (2019) 12136.

[8] N. Farhat, A. Tauseef, S. Ayesha, H. Naveed, Noble Metal Based Alloy Nanoframes: Syntheses and Applications in Fuel Cells, *Frontiers in Chemistry* 7 (2019) 456.

[9] H. Liu, C. Song, L. Zhang, J. Zhang, H. Wang, D. P. Wilkinson, A Review of Anode Catalysis in The Direct Methanol Fuel Cell, *Journal of Power Sources* 155 (2006) 95.

[10] V. Mehta, J. S. Cooper, Review and Analysis of PEM Fuel Cell Design and Manufacturing, *Journal of Power Sources* 114 (2003) 32.

[11] H. Wendt, E. V. Spinacé, A. oliveira neto, M. Linardi, Electrocatalysis and Electrocatalysts For Low Temperature Fuel Cells: Fundamentals, State of The Art, Research and Development, *Química Nova* 28 (2005) 1066.

[12] Z. Chen, J. -P. Dodelet, J. Z. Dodelet, Non-Noble Metal Fuel Cell Catalysts, *Wiley* (2014) ISBN 9783527333240.

[13] L. Wang, Z. Zeng, C. Ma, Y. Liu, M. Giroux, M. Chi, J. Jin, J. Greeley, C. Wang, *Nano Letters* 17 (2017) 3391.

[14] D. Banham, S. Ye, K. Pei, J. -I. Ozaki, T. Kishimoto, Y. Imashiro, A Review of The Stability and Durability of Non-Precious Metal Catalysts for The Oxygen Reduction Reaction in Proton Exchange Membrane Fuel Cells, *Journal of Power Sources* 285 (2015) 334.

[15] M. El-Shafie, S. Kambara, Y. Hayakawa, Hydrogen Production Technologies Overview, *Journal of Power and Energy Engineering* 7 (2019) 1.

[16] S. Z. Baykara, Hydrogen: A Brief Overview on Its Sources, Production and Environmental Impact, *International Journal of Hydrogen Energy* 43 (2018) 10605.

[17] Y. Li, S. Guo, Noble Metal-Based 1D and 2D Electrocatalytic Nanomaterials: Recent Progress, Challenges and Perspectives, *Nano Today* 28 (2019) 100774.

[18] F. I. Dar, S. Habouti, R. Minch, M. Dietze, M. Es-Souni, Morphology Control of 1D Noble Metal Nano/Heterostructures Towards Multi-Functionality, *Journal of Materials Chemistry* 22 (2012) 8671.

[19] C. Li, T. Sato, Y. Yamauchi, Electrochemical Synthesis of One-Dimensional Mesoporous Pt Nanorods Using the Assembly of Surfactant Micelles in Confined Space, *Angewandte Chemie International Edition* 52 (2013) 1.

[20] S. Du, C. Koenigsmann, S. Sun, One-dimensional Nanostructures for PEM Fuel Cell Applications, Hydrogen and Fuel Cells Primers, *Elsevier* (2017), ISBN 9780128111123.

[21] N. Kumar, S. Kumbhat, Essentials in Nanoscience and Nanotechnology, *John Wiley & Sons* (2017), ISBN 9781119096115.

[22] H. Xu, B. W. Zeiger, K. S. Suslick, Sonochemical Synthesis Of Nanomaterials, *Chemical Society Reviews* 42 (2013) 2555.

[23] M. Es-Souni, S. Habouti, Ordered Nanomaterial Thin Films via Supported Anodized Alumina Templates, *Frontiers in Materials* 1 (2014) 19.

[24] N. Berger, S. Habouti, H.-G. Rubahn, M. Es-Souni, On-substrate Fabrication Of Porous Al_2O_3 Templates With Tunable Pore Diameters And Interpore Distances, *Applied Physics A* 122 (2016) 192.

[25] N. Berger, M. Es-Souni, Understanding and Shaping the Morphology of the Barrier Layer of Supported Porous Anodized Alumina on Gold Underlayer, *Langmuir* 32 (2016) 6985.

2 Electrocatalysis

2.1 Introduction

Many chemical reactions, even the thermodynamically favorable ones, do not occur at a significant rate on their own. For such a reaction to be beneficial a catalyst is often required, which changes the rate of chemical reactions typically by several orders of magnitude. By definition, a catalyst is a chemical element that is added to speed up a chemical reaction without any chemical change in the catalyst [1]. Catalysis is key to the industrial growth of different chemical technologies (e.g., fuel cells catalysts, pollutant reduction, water splitting, organic synthesis etc.) [2]. Chemical reactions always occur with no catalyst modification or with no significant change. Generally, catalysis reactions are categorized as heterogeneous and homogeneous reactions. In homogeneous catalysis, the catalyst (i.e., acid, base, ions) added into the reaction is in the same phase as that of the reaction components (i.e., gas or single-phase liquid). In contrast, in heterogeneous catalysis, the catalyst is in a phase different from that of the reaction component; a typical example is the addition of a solid catalyst to a liquid or gaseous reactant.

In the following, emphasis will be placed on heterogeneous catalysis as the main subject of this thesis. A majority of heterogeneous catalysis reactions occur following the same process detailed below [3]:

- Reactants are adsorbed on active sites on the catalyst surface.
- Interactions between the active sites and reactants occur, whereby intramolecular bonds are broken and weakened, affording more reactive species.
- The targeted reaction occurs, and the products are desorbed.

A suitable catalyst should adsorb the reactant sufficiently strongly for a reaction to occur, but not all too strong for the product to stick on the catalyst surface. During a heterogeneously-catalyzed reaction, the catalyst is not consumed, but it can be destroyed or deactivated by secondary molecules, mostly intermediate products. Electrochemical catalysis (electrocatalysis) is a particular form of heterogeneously catalyzed reactions. In an electrochemical cell comprising electrodes and an electrolyte the reaction occurs at the electrolyte–electrode (catalyst) interface involving charge transfer in a Redox system (oxidation/reduction).

Electrochemistry covers all technologies involving chemistry and electrical charges, e.g., corrosion, batteries, electrodeposition, and electrocatalysis [4]. The selection of an electrochemical electrode is specific to the desired application of the reaction; in particular, when one of the electrodes is selected as a heterogeneous catalyst, the application is referred to as electrocatalysis, which involves assisting and accelerating a reaction or enhancing the current density at the electrocatalyst active sites. Figure 2.1 shows the schematic of an electrocatalytic system. Electrocatalytic reactions comprise three main steps; first, the reactant is dissolved and adsorbed on the catalyst surface; second, charges are transferred to help in the reaction of the adsorbed elements; finally, the desorption of products occurs.

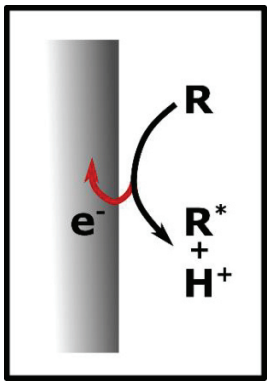

Figure 2.1. Electrocatalytic system comprising heterogeneous electrocatalysts and the reactant.

In heterogeneous catalysis, two main reaction mechanisms are proposed: Langmuir–Hinshelwood and Eley–Rideal mechanisms; in the former mechanism, the species adsorbed on the electrocatalyst surface react with each other [5], while in the latter mechanism, only one reactant is adsorbed and the other reactant is directly sourced from the gas or liquid phase [6]. Figure 2.2 shows the schematic of the electrocatalytic process, which is related to the reaction activation energy, in the presence of the electrocatalysts used to enhance the rate of a reaction (reaction products) or the current density (released energy). Suitable electrocatalysts are those that require low energy for the reactions to occur.

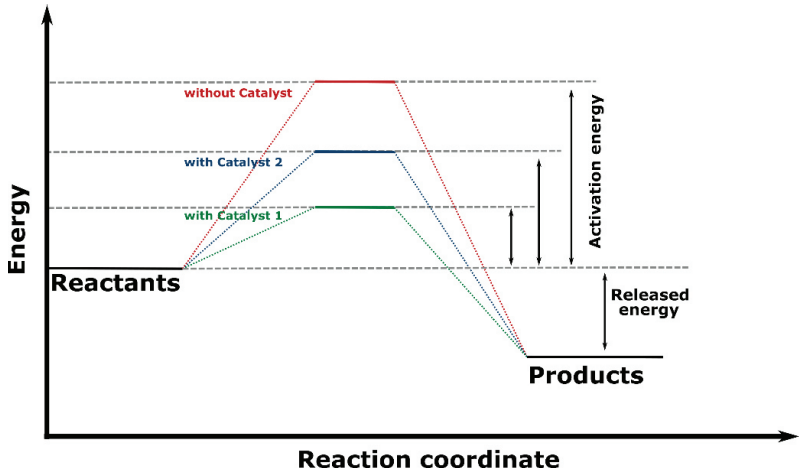

Figure 2.2. Schematic of the electrocatalytic reaction pathway.

Heterogeneous electrocatalysts have widespread applications, including efficient energy utilization, chemical energy conversion, and selective reaction pathway. However, challenging questions still need to be resolved, e.g., the increase in the electrode working life as well as the search for cost-effective electrocatalyst materials. Guo-Qiang Lu and Andrzej Wieckowski have highlighted the essential applications of heterogeneous electrocatalysts (Figure 2.3) [7].

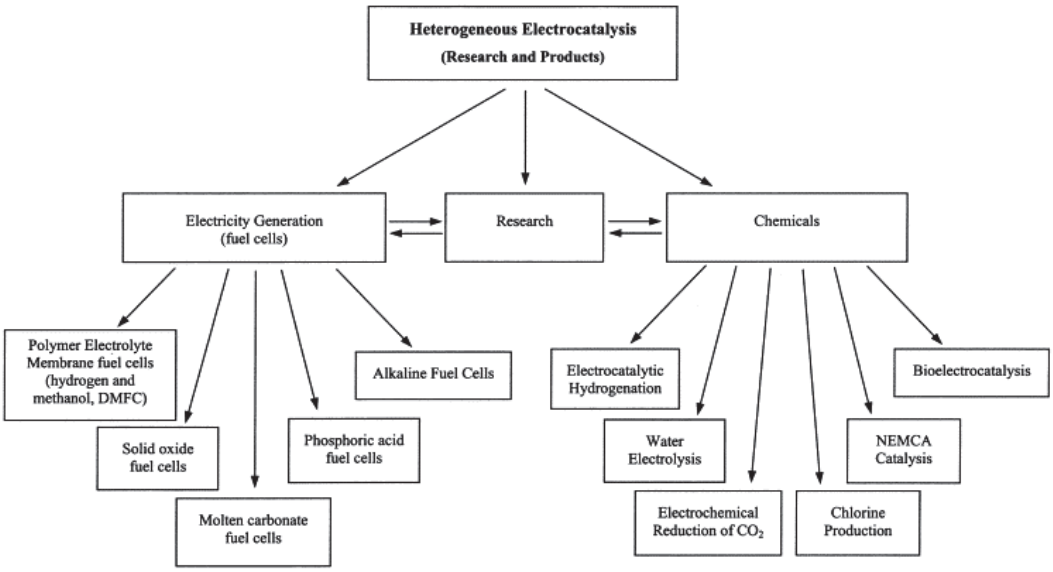

Figure 2.3. Practical outcomes of heterogeneous electrocatalytic reactions. The significance of the research in the categories of electricity generation and chemical production is highlighted [7].

2.2 Electrocatalysts in Fuel cells

Although William Grove invented the first fuel cell in 1840, Christian Friedrich Schönbein discovered the basic principles of fuel cells for the first time in 1839 when he demonstrated the reverse electrolysis of hydrogen. However, the industrial-scale technological development of fuel cells started 1 century later, when the space race between the U.S.A and U.S.S.R began in the 1960s. Currently, fuel cells are key in research and industrial fields. Fuel cells convert chemical energy into electrical energy using fuel that can be produced from intermittent energy sources, which can be subsequently stored in large quantities. The conversion efficiency into electrical energy is a key parameter. This technology finds widespread applications (e.g., vehicles and power generators)" [8-10], and it is an environment-friendly technology because no greenhouse gas emissions that cause global warming are generated in the process. However, research is still required with respect to the reduction of costs and increase in the working life. Based on the materials used, working conditions, and the molecules used as fuel, different fuel cells exist, e.g., alkaline fuel cells (AFC), proton-exchange membrane fuel cells (PEMFC), and solid-oxide fuel cells (SOFC) [11]. This thesis focuses on the direct formic acid fuel cells (DFAFC) and direct methanol fuel cells (DMFC), which constitute a subcategory of PEMFC. Electrochemical reactions (oxidation–reduction reactions) occurring in PEMFC enhance the charge transfer, with the help of other parts of the cell, and the charges flow, affording current density. Figure 2.4a shows a PEMFC. To produce energy, two gases are injected to the PEMFC: Hydrogen is injected to the anode for oxidation, and oxygen is injected to the cathode, which undergoes reduction to water. Oxygen can be replaced by air. The oxidation of hydrogen at the anode affords protons (H^+) and electrons (e^-) (eq. 2.1). The formed H^+ circulate in the electrolyte toward the cathode, and the e^- pass through an external circuit to reach the cathode and produce a current. The oxygen at the cathode combines with H+ and the electrons from the anode and are subsequently reduced to H_2O (eq. 2.2). An exothermic reaction occurs at the cathode, releasing heat that also can be used.

Anode reaction: $H_2 \rightarrow 2H^+ + 2e^-$ 2.1

cathode reaction: $O + 4H^+ + 4e^- \rightarrow 2H_2O$ 2.2

The resultant equation is as follows:

$2H_2 + O_2 \rightarrow 2H_2O + electricity + heat$ 2.3

PEMFC comprise several layers of materials, each of which plays a role in energy production (Figure 2.4b) [11]:

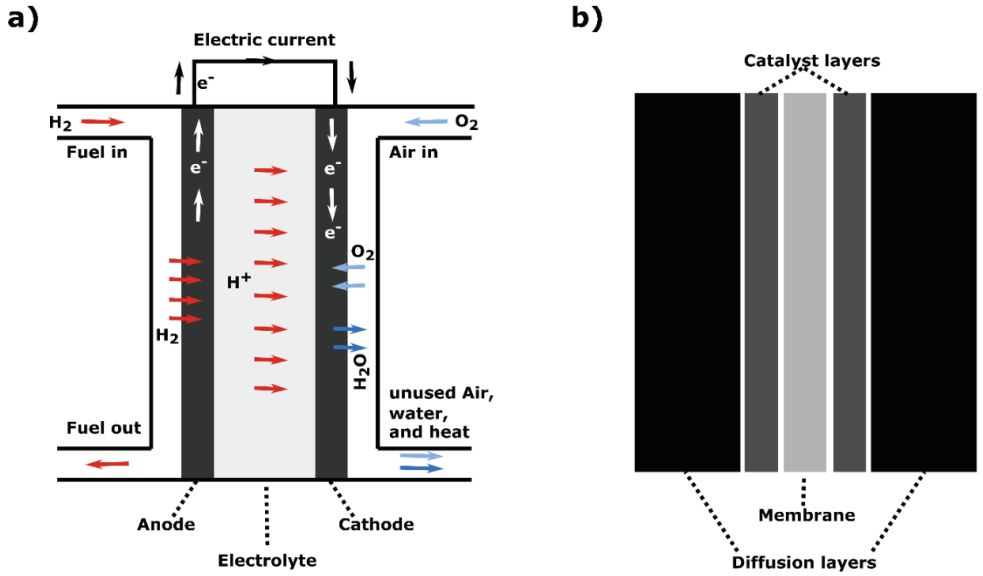

Figure 2.4. a) Working principle of PEMFC. b) Schematic of PEMFC elements.

- **Gas diffusion layers:** permit the diffusion of gases up to the active layer; these layers are composed of microporous materials, generally carbon fibers, and their thickness is between 100 and 500 μm. They are often subjected to hydrophobic treatment to manage the water inside the fuel cell.
- **Catalyst layers:** are located on each side of the membrane; an electrochemical reaction occurs at these layers which contain the catalyst that improves the reaction kinetics. These layers must exhibit three functions: they must exhibit good proton conductivity, permitting the transport of protons between sites of electrochemical reactions and the membrane; they must exhibit excellent electronic conductivity for the conduction of electrons to the external electric circuit; and they must provide facile access to reactive gases, in addition to the possibility of evacuating reaction products and inert gases (produced H_2O, N_2 of air).
- **Membrane:** is located in the center of the cell; it is an electrolyte composed of an ionic conductive polymer. It is often perfluorosulfonic acid (PFSA) such as Nafion. These materials must be electronic insulators and excellent proton conductors.

2.2.1 Direct Formic Acid Fuel Cells (DFAFC)

DFAFC are a subcategory of PEMFC, where instead of using hydrogen, formic acid (FA) is used as the fuel, which is directly fed to the anode. Formic acid at room temperature is liquid; thus, the storage of FA is easier and safer than that of hydrogen. DFAFC convert HCOOH and O_2 to CO_2 and H_2O, respectively, and produce an electric current. FA electrooxidation occurs at the anodic catalyst layer of the fuel cell, and the reaction at the anode (eq. 2.4) produces CO_2, H^+, and e^-. In PEMFC, H^+ move toward the cathode passing through the membrane and combine with oxygen at the cathode to form H_2O (eq. 2.5), while the electrons pass through an external circuit toward the cathode, affording the desired electric current.

Anode: $HCOOH \rightarrow CO_2 + 2H^+ + 2e^-$ 2.4

Cathode: $\frac{1}{2}O_2 + 2H^+ + 2e^- \rightarrow H_2O$ 2.5

Overall reaction: $2HCOOH + O_2 \rightarrow 2CO_2 + 2H_2O$ 2.6

The oxidation of HCOOH to CO_2 at the electrocatalyst anode (eq. 2.6) occurs via different mechanistic pathways (Figure 2.5):

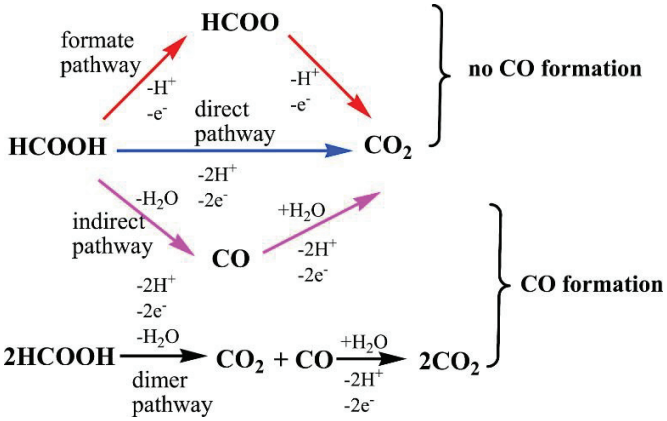

Figure 2.5. HCOOH electrooxidation mechanisms along different pathways [12].

- *Indirect pathway*: proceeds by the dehydration of HCOOH and the formation of CO molecules as the intermediate species (called poisoning intermediates) [12].
- *Direct pathway*: proceeds by the dehydrogenation of HCOOH to directly form CO_2 [12] without the formation of poisoning species.
- *Formate pathway*: starts with an O–H bond-breaking reaction to form an $HCOO^-$ intermediate, followed by the oxidation of $HCOOH^-$ to CO_2 [12].

- *Dimer pathway*: proceeds with the simultaneous formation of CO_2 and CO intermediates during the oxidation of HCOOH [12].

2.2.2 Direct Methanol Fuel Cell (DMFC)

DMFC is another subcategory of PEMFC. Due to the facile storage safety of methanol compared with that of hydrogen, as well as its high energy density, methanol (CH_3OH) is considered to be an alternative fuel. Methanol can be completely electrooxidized to CO_2 at low temperatures with a sufficient energy density. Methanol can be used in a fuel cell (or DMFC) or after reformation as a hydrogen source to PEMFC. The electrooxidation of methanol to CO_2 involves the transfer of six electrons. There are two acceptable pathways for the electrooxidation of CH_3OH: the direct pathway with no CO formation and the indirect pathway involving the formation of poisoning intermediate CO.

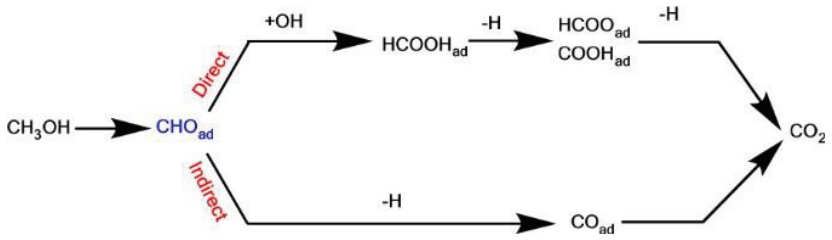

Figure 2.6. Direct and indirect pathways of CH_3OH oxidation [13].

The frame reactions in DMFC are as follows:

Anode: $CH_3OH + H_2O \rightarrow CO_2 + 6H^+ + 6e^-$ 2.7

Cathode: $\frac{3}{2}O_2 + 6H^+ + 6e^- \rightarrow 3H_2O$ 2.8

Overall reaction: $CH_3OH + \frac{3}{2}O_2 \rightarrow CO_2 + 2H_2O$ 2.9

2.2.3. Hydrogen Evolution Reaction (HER)

HER is a complex electrochemical interfacial process between the electrocatalyst and electrolyte (e.g., water, acid, base, etc.) that follows specific mechanisms depending on the pH, electrocatalyst, and applied voltage. The HER mechanism involves three steps (Figure 2.7) [14-17]. The first step involves the electrochemical adsorption of hydrogen (eq. 2.10), followed by desorption. The second step involves desorption, which can occur between the adsorbed hydrogen ions forming H_2 (Tafel reaction, eq. 2.11) or between one adsorbed hydrogen and one free hydrogen ion (Hyrovsky reaction, eq. 2.12).

Volmer reaction: $H_3O^+ + M + e^- \rightarrow MH_{ads} + H_2O$ 2.10

Tafel reaction: $2MH_{ads} \rightarrow H_{2\uparrow} + 2M$ 2.11

Heyrovsky reaction: $MH_{ads} + H_3O^+ + e^- \rightarrow H_{2\uparrow} + M + H_2O$ 2.12

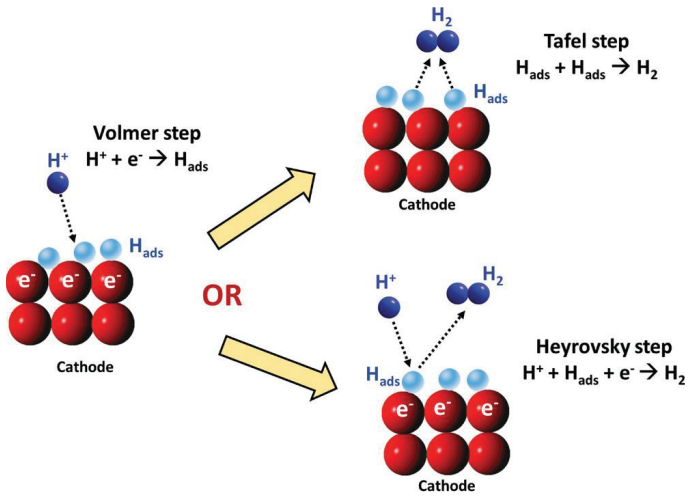

Figure 2.7. Schematic illustration represents the possible paths for HER [17].

2.3 Overview of electrocatalytic properties of nanoscale materials

Nanoscience is the field of study of nanoscale materials and exploitation of small-sized materials (from angstroms to hundreds of nanometers). Nanoscale materials (or nanomaterials) can exhibit different shapes (such as nanospheres, nanotubes, nanowires, nanorods). For current and future science, as well as technological applications, nanomaterials are of immense interest and increasing importance. They exhibit peculiar electrical, mechanical, optical, and magnetic properties that differ from those of bulk materials, and make them irreplaceable for novel applications. Significant potential has been invested in nanomaterials research to examine additional applications and shape a new technological future of electronics, biology, medical treatment, optics, energy conversion, and storage [18-22]. For fuel cell applications, nanomaterials have demonstrated efficiency due to their increased activity together with decreased electrocatalyst loading. As catalytic reactions occur on the catalyst surface, which is obviously huge for nanomaterials, the electrocatalytic activity may be orders of magnitude higher than corresponding bulk materials [22,23]. Besides, the designing of shape and composition can lead to drastic improvement of the electrocatalytic activity [24-26]. In the following, known electrocatalysts are discussed.

2.3.1 Platinum group metals nanomaterials

Platinum group metals (PGM) include platinum, palladium, ruthenium, rhodium, rhenium, osmium, and iridium. These elements exhibit specific properties such as excellent corrosion resistance and a high melting point; hence, they have demonstrated to be suitable catalysts. This group of metals includes rare and precious metals. PGM are often found as alloys in nature, indicating that the production and purification of these elements are expensive. Currently, PGM are mainly used in electrocatalytic applications; this is a limiting factor for fuel cell production industries. Figure 2.8 shows the activities of different metals compared to PGM.

Several studies have demonstrated that the use of multi-catalytic materials as a mixture of PGM and other materials can accelerate the kinetics of oxidation/reduction reactions. Previously, platinum black was predominantly used as the catalyst in large quantities to obtain suitable performance; however, high catalyst loading leads to high costs. The first technological solution involved the use of carbon-supported platinum nanoparticles, leading to the significant reduction in the platinum loading. In the past decades, several studies have been conducted on multi-metal catalysts based on Pt and transition metals or PtM (M = Fe, Co, Pd), which afforded key results in terms of performance compared to pure platinum [27].

For the large-scale development of the fuel cell market, it is crucial to either reduce the amount of platinum in the catalyst or even eliminate it completely. Various solutions have been proposed to reduce platinum in fuel cells. However, studies revealed that among pure metals, platinum exhibits the best performance; hence, additional research has been focused on its partial replacement.

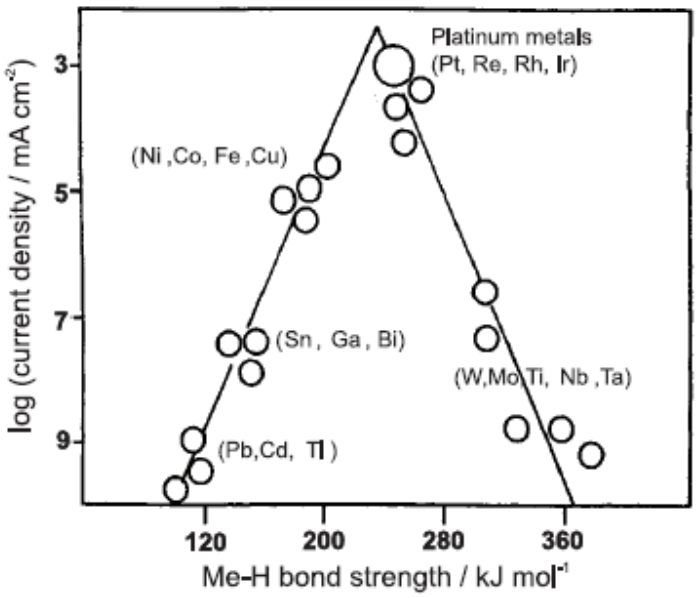

Figure 2.8. Volcano-type correlation of the catalytic activities of different metals to the Me–H binding energy [28].

2.3.2 Core–shell structures and alloy structures

The electrocatalyst surface is used for electrochemical reactions in FC, while the particle core only supports this surface or drives the electrons. Core–shell structures demonstrate a solution of changing the nanoparticle core with inexpensive metals while maintaining the nanoparticle surface comprising highly active metals such as platinum. A majority of core–shell nanoparticles have been synthesized with platinum and transition metals as the shell and core, respectively: Such structures exhibit high electrocatalytic activity with a significant decrease in the amount of precious metals used.

On the other hand, bimetallic and trimetallic Pt-based alloys are attracting significant research interest. The electronic states per atom in the 5d band of a platinum alloy are greater than those in the 5d band of pure platinum. This evolution of the electronic structure undoubtedly affects the catalytic mechanisms for the transfer of electrons to the aggregate–electrolyte interface. Currently, the electrocatalysts of platinum alloyed with ruthenium represent good materials.

Here, some examples of core–shell and alloy structures are as follows:

- **Pt@Pd:** Choi et al. [24] have reported enhanced catalytic activity by using Pd as the core, related to the electronic modification of the Pt catalyst when it is in contact with other noble metals (Figure 2.9a).
- **Pt@M, M = Fe, Co, and Ni:** Kuttiyiel et al. [25] have examined the use of non-precious metal nitrides and Pt as the core and shell, respectively, for oxygen reduction reactions (ORR). Their study demonstrated that the metal nitride core changes the electronic structure of the Pt catalyst (Figure 2.9b). In addition, the metal nitride apparently increases the stability of the core–shell structure.
- **Pt:M, M = Ti, V, Fe, Co, and Ni:** Stamenkovic et al. [27] have revealed that alloying transition metals with Pt changes the electronic structure of the alloy and improves the electrocatalytic activity toward ORR (Figure 2.9c).

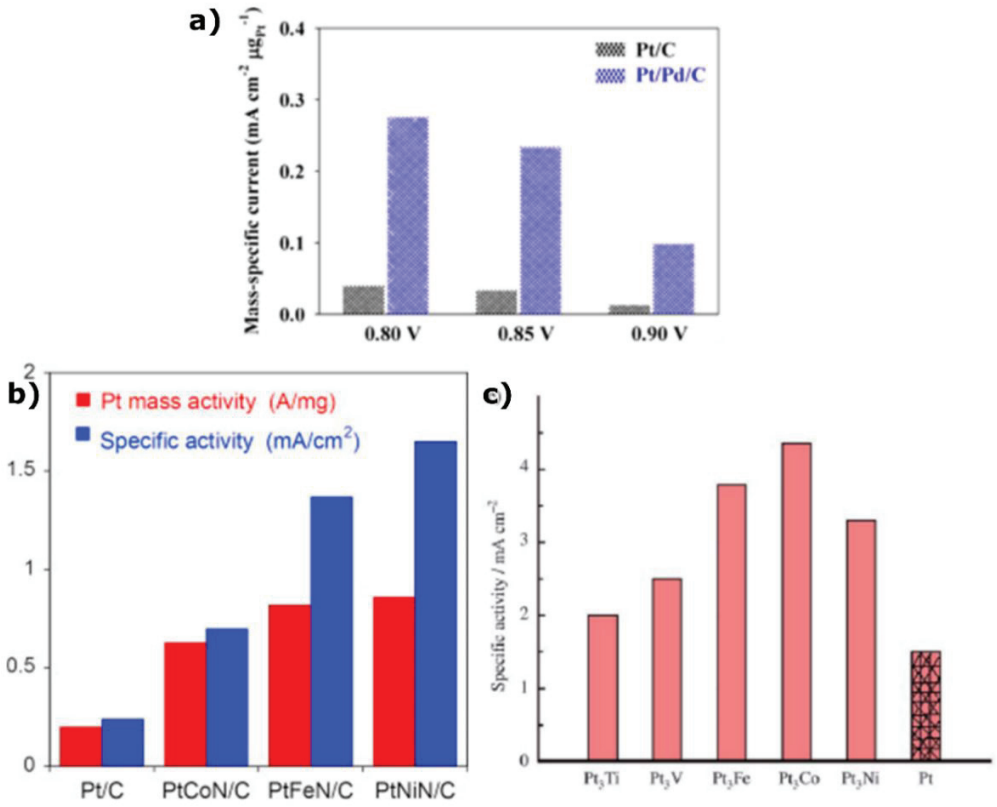

Figure 2.9. a) Mass and specific activities of PtCoN/C, PtFeN/C, and PtNiN/C as well as commercial Pt/C [24]. b) Specific activity comparison of Pt/C and Pt/Pd/C [25]. c) Specific activities of Pt and Pt3M electrodes expressed as the kinetic current density for ORR at 0.9 V (0.1 M $HClO_4$, 333 K) [26].

One-dimensional (1D) nanostructures such as nanorods, nanowires, and nanotubes exhibit promising activity and durability as electrocatalysts for applications in PEM fuel cells. Lu et al. summarized the properties of 1D electrocatalysts and their advantages over 0D electrocatalysts.

Some examples of 1D structures are as follows:

- **Ni@Pt core–shell nanotube [29]:** The as-synthesized porous Ni@Pt core–shell nanotube exhibited high electrocatalytic properties with a low Pt loading. In 0.5 M H_2SO_4 + 0.5 M CH_3OH, the current density was 1.5 mA/cm² for Ni@Pt (Pt loading of 33.4 μg/cm²), while it was ~0.7 mA/cm² for Pt/C (Pt loading of 28 μg/cm²). Compared to Pt/C, Ni@Pt NTs exhibited enhanced activity for the methanol electrooxidation (Figure 2.10a).
- **Pd–Pt alloys nanowires**: Rana et al. [30] reported that Pd_{73}-Pt_{27} nanowires exhibit activity 10 times greater than that of commercial Pt/C for the methanol oxidation. Such high activity might correspond to the ligand effects between Pt and Pd. The stability study revealed that after 1000 cycles, ~100 mA/mgPt is lost from $Pd_{73}Pt_{27}$, but it is still considerably greater than Pt/C. After 1000 cycles, the activity of the PdPt nanowires maintained stability for up to 4000 cycles, while Pt/C activity kept decreasing (Figure 2.10b).
- **Pt,Pd nanotubes and nanorods:** Previously, Dar et al. [31] reported on Pt nanotubes/nanorods for methanol electrooxidation: The nanotubes exhibited an extremely high electrochemical surface area and an enhanced electrocatalytic activity. Pt NTs exhibited a current density of 128 mA/mg, while Pt nanorods exhibited a current density four times less than this value. The same research group reported a current density of 300 mA/mg for Pd nanotubes for the oxidation of formic acid.

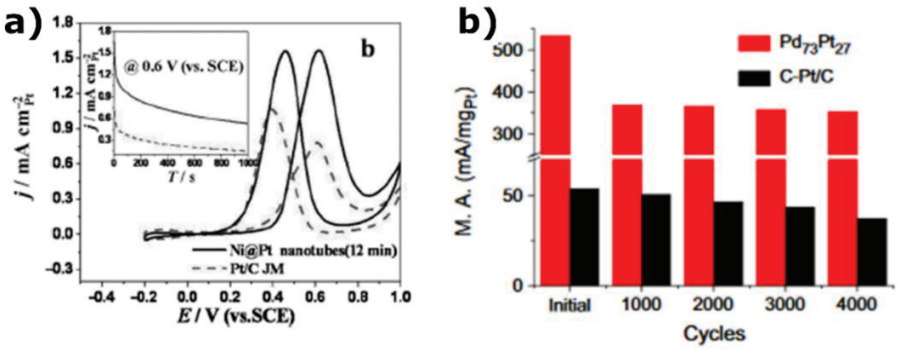

Figure 2.10. a) Cyclic Voltammetry and chronoamperometry of Ni@Pt core-shell nanotube compared to Pt/C [29]. b) Pd73Pt27 stability over cycles compared to Pt/C [30].

2.4 References

[1] R. Masel, Chemical Kinetics and Catalysis, *John Wiley & sons, Inc* (2001), ISBN 9780471241973.

[2] L. Lloyd, Handbook of inDustrial Catalysts, *Springer US* (2011), ISBN 9780387499628.

[3] A. J. Bard, G. Inzelt, F. Scholz, Electrochemical Dictionary, *Springer-verlag: Berlin Heidelberg* (2008), ISBN 9783642295515.

[4] S. Srinivasan, Fuel Cells, *Springer* (2006), ISBN 9780387354026 .

[5] K. J. Laidler, J. H. Meiser, B. C. Sanctuary, Physical Chemistry, *Benjamin/Cummings* (1982), ISBN 9780618123414.

[6] I. Chorkendorff, J.W. Niemantsverdriet, Concepts of Modern Catalysis and Kinetics, *Wiley-VCH* (2003), ISBN 9783527305742.

[7] G.-Q. Lu, A. Wieckowski, Heterogeneous Electrocatalysis: A Core Field of Interfactial Science, *Current Opinion in Colloid Interface Science* 5 (200) 95.

[8] A. Choudhury, H. Chandra, A. Arora, Application of Solid Oxide Fuel Cell Technology for Power Generation—A Review, *Renewable and Sustainable Energy Reviews* 20 (2013) 430.

[9] A. Qi, B. Peppley, K. Karan, Integrated Fuel Processors for Fuel Cell Application: A Review, *Fuel Processing Technology* 88 (2007) 3.

[10] V. Mehta, J. S. Cooper, Review and Analysis Of PEM Fuel Cell Design And Manufacturing, *Journal of Power Sources* 114 (2003) 32.

[11] L.J.M.J. Blomen, M. N. Mugerwa, Fuel Cell Systems, *Springer US* (1993), ISBN 9781489924247.

[12] W. Zhong, Y. Qi, M. Deng, The Ensemble Effect Of Formic Acid Oxidation On Platinum–Gold Electrode Studied By First-Principles Calculations, *Journal of Power Sources* 278 (2015) 203.

[13] L. Ou, New Insights Into The Pt-Catalyzed CH_3OH Oxidation Mechanism:First-Principle Considerations on Thermodynamics, Kinetics, and Reversible Potentials, *ACS Omega* 3 (2018) 886.

[14] B. E. Conway, B. V. Tilak, Interfacial Processes Involving Electrocatalytic Evolution and Oxidation of H_2, and the Role of Chemisorbed H, *Electrochimica Acta* 47 (2002) 3571.

[15] J. O. Bockris, B. E. Conway, Modern Aspects of Electrochemistry, *Butter-worths Sci Publications* (1954), ISBN 9781461574637.

[16] D. D. Eley, H. Pines, P. B. Weisz, Advance in Catalysis, *Elsevier* (1992).

[17] S. Gupta, M. K. Patel, A. Miotello, N. Patel, Metal Boride-Based Catalysts for Electrochemical Water-Splitting: A Review, *Advanced Functional Materials* 30 (2020) 1906481.

[18] Z. H. Khan, Nanomaterials and Their Applications, *Springer Singapore* (2018), ISBN 9789811062148.

[19] M. H. Chaudhery, Handbook of Nanomaterials for Industrial Applications, *Elsevier* (2018), ISBN 9780128133514.

[20] Z. Cai, F. Li, M. Rong, L. Lin, Q. Yao, Y. Huang, X. Chen, X. Wang, Novel Nanomaterials for Biomedical, Environmental and Energy Applications, *Elsevier* (2019), ISBN 9780128144978.

[21] T. Pradeep, Anshup, Noble Metal Nanoparticles For Water Purification: A Critical Review, *Thin Solid Films* 517 (2009) 6441.

[22] I. Capek, Noble Metal Nanoparticles, *Springer Japan* (2017), ISBN 9784431565567.

[23] B. A. Bhanvase, V. B. Pawade, S. J. Dhoble, S. H. Sonawane, M. Ashokkumar, Nanomaterials for Green Energy, *Elsevier* (2018), ISBN 9780128137314.

[24] I. Choi, S. H. Ahn, J. Jeong Kim, O. Joong Kwon, Preparation of Pt shell–Pd Core Nanoparticle with Electroless Deposition of Copper for Polymer Electrolyte Membrane Fuel Cell, *Applied Catalysis B: Environmental* 102 (2011) 608.

[25] K. A.Kuttiyiel, Y. M. Choi, S. -M. Hwang, G. -G. Park, T. -H. Yang, D. Su, K. Sasaki, P. Liu, R. R.Adzic, Enhancement Of The Oxygen Reduction On Nitride Stabilized Pt-M (M=Fe, Co, And Ni) Core–Shell Nanoparticle Electrocatalysts, *Nano Energy* 13 (2015) 442.

[26] V. Stamenkovic, B. S. Mun, K. J. J. Mayrhofer, P. N. Ross, N. M. Markovic, J. Rossmeisl, J. Greeley, J. K. Nørskov, Changing the Activity of Electrocatalysts for Oxygen Reduction by Tuning the Surface Electronic Structure, *Angewandte Chemie* 118 (2006) 2963.

[27] V. Mazumder, M. Chi, K. L. More, S. Sun, Core / Shell Pd / FePt Nanoparticles as an Active and Durable Catalyst for the Oxygen Reduction Reaction, *Journal of American Chemical Society* 5 (2010) 7848.

[28] H. Wendt, E. V. Spinacé, A. oliveira neto, M. Linardi, Electrocatalysis And Electrocatalysts For Low Temperature Fuel Cells: Fundamentals, State of The Art, Research and Development, *Química Nova* 28 (2005) 1066.

[29] L. -X. Ding, G. -R. Li, Z. -L. Wang, Z. -Q. Liu, H. Liu, Y. -X. Tong, Porous Ni@Pt Core-Shell Nanotube Array Electrocatalyst with High Activity and Stability for Methanol Oxidation, *Chemistry—A European Journal* 18 (2012) 8386.

[30] M. Rana, P. K. Patil, M. Chhetri, K. Dileep, R. Datta, U. K. Gautam, Pd–Pt Alloys Nanowires as Support-Less Electrocatalyst With High Synergistic Enhancement in Efficiency for Methanol Oxidation in Acidic Medium, *Journal of Colloid and Interface Science* 463 (2016) 99.

[31] F. I. Dar, S. Habouti, R. Minch, M. Dietze, M. Es-Souni, Morphology Control Of 1D Noble Metal Nano/Heterostructures Towards Multi-Functionality, *Journal of Materials Chemistry* 22 (2012) 8671.

3 Synthesis and characterization of nanoscale materials

3.1 Sonochemistry

3.1.1 General Concept of Sonochemistry

Ultrasound is defined as acoustic waves with frequencies in the complete range of 16 kHz to 10 MHz. The ultrasonic frequency range is divided into power ultrasound and high-frequency ultrasound. Power ultrasound involves intensive waves with a low frequency (16–1000 kHz). In this frequency range, the medium is modified due to cavitation. Modification can be physical (e.g., degassing, stripping, etc.) or chemical (change in reactions mechanisms, production of free radicals). The popular example of power ultrasound applications involves ultrasonic cleaners that operate at less than 50 kHz. Generally, in Sonochemistry it is unusual to utilize higher frequencies up to megahertz. Effects of ultrasound on the medium are related to cavitation. Cavitation activity permits the transformation of low-energy density of an acoustic field into high-energy density in the vicinity of implosion bubbles [1-4].

Sonochemistry involves the use of ultrasound to produce intermediate reactive species and accelerate or change the reaction mechanism to obtain products different from those obtained under typical reaction conditions. The conversion of several chemical reactions as well as to improve the physical process through cavitation effects, when a system is supplied with sufficient energy capable of overcoming the cohesive forces of a liquid, where the pressure of the liquid becomes less than its vapor pressure, cavitation occurs, and then bubbles containing gas and vapor of the liquid appear. The change in the necessary forces that leads to bubble formation is related to the properties and purity of the liquid. Four types of cavitation exist: thermal, optical, hydrodynamic, and acoustic cavitation. When the pressure inside the bubble is greater than the gas pressure, the bubble surface increases, and the difference in the concentration between the bubble (low concentration) and liquid (high concentration) forms a driving force for the transfer of matter toward the inside the bubble: liquid–vapor and dissolved gas diffuse into the bubble. Thus, the bubble size and transfer surface are larger during the relaxation phase than during the compression phase. Therefore, the amount of material contained in the bubble increases with time [1-4]. Cavitation bubbles overgrow and then collapse, and their lifetime does not exceed a few cycles of compression and refraction (Figure 3.1).

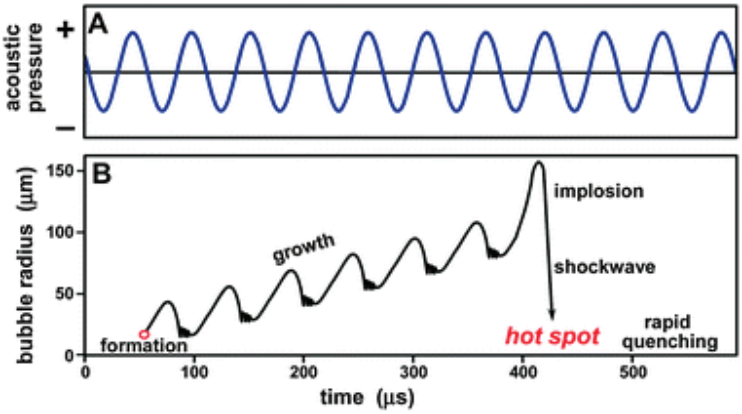

Figure 3.1. Schematic representation of cavitation bubble formation, growth, and subsequent collapse over several acoustic cycles [4].

Sonochemistry occurs during the final bubble growth and collapse. The cavitation bubble oscillates in an ultrasonic field and reaches high pressure and high temperature. During the growth of the cavitation bubble, matter is transferred between the liquid zones toward the inside of the bubble [4]. Dissolved gases from the medium and vapor diffuse in the bubble according to Henry's law. By definition, Henry's law states that at constant temperature, the amount of dissolved gas in a liquid is proportional to the pressure applied from the gas to the liquid [5]. High temperature and high pressure are ideal conditions for radical formation. In an aqueous solution, liquid vapor within the cavitation bubble is dissociated into various products, referred to as water sonolysis.

Henry's law: $C_s = p.H$, where C_s is the maximum gas pressure, p is the partial pressure, and H is the Henry constant.

3.1.2 Sonochemical Synthesis of Nanoparticles

The cavitation bubble accumulates ultrasonic energy until it reaches a specific size (tens of micrometers), loses its ability to absorb additional energy and collapses. Bubble collapse occurs in a short time and is assumed to be adiabatic. At this stage, the bubble accumulates energy in a localized spot fast, leading to high pressure and temperature at this spot; this spot is called a hot spot (Figure 3.2). Cooling and heating rates are incredibly high at the hot spot, leading to primary sonochemistry. Reactions occur inside the bubble, affording crystallite nanomaterials [4]. Besides, the thin liquid layer surrounding the bubble is exposed to low pressure and temperature, which aid in the reaction of the non-volatile precursor and production of amorphous or crystalline nanomaterials, referred to as secondary Sonochemistry [4].

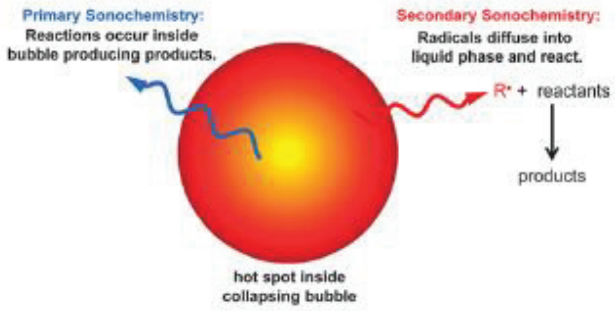

Figure 3.2. The hot-spot inside the collapsing bubble and different Sonochemistry processes [4].

Sonochemistry has been widely used for the synthesis of nanomaterials starting either from volatile or non-volatile precursors. Noble-metal nanostructures are typically prepared from non-volatile precursors dissolved in a volatile solvent (water) [4]. During this process, the sonolysis of the solvent vapor affords reductants that can surpass the use of external reducing agents. Water sonolysis generates highly reactive $OH^{\bullet}$ and $H^{\bullet}$, which are responsible for redox chemistry. Furthermore, these reactive radicals can react with organic additives in the solution, generating secondary radicals $R^{\bullet}$. The process can be summarized by the following equations:

$$H_2O \rightarrow H^{\bullet} + OH^{\bullet} \quad 3.1$$

$$H^{\bullet} + H^{\bullet} \rightarrow H_2 \quad 3.2$$

$$H^{\bullet} + OH^{\bullet} \rightarrow H_2O \quad 3.3$$

$$OH^{\bullet} + OH^{\bullet} \rightarrow H_2O_2 \quad 3.4$$

$$RH(volatile - vapour) \rightarrow R^{\bullet} + H^{\bullet} \quad 3.5$$

$$RH + OH^{\bullet} \rightarrow R^{\bullet} + H_2O \quad 3.6$$

$$RH + H^{\bullet} \rightarrow R^{\bullet} + H_2 \quad 3.7$$

$$M^{n+} + nR^{\bullet} \rightarrow M^0 \quad 3.8$$

$$M^{n+} + nH^{\bullet} \rightarrow M^0 \quad 3.9$$

$$mM^0 \rightarrow M_m \quad 3.10$$

Sonochemistry exhibits several advantages for the synthesis of metallic nanomaterials. The use of a chemical reducing agent is not required. The radicals produced during sonochemical irradiation serve as reducing agents. Due to the high temperature and pressure in the hot spots, reaction rates are sufficiently high for small nanoparticles to be formed [4]. The following noble-metal nanoparticles are synthesized by sonochemistry:

- **Au Nanoparticles:**

Kanji et al. [6] reported the sonochemical synthesis of gold nanoparticles from an aqueous solution containing 1-propanol. Their results showed correlation between the Au(III) reduction rate and ultrasound frequency (Figure 3.3a). Thus, the size and distribution of nanoparticles also depend on the ultrasound frequency. Furthermore, nucleation and growth processes were governed by chemical effects of cavitation and not the accompanying physical effects. The sonochemical reduction of Au(III) in the presence of organics proceeds as follows:

$$H_2O \rightarrow OH^{\bullet} + H^{\bullet} \quad 3.11$$

$$RH + OH^{\bullet} \rightarrow R^{\bullet} + H_2O \quad 3.12$$

$$RH + H^{\bullet} \rightarrow R^{\bullet} + H_2 \quad 3.13$$

$$\mathrm{RH} \rightarrow \text{ pyrolysis radicals and unstable products} \quad 3.14$$

$$\mathrm{Au(III)} + \text{ reducing species(H}\bullet, \mathrm{R}\bullet, \text{etc.)} \rightarrow \mathrm{Au(0)} \quad 3.15$$

- **Pt Nanoparticles:**

Mizukoshi et al. [7] prepared Pt nanoparticles from an aqueous solution in the presence of a surfactant by using high-intensity ultrasound (Figure 3.3b). The presence of a surfactant allows for the high stability of nanoparticles as it permits homogeneity in their shape and size. During Pt(II) sonochemical reduction, three reducing species were proposed: Hydrogen atoms; radicals from the thermal decomposition of the surfactant at the interface between the cavitation bubble and bulk solution; and radicals formed via $OH^{\bullet}$ or $H^{\bullet}$ with the surfactant.

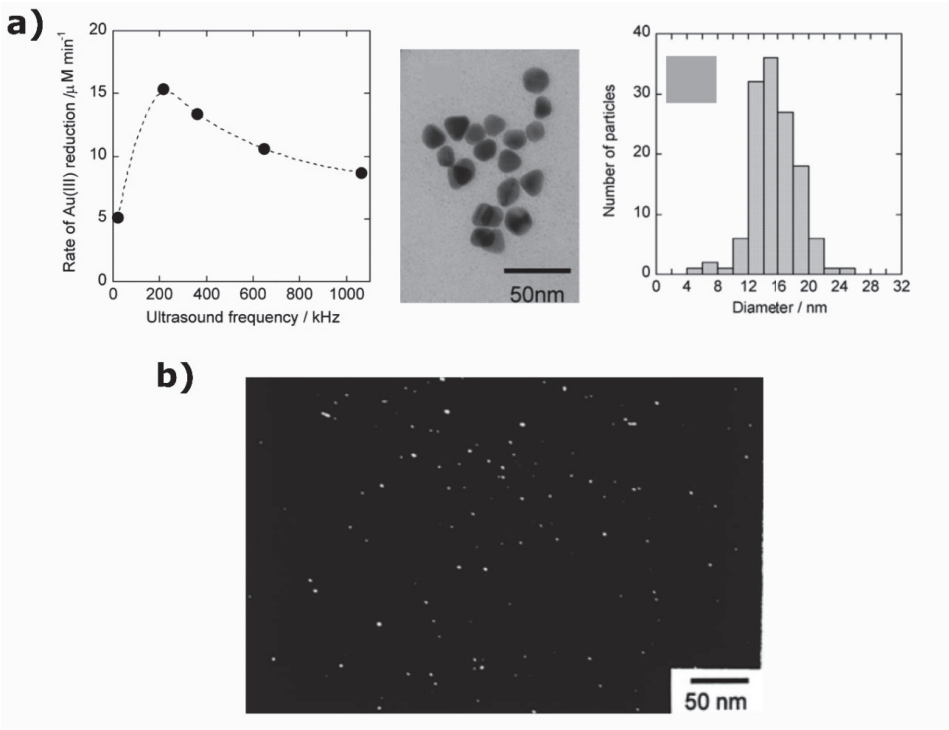

Figure 3.3. a) Au(III) reduction rate as a function of the ultrasound frequency. TEM micrograph of Au nanoparticles synthesized after 120 min irradiation with 213 kHz ultrasound. Histogram showing the size distribution of Au nanoparticles [6]. b) TEM photographs of platinum nanoparticles prepared by the sonochemical method [7].

3.2 AAO templates

3.2.1 Physical Vapor Deposition

Physical vapor deposition (PVD) is a coating process in which ions, atoms, or molecules are deposited on a surface. The thickness of the as-produced layer may range from a few nanometers to hundreds of micrometers. Deposition requires high vacuum conditions. Metallic vapor is derived from a solid or liquid target by means of heat (evaporation), ionization (sputtering), or a combination of both.

- **Sputtering**

Physical sputtering is based on the formation of a discharge between two electrodes. The target is used as the cathode, while the substrate is used as the anode. DC voltage is applied between two electrodes under inert gas, mostly argon. Electric discharge ionizes the argon gas atoms and forms

plasma. Ar^+ ions are attracted to the target and acquire energy that they release once they come in contact with the target. This released energy is transmitted to the target atoms that are sputtered and then deposited on the substrate. To obtain materials with good crystallinity, not only high-voltage sputtering but also substrate heating is required. To overcome this issue, magnets are placed under the cathode, which trap electrons, hence move in a cycloidal trajectory and acquire high energy. The plasma formed in the chamber is then confined and closer to the cathode [8-10] (Figure 3.4), referred to as magnetron sputtering; it exhibits several advantages, such as a high ionization efficiency leading to a high sputtering rate at low voltages [9]; low deposition temperature; and ease of use with a large selection of target materials.

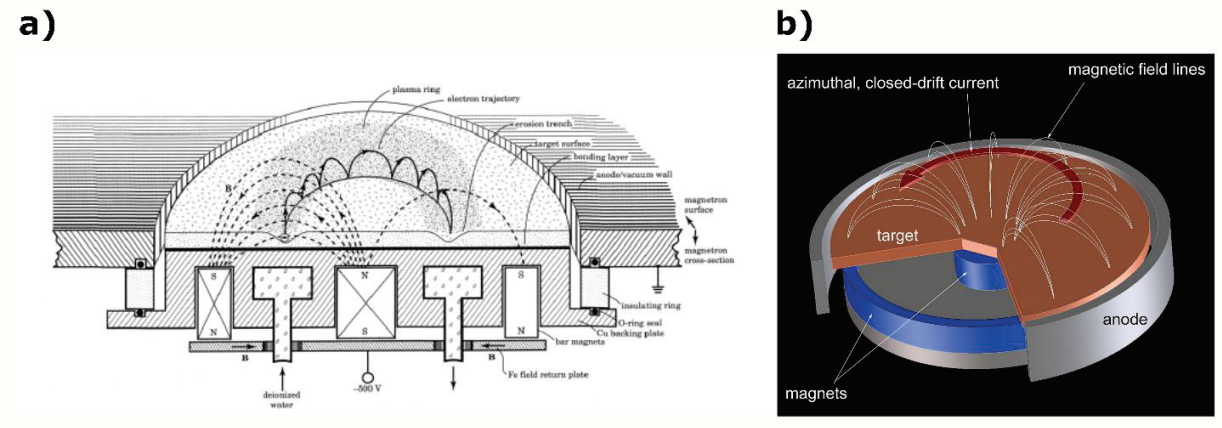

Figure 3.4. a) Schematic of magnetron sputtering [11]. b) Diagram depicting the electron drift on the top of the target [12].

- **Evaporation**

Electron-beam evaporation is a high-vacuum evaporation method in which the target material is placed in a cooled crucible, where it is heated until it evaporates. The cathode filament is heated by high voltage and generates high-energy electrons. The electron beam is deflected by a magnetic field and is focused on a crucible [8]. The electrons cause the local melting of the material until its evaporation due to low pressure. The evaporated material expands in the vacuum chamber and coats everything in it. The deposition rate can be easily controlled via the control of the applied power, and electron-beam evaporation can permit deposition at a rate as low as 1 nm/min to a few micrometers per minute (Figure 3.5).

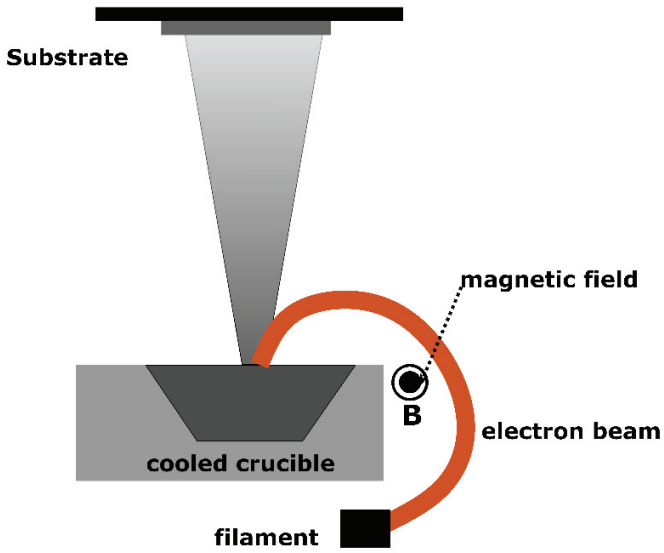

Figure 3.5. Schematic of electron-beam vapor deposition.

3.2.2 AAO Template Preparation

In the presence of an acid and electricity, aluminum, as some other transition metals, can be oxidized to Al_2O_3. The oxide layer formed during anodization, referred to as anodic aluminum oxide (AAO), exhibits a porous morphology. Several parameters (electrolyte, temperature, voltage) can change the aluminum pore characteristics such as density, diameter, interpore distance, and the order [13-16]. During potentiostatic anodization, the current density behavior exhibits four phases (Figure 3.6), corresponding to the growth of different Al_2O_3 layers and pore formation. In phase 1, the current density sharply decreases due to the splitting of water and aluminum into ions (eq. 3.16-3.18) [13,16].

$$H_2O \rightarrow 2H^+ + O^{2-} \quad 3.16$$

$$H_2O \rightarrow H^+ + OH^- \quad 3.17$$

$$Al \rightarrow Al^{3+} + 3e^- \quad 3.18$$

O_2^- and OH^- drift toward the anode and react with aluminum, affording an oxide layer of Al_2O_3 (eq. 3.19); this leads to a low current density (as oxide is less conductive than the metal), followed by the formation of pore pitches on cracks or weak spots. In phase 2, the oxide layer becomes porous, and the current density increases, before it stabilizes at a high value; also, O_2^- and OH^-

continue the drift toward the anode and release H^+, which drift toward the cathode and dissolve Al_2O_3 along the way (eq. 3.20) [13,16].

$$2Al + 3H_2O \rightarrow Al_2O_3 + 3H_2 \quad 3.19$$

$$Al_2O_3 + 6H^+ \rightarrow 2Al^{3+} + 3H_2O \quad 3.20$$

Owing to the high H^+ concentration in the pore bottom, Al_2O_3 dissolution is more rapid in the axial direction than in the radial direction, leading to vertical pore growth (Phase 3). For aluminum foils, this phase 3 controls the pore length. Anodization stops when the necessary length is acquired.

In this thesis, anodization is maintained on a thin aluminum layer deposited on heterogeneous underlayers (silicon/Ti/Au/Ti/Al). When there is no more Al metal to be oxidized, O_2^- and OH^- keep drifting to the anode, reach the Au underlayer, and concentrate at the interface between Al_2O_3 and Au (Phase 4). At this stage, water electrolysis transforms water into O_2 and H_3O^+ (eq. 3.21-3.22). H_3O^+ drift toward the cathode, while O_2 forms a bubble between Au and Al_2O_3, and Al_2O_3 forms a barrier layer. Anodization is completed at this level, and anodized aluminum is transferred to a pore-widening bath to open the pores and remove the barrier layer [13,16]. At that point the immersion time should be sufficient to completely remove the barrier layer.

$$6OH^- \rightarrow O_2 + 2H_2O + 4e^- \quad 3.21$$

$$6H_2O \rightarrow O_2 + 4H_3O^+ + 4e^- \quad 3.22$$

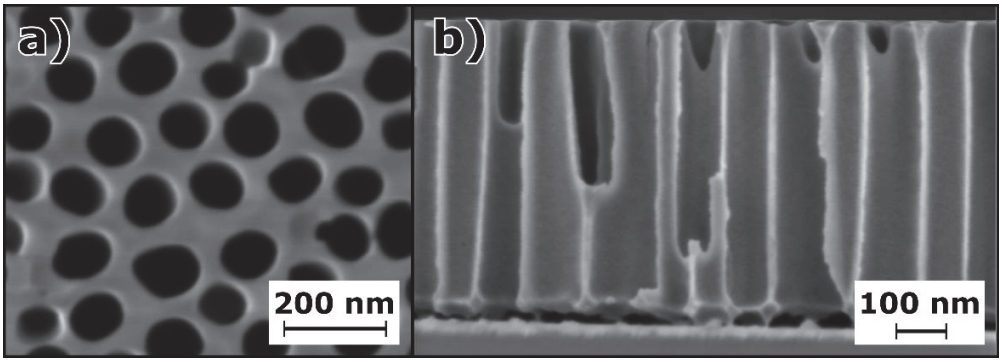

Figure 3.7. Top-view (a) and cross-section (b) of AAO.

Figure 3.7 shows the top view and cross-section of AAO templates after anodization and pore widening. Pore diameter, interpore distance, and pore order are controlled by different anodization parameters (e.g., electrolyte, voltage, concentration, temperature). The pore widening step is another parameter for controlling the diameter and interpore distance. Table 3.1 summarizes some of the optimized combinations of different anodization parameters and pore diameters after anodization in oxalic acid.

Table 3.1. Pores diameter and interpore distance range for different oxalic acid concentrations [14].

Concentration (M)	Voltage (V)	Interpore distance (nm)	Minimum opening time (min)/diameter (nm)	Maximum opening time (min)/ diameter (nm)
0.1	80	180	48/137	52/156
0.2	70	156	44/123	48/140
0.3	40	103	24/70	28/85
0.6	30	78	21/57	24/61

In this study, anodization was performed using a two-electrode setup, with aluminum and Pt-foil as the anode and cathode, respectively, in 0.2 M oxalic acid under potentiostatic conditions of 70 V using an electrochemical workstation (Keithley 2400 SM, Cleveland, OH, USA). Barrier layers were removed in a 5 wt% phosphoric acid bath at 30 °C for 50 min.

3.2.3 Nanostructure Synthesis using AAO Templates

Chemical electrodeposition of materials from aqueous electrolytes on an AAO template is a cost-effective method for producing 1D anisotropic ordered structures [15,17,18]. Electrodeposition occurs on an AAO template where the nanopores are in contact with an electrical underlayer (gold) and the electrolyte. The materials are deposited on the pores under potentiostatic conditions using suitable electrolyte and voltage. Nucleation occurs at the bottom of the pores and, through successive attachment of newly nucleated clusters, starts growing vertically.

Electrodeposition i–t curves recorded during potentiostatic electrodeposition provide insights into the related electrodeposition mechanism. Figure 3.8c shows the current behavior. Three important stages are observed in the i–t curve. First, the current increases to the maximum, indicative of metal nuclei formation, followed by a small drop in the current density due to the limited diffusion and growth. Then, the current starts to slowly increase due to the diffusion and

kinetics of nucleation. In the last stage of electrodeposition, the current remains quasi-stable, indicative of the predominance of kinetics control.

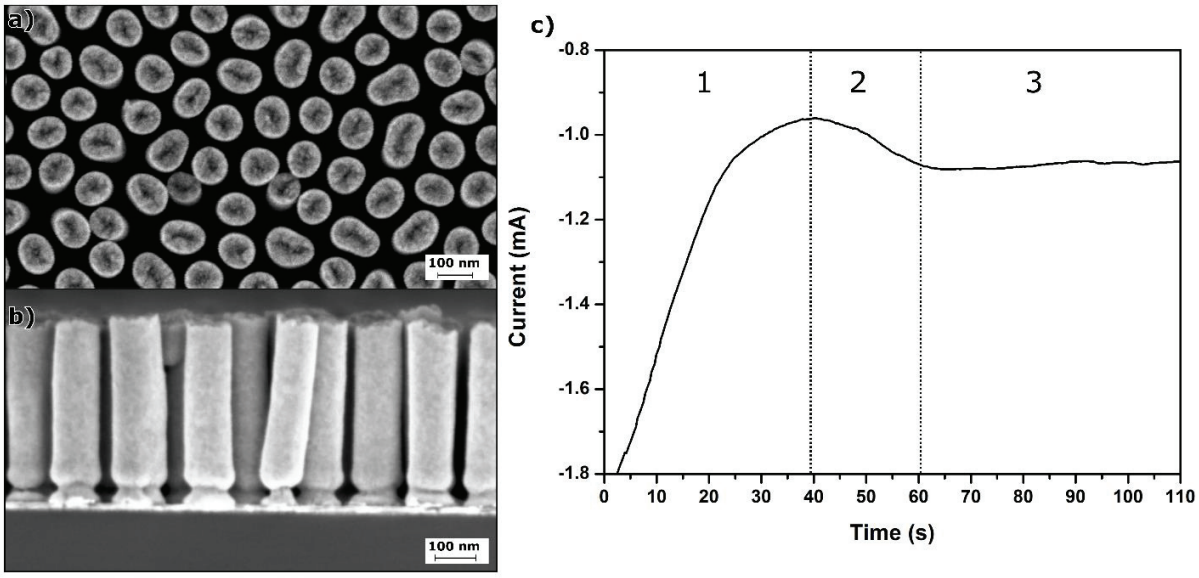

Figure 3.8. top view (a) and cross-section (b) of electrodeposited Pt-nanorods after dissolving the AAO template. c) the recorded current-time curve of the potentiostatic electrodeposition.

Electrodeposition is performed in a three-electrode cell, where the applied voltage is related to the Ag/AgCl electrode. Pt and AAO/Au were used as the counter and working electrodes, respectively. Electrodeposition was controlled by a potentiostat (PRINCETON). Table 3.2 summarizes different parameters for metal electrodeposition. Figure 3.8a-b shows the SEM micrographs of NRs after dissolving the AAO template in NaOH. SEM images reveal ordered self-standing nanorods, with a homogenous nanorod length.

Table 3.2. Used conditions for Pt, Au, and Pd electrodeposition.

	Electrolyte	Concentration (mM)	Voltage (V vs. Ag/AgCl)	Time/length (s/nm)
Pt-NRs	H_2PtCl_6	10	–0.1	100/70
Pd-NRs	Cl_4PdK_2	10	–0.1 for 100s, 0.3	150/60
Au-NRs	$HAuCl_4$	8	0.1	1000/300

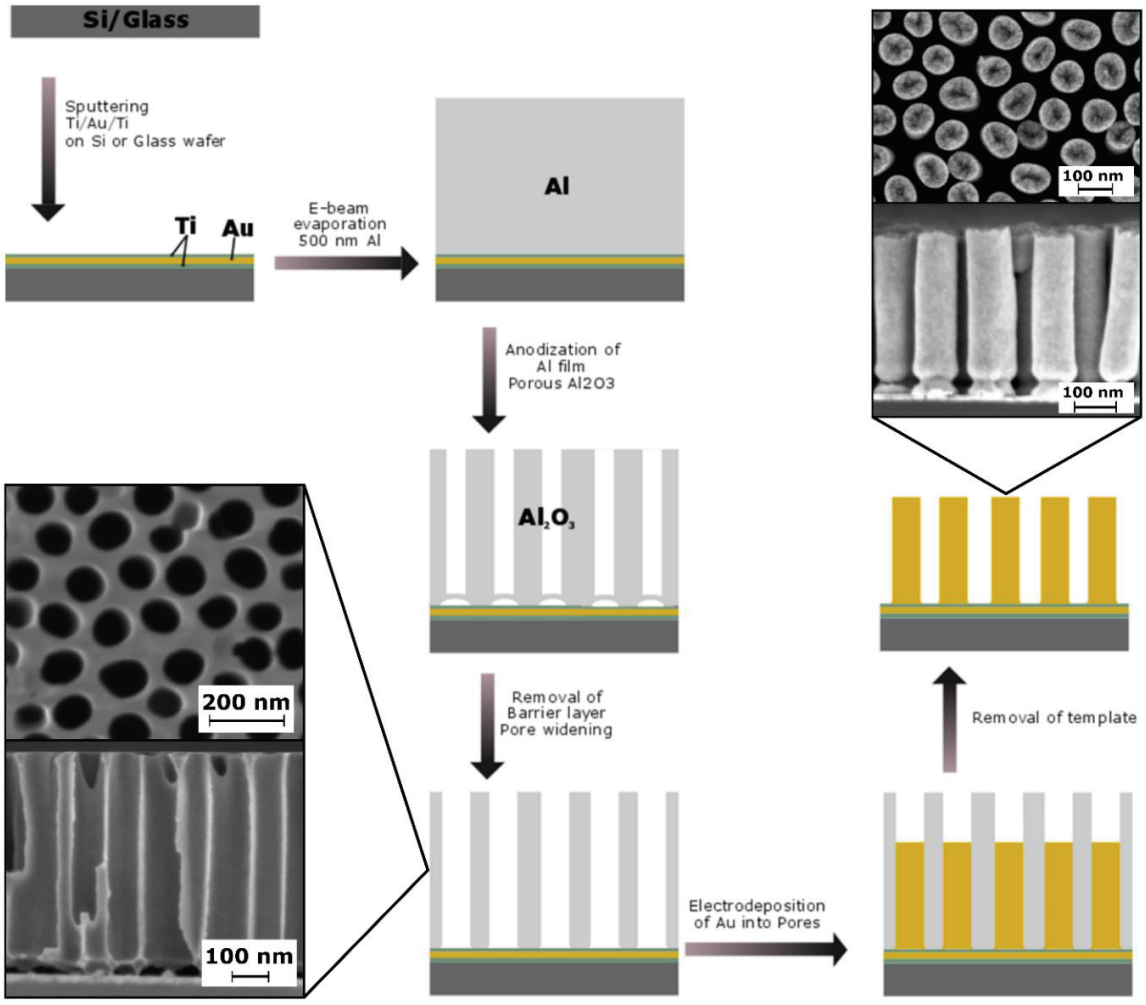

Figure 3.9. Schematic representation of the complete process, from the making of the templates to the nanorods electrodeposition.

3.3 Characterization methods

3.3.1 Scanning Electron Microscopy

Scanning electron microscopy (SEM) is crucial for nanomaterial characterization. Owing to its high resolution, SEM provides good knowledge about the morphology, size, and shape of nanostructures. SEM utilizes an accelerated electron beam, which interacts with the sample in terms of collisions between electrons and atoms of the sample, leading to radiation emission (such as secondary electrons, backscatter electrons, Auger electrons, X-rays) [19]. These emitted radiations are detected by suitable detectors and image processing programs to construct an image of the scanned area. The electron beam is directed onto the sample surface by an acceleration voltage,

which controls the penetration depth of the sample. SEM operates in a high-vacuum medium for ensuring that electrons reach the substrate without interference.

Secondary electrons (SE) are low-energy electrons that are ejected by an incident beam from the valence or conduction band of atoms and are collected; these collected electrons provide information about the sample topography [19]. When beam electrons exhibit high energy, they penetrate the atoms, interact with core electrons, and are ejected as secondary electrons. The atom needs to find its stability by electron transition to fill the secondary electrons band, leading to the emission of X-ray radiation [19]. Every atom has its own characteristic X-rays; therefore, the emitted X-rays provide information about the composition of the scanned sample (energy-dispersive X-ray spectroscopy). Backscattered electrons (BSE) are incident accelerated electrons that are elastically reflected or backscattered by the atom. These BSEs are sensitive to the atomic number of the scanned sample as heavy atoms backscatter electrons more strongly than light atoms, leading to a difference in the contrast between different areas of the sample (heavier atoms appear brighter); this provides information about the sample composition [19].

In this thesis, structure morphologies were characterized by high-resolution SEM from Zeiss (SEM Ultra Zeiss, Germany), equipped with energy-dispersive X-ray spectroscopy from INCAx-act (Oxford Instruments, UK).

3.3.2 X-ray Diffraction (XRD)

X-ray diffraction (XRD) is a material characterization method based on matter–light interaction by the diffraction of an incident X-ray by matter. It is a non-destructive method and permits rapid analysis to identify unknown matter, determine its crystalline phase, lattice parameters, and particle sizes. Diffraction only occurs if the incident X-ray wavelength is of the same order of magnitude as that of the spacing between crystal planes (d-spacing). When the material surface is examined by X-rays, the atom electronic cloud is shifted. This displacement leads to the re-emission of an electromagnetic wave with the same frequency as that of the incident X-ray (Rayleigh scattering). A regular array of atoms generates an array of scattered waves, which interfere with each other, completely cancel each other in the most incidence direction (destructive interference), and amplify each other in some specific incidence directions. By varying the incidence angle of X-rays, only the direction that obeys Bragg's law (eq. 3.23) exhibits constructive interference. By recording the diffraction pattern depending on the diffraction angle, the structure

of the analyzed crystal can be determined, as crystals always exhibit sharp distinct peaks unlike amorphous materials, which do not exhibit distinct peaks [20,21].

$$2d_{hkl}\sin\theta = n\lambda \qquad 3.23$$

d is the spacing between the crystal planes, θ is the incident angle, λ is the X-ray wavelength.

In this thesis, all the nanostructures were characterized by XRD on an X'Pert PRO diffractometer (PANalytical, Holland). The grazing incidence diffraction mode (θ = 1°) helps with the analysis of thin materials via the minimization of the X-ray penetration depth and thus the contribution of support substrates. The X-ray wavelength λ is 1.5418 Å.

3.3.3 Electrochemical Characterization

Applications of electrocatalysts as fuel-cell electrodes require electrochemical testing, particularly cyclic voltammetry and chronoamperometry. The measurement setup comprises three electrodes. Electrocatalysts, a Pt foil, and a hydrogen electrode serve as the working electrode, counter electrode, and reference electrode, respectively. The reference electrode must be as close as possible to the working electrode to avoid voltage drop. The used hydrogen reference electrode (Hydroflex from Gaskatel) exhibits a pH-dependent potential difference to the standard hydrogen electrode (SHE or NHE). This difference at room temperatures is expressed as follows:

$$E_{correction} = -(0.059 \cdot pH)\ V \qquad 3.24$$

- **Cyclic Voltammetry**

Electrochemical characterization of different reactions occurring on an electrocatalyst surface can be performed via the study of the behavior of the measured current as a function of the applied potential in an electrochemical cell, which is known as cyclic voltammetry. The potential is linearly varied to the working electrode (electrocatalyst) relative to a reference electrode, and the charge transfer between the working and counter electrodes is recorded using a potentiostat. The obtained current–voltage plot is called voltammogram. CV is mostly employed for the examination of oxidation/reduction events of a chemical substance on electrocatalysts, affording the exact potential at which the reaction occurs. In addition, CV is a tool for the spectroscopy of other complicated reactions such as adsorption/desorption and their involved reactions. Therefore, CV is a powerful

tool for studying different reactions occurring on the electrocatalysts and understanding their mechanisms. CV is a composition of two cycles of linear sweep voltammetry (LSV), where the electrocatalyst potential is swept from a starting potential E_i to an ending potential E_e. Then, a reversed LSV is swept back to the starting potential E_i. CV is controlled by a potentiostat with a constant scan rate dE/dt.

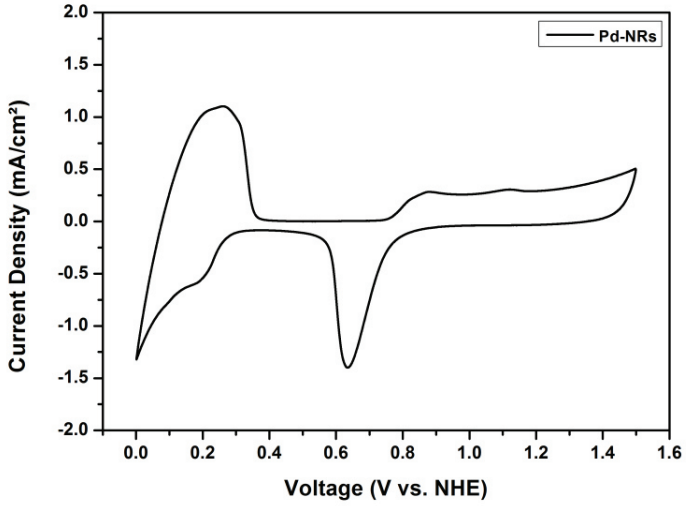

Figure 3.10. Cyclic voltammetry of Pd-NRs in 0.5 M H_2SO_4.

Figure 3.10 shows an exemplary CV of the Pd electrode in 0.5 M sulfuric acid. In forward-scan LSV, the increase in the current is observed at 0.26 V, corresponding to the hydrogen desorption due to one-electron transfer. As the potential is swept more positive, another peak in the current at ~0.88 V is observed due to the oxidation of Pd to PdO. In the backward scan (reverse LSV), the reduction of PdO occurs at 0.6 V, followed by hydrogen adsorption.

- **Chronoamperometry**

Chronoamperometry involves the variation of current as a function of time. Chronoamperometry is performed by maintaining the applied potential on the electrocatalysts and measuring the anodic/cathodic current. Thus, the Faradic current (current generated from oxidation and redaction) behavior is recorded as a function of time. For heterogeneous electrocatalysts, chronoamperometry permits the study of an electrocatalytic process lifetime, namely, at a desired potential, the lifetime during which electrocatalysts will stay active for the electrooxidation of a

chemical substance before it loses its activity either by poisoning or becoming unstable (dissolution)...

- **Tafel plot**

The Tafel plots show the dependence between the overpotential and current density. The Tafel analysis leads to understanding of the mechanisms controlling HER by analyzing the Tafel slope and exchange current density. Generally, the Butler–Volmer equation (eq. x3.25) describes the current behavior as a function of the voltage of electrochemical redox reactions (cathodic and anodic reactions) [22]:

Butler-Volmer: $j = j_0\{exp(-\alpha f\eta) - exp\big((1-\alpha)f\eta\big)\}$ 3.25

A is the transfer coefficient, $f = {}^{F}/_{RT}$ (F is the Faraday's constant, R is the universal gas constant, and T is the absolute temperature).

At a negative overpotential, the equation is simplified as follows:

$$j = j_0\{exp(-\alpha f\eta)\} \quad 3.26$$

Then, the cathodic reaction can be expressed as follows:

$$\eta = \frac{RT}{\alpha F} ln(j_0) - \frac{RT}{\alpha F} ln(j) \quad 3.27$$

Moreover, as:

$$\eta = a - b\ log(j) \quad 3.28$$

b is the Tafel slope, and J_0 is the exchange current density.

3.4 First Principal calculations

Density functional theory (DFT) is a quantum calculation method that is widely used to calculate electronic structures of matter. DFT provides accurate, predictive results for physical and chemical properties of matter [23,24]. The general concept of DFT is that the energy of a system can be expressed as function of electron density; this concept was demonstrated to be accurate by Kohn

and Sham [25,26]. The use of DFT can simplify the resolution of the Schrodinger equation of interacting N bodies (N variables) to an equation that depends only on the electronic density. The electronic density depends on three spatial coordinates. DFT provides a theoretical basis for the band structure calculation of a system. Studies revealed that the electronic density of a system permits the calculation of all its ground-state properties.

DFT requires some approximations to determine the energy of a system. Local density approximation (LDA) is the simplest approximation, which considers the electrons as a local homogeneous gas [25,26]. LDA is not applicable for a highly inhomogeneous system as it overestimates binding energies inside molecules and underestimates lattice parameters of crystals. To overcome limitations of the LDA approximation, gradient generalized approximation (GGA) considers that the energy is a spatial gradient of the ground-state electron density or exchange correlation energy instead of treating it as a homogenous function [25,26]. GGA corrects the estimated binding energies in molecules obtained by LDA, leading to the high precision of system energies. However, GGA exhibits some limitations for d and f orbitals electrons due to their high correlation; also, it cannot describe long-range interactions such as van der Waals interactions.

In this thesis, the Quantum ESPRESSO package was used, which is an open-source package based on DFT in the framework of GGA and projector-augmented wave potentials [27].

3.5 References

[1] M. Aliofkhazraei, Handbook of Nanoparticles, *Springer* (2016), ISBN 9783319153384.

[2] J. A. Gallego-Juárez, K. F. Graff, Power Ultrasonics Applications of High-Intensity Ultrasound, *Woodhead Publishing* (2015), ISBN 9781782420286.

[3] G. Chatel, J. C. Colmenares, Sonochemistry: from Basic Principles to Innovative Applications, *Topics in Current Chemistry* 375 (2017) 8.

[4] H. Xu, B. W. Zeiger, K. S. Suslick, Sonochemical synthesis of nanomaterials, *Chemical Society Reviews* 42 (2013) 2555.

[5] R. Sander, Compilation of Henry's law constants (version 4.0) for water as solvent, *Atmospheric Chemistry and Physics* 15 (2015) 4399.

[6] K. Okitsu, M. Ashokkumar, F. Grieser, Sonochemical Synthesis of Gold Nanoparticles: Effects of Ultrasound Frequency, *Journal of Physical Chemistry B* 109 (2005) 44.

[7] Y. Mizukoshi, R. Oshima, Y. Maeda, Y. Nagata, Preparation of Platinum Nanoparticles by Sonochemical Reduction of the Pt(II) Ion, *Langmuir* 15 (1999) 2733.

[8] D. M. Mattox, R. E. Cuthrell, C. R. Peeples, P. L. Dreike, Design and performance of a moveable-post Cathode Magnetron Sputtering System for making PBFA II accelerator ion sources, Surface *Coatings Technology* 33 (1987) 425.

[9] D. M. Mattox, Handbook of Physical Vapor Deposition (PVD) Processing, *Elsevier* (2010), ISBN 9780815520375.

[10] J. A. Thornton, High rate sputtering techniques, *Thin Solid Films* 80 (1981) 1.

[11] D. L. Smith, Thin Film Deposition, Principles and Practice, *McGraw-Hill* (1995), ISBN 9870070585027.

[12] A. Anders, Discharge physics of high power impulse magnetron sputtering, *Surface and Coatings Technology* 205 (2011) S1.

[13] N. Berger, M. Es-Souni, Understanding and Shaping the Morphology of the Barrier Layer of Supported Porous Anodized Alumina on Gold Underlayer, *Langmuir* 32 (2016) 6985.

[14] N. Berger, S. Habouti, H.-G. Rubahn, M. Es-Souni, On-substrate fabrication of porous Al2O3 templates with tunable pore diameters and interpore distances, *Applied Physics A* 122 (2016) 192.

[15] M. Es-Souni, S. Habouti, Ordered nanomaterial thin films via supported anodized alumina templates, *Frontiers in Materials* 1 (2014) 19.

[16] S. Habouti, Herstellung substratgestützter, nanoporöser Aluminiumoxid-Template und ihre Anwendung für die Präaparation von hochezienten SERS-Substraten, Dissertation, 2014, Technischen Fakultät der Christian-Albrecht-Universität zu Kiel.

[17] F. I. Dar, S. Habouti, R. Minch, M. Dietze, M. Es-Souni, Morphology control of 1D noble metal nano/heterostructures towards multi-functionality, *Journal of Materials Chemistry* 22 (2012) 8671.

[18] S. Habouti, M. Es-Souni, Au-NRs / VO2-NPs nanocomposites supported on glas substrates: Microstructure and optical properties, *CrystEngComm* 16 (2014) 3068.

[19] S. Thomas, R. Thomas, A. K. Zachariah, R. K. Mishra, Microscopy Methods in Nanomaterials Characterization: A volume in Micro and Nano Technologies, *Elsevier* (2017), ISBN 9780323461412.

[20] V.S. Ramachandran, J. J. Beaudoin, Handbook of Analytical Techniques in Concrete Science and Technology, *Elsevier* (2001), ISBN 9780815514374

[21] K. H. J. Buschow, M. C. Flemings, E. J. Kramer, P. Veyssière, R. W. Cahn, B. Ilschner, S. Mahajan, Encyclopedia of Materials: Science and Technology, *Pergamon* (2001), ISBN 9780080431529.

[22] T. Shinagawa, A. T. Garcia-Esparza, K. Takanabe, Insight on Tafel Slopes from A Microkinetic Analysis of Aqueous Electrocatalysis For Energy Conversion, *Scientific Reports* 5 (2015) 13801.

[23] P. Politzer, Jorge Seminario, Modern Density Functional Theory: A Tool for Chemistry, *Elsevier* (1995), ISBN 9780080536705.

[24] D. Sholl, J. A. Steckel, Density Functional Theory: A Practical Introduction, *Wiley* (2009), ISBN 9780470373170.

[25] J. Sabin, E. Brandas, M. Zerner, Advances in Density Functional Theory, *Academic Press* (1998), ISBN 9780120348329.

[26] T. Tsuneda, Density Functional Theory in Quantum Chemistry, *Springer* (2014), ISBN 9784431548249.

[27] P. Giannozzi, S. Baroni, N. Bonini, M. Calandra, R. Car, C. Cavazzoni, D. Ceresoli, G. L. Chiarotti, M. Cococcioni, I. Dabo, A. Dal Corso, S. De Gironcoli, S. Fabris, G. Fratesi, R. Gebauer, U. Gerstmann, C. Gougoussis, A. Kokalj, M. Lazzeri, L. Martin-Samos, N. Marzari, F. Mauri, R. Mazzarello, S. Paolini, A. Pasquarello, L. Paulatto, C. Sbraccia, S. Scandolo, G. Sclauzero, A. P. Seitsonen, A. Smogunov, P. Umari and R. M. Wentzcovitch, *Journal of Physics: Condensed Matter* 21 (2009) 395502.

4 “Noble metal NPs and nanoalloys by sonochemistry directly processed on nanocarbon and TiN substrates from aqueous solutions”

Ayoub Laghrissi, Claus-Henning Solterbeck, Dimitri Schopf, Mohammed Es-Souni

IMST Institute for Materials and Surface Technology, University of Applied Sciences Kiel, Kiel, Schleswig-Holstein, Germany

[DOI: 10.1016/j.ultsonch.2018.10.034] Reproduced by permission of Elsevier

Noble-metal nanoparticles are critical in many applications, including biotechnology and catalysis. Their synthesis using cost-effective and sustainable methods is therefore the subject of intense research activities. Moreover, processing of nanoalloys with controlled compositions is highly desirable as nanoalloys that could exhibit superior properties than monolithic nanoparticles. In this paper, Au-nanoparticles (Au-NPs) and nanoalloys were processed on nanocarbon and TiN substrates by sonochemistry without the use of reducing agents. Further a simple laboratory cleaning ultrasonic device sufficed for the processing of NPs directly from an aqueous precursor solution, with no requirement of a surfactant. The main results were as follows: the successful deposition of Au-NPs, AuPd-NPs, and PtPd-NPs. Notably, the underlying mechanisms for the formation of noble-metal NPs were suggested. In the absence of a substrate, nanoparticles were not formed in solution, indicating that the substrate serves as a mediator for the reduction of nanoparticles. This is possible if reducing radicals are formed on the substrate surface. The electrocatalytic activity of AuPd-NPs for the oxidation of formic acid was examined (~4 $mA \cdot cm^{-2}$ corresponding to 400 A/g for AuPd). The high current density is related to nanoparticle size and ligands effects between Au and Pd.

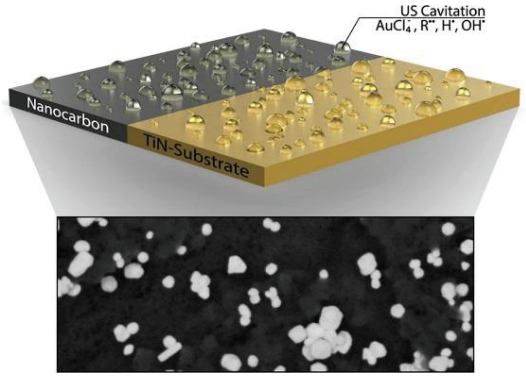

Prof. Dr. Mohammed Es-Souni designed the underlying concept. The author of the dissertation carried out the experiments and evaluated them. C. -H. Solterbeck helped in the electrochemical measurements, D. Schopf prepared the nanocarbon substrates. The author prepared the first draft and Prof. Dr. Mohammed Es-Souni validated the results and corrected the manuscript.

Ultrasonics - Sonochemistry 51 (2019) 138–144

Contents lists available at ScienceDirect

Ultrasonics - Sonochemistry

journal homepage: www.elsevier.com/locate/ultson

Noble metal NPs and nanoalloys by sonochemistry directly processed on nanocarbon and TiN substrates from aqueous solutions

Ayoub Laghrissi, Claus-Henning Solterbeck, Dimitri Schopf, Mohammed Es-Souni*

IMST Institute for Materials and Surface Technology, University of Applied Sciences Kiel, Kiel, Schleswig-Holstein, Germany

ARTICLE INFO

Keywords:
Sonochemistry
Noble metal
Au nanoparticles
AuPd nanoalloy
AuPt nanoalloy
Nanocarbon
Titanium nitride

ABSTRACT

The sonochemical processing of nanomaterials in a solution is well established and has been advantageously used for a variety of nanomaterials and morphologies thereof. In general, high energy and high frequency ultrasound is applied to a solution containing the ionic species of the elements to be reduced as well as a certain amount of reducing chemicals. For further applications such as catalysis washing, filtering, dispersion and mounting on or mixing in a substrate are necessary. A sonochemical processing of nanomaterials directly on a substrate could make all these steps obsolete. Herein we show that noble metal and nanoalloy nanoparticles (NPs) can directly be processed on nanocarbon and titanium nitride surfaces using a simple ultrasound laboratory cleaner in aqueous solutions that are free from any reducing chemicals. The process is demonstrated on Au-NPs and nanoalloys of AuPd and PdPt which form a dense distribution on the substrate surface. To illustrate the catalytic activity of the NPs, the electrocatalytic performance of one AuPd-nanoalloy is demonstrated. The results are discussed in terms of reduction phenomena occurring at the interface between the ultrasonic cavitation and the substrate. We think that these reduction phenomena are mediated by the formation of reducing radicals at the substrate surface that are in turn driven by $^{\cdot}OH$ radicals from water sonolysis. Electrochemical current measurement at 0 V seem to support the existence of reducing currents during measurements under chopped ultrasound in an aqueous solution of $HAuCl_4$ in comparison to measurements in water.

1. Introduction

It is of common knowledge that nanomaterials are of paramount importance in many key applications, including catalysis, safety, sensors and biomedical technology [1]. In particular, noble metal nanomaterials have been successfully used in biomedical sensing and catalysis because of their stability in various media and eventually their biocompatibility. For instance, and to cite only few applications, Au-nanoparticles (NP) and nanorods (NR) are well established in biomolecular sensing and the detection of trace molecules via surface enhanced spectroscopies [2,3], and Pt-NPs are very well known electrocatalysts in fuel cell technology [4]. A myriad of processing techniques can be used to process these nanomaterials, e.g via chemical reduction in solution [5], using template approaches [3,6,7], electron beam lithography [8] and many more.

Among the methods cited above, sonochemistry is well established. It has been used in the past and continues to be of high interest for the processing of nanoparticles of different materials in a solution. For instance, the review article by Xu et al. [9] describes the different materials and morphologies that can be obtained by sonochemistry and general mechanisms underlying reduction from solutions. More specifically, and regarding the nanomaterials of interest to this paper, Au and Pt NPs were processed in aqueous solutions containing the ionic species, surfactant and an alcohol (to facilitate reduction of noble metal ions), using high power ultrasonic sources [10,11]. Mizukoshi et al. [12] fabricated bimetallic Au–Pd nanoparticles from a solution containing a mixture of the ions, using a very similar procedure. Also, dendritic Pt@Au-NPs with a narrow size distribution were processed by applying an ultrasonic treatment to a solution containing both noble metal ions, ascorbic acid (as reducing agent) and a surfactant [13]. It appears that noble metal nanoparticles can be successfully processed in aqueous solutions containing small amounts of reducing agents, and that the ultrasound energy may be advantageously used to tailor particle size. However, the handling of the NPs may prove difficult as it requires centrifugation, filtration and dispersion on a support, e.g. for catalysis. Furthermore, a surfactant is required in order to prevent excessive agglomeration of the particles. The question then arises as to whether sonication of a solution in the presence of a suitable substrate

* Corresponding author at: IMST Institute for Materials and Surface Technology, University of Applied Sciences Kiel, Grenzstr. 3, 24149 Kiel, Schleswig-Holstein, Germany.
E-mail address: mohammed.es-souni@fh-kiel.de (M. Es-Souni).

https://doi.org/10.1016/j.ultsonch.2018.10.034
Received 18 September 2018; Received in revised form 15 October 2018; Accepted 25 October 2018
Available online 26 October 2018
1350-4177/

could potentially lead to the attachment of NPs onto the substrate surface. This could afford a method to directly process supported catalysts from an aqueous solution and would make all the necessary steps of filtration, etc. mentioned above needless. In the present paper we intend to demonstrate that this is exactly what happens when suitable substrates are chosen as supports.

Inspired by a recent reading of the paper by Guittonneau et al. [14] who showed that, mediated by water sonolysis, graphite may be decomposed by ultrasound down to organic radicals of different chemistry, we explored the possibility of attaching Au-NPs on nanocarbon surfaces while maintaining the ultrasound energy at a moderate level in order not to damage the surface. We surmised that the formation of reducing organic radicals on the nanocarbon surface could lead to the reduction of the Au-ions onto the surface dispensing of other reducing agents in the solution. The results depicted below demonstrate the validity of our hypothesis. It is further amazingly interesting to note that Au-NPs are easily and rapidly (90 s sonication is sufficient to treat a substrate) attached on to the surface when a nanocarbon substrate is sonicated in an aqueous solution of $HAuCl_4$ using a simple laboratory ultrasonic cleaner that allows to preserve the pristine surface. We extend the demonstration of the method to AuPd and PdPt nanoalloys, and to TiN terminated substrates. As one of the potential applications of our nanomaterials, we show the outstanding electrocatalytic properties of the processed AuPd nanoalloy NPs for the electrooxidation of formic acid. Besides the lack of any similar work reported so far, the novelty of our approach additionally resides in the simplicity, not least the versatility, of our method, its scaling-up possibility and cost-effectiveness, as large area substrates are easily modified.

2. Materials and methods

2.1. Reagents and materials

N,*N*-dimethylformamide (C_3H_7NO) was obtained from Carl Roth, Germany. Goodfellow supplied polyvinylidene fluoride granule and the TiN target. Ammonium nitrate, multi-walled carbon nanotubes (> 90% carbon basis) and H_2PtCl_6 were purchased from Sigma-Aldrich, Germany. Sulfuric acid was obtained from VWR chemicals, Formic acid from Fluka. $HAuCl_4$ and K_2PdCl_4 were purchased from abcr, Germany.

2.2. Substrate preparation

The processing of nanocarbon films involves different steps that are described in our previous papers [15,16]. In brief, first a precursor solution is prepared by dissolving 20 wt% of PVDF in DMF under stirring and heating (65 °C). To promote the formation of pores, 10 wt% of NH_4NO_3 is added after complete dissolution of PVDF (ca. 1 h). Further stirring for 2 h leads to a clear solution. In the third step 1% of multi-walled carbon nanotubes (MWCNTs) is added to the solution under further stirring. The PVDF–MWCNT-films are then dip-coated on mill-finished stainless steel substrates at a drawing speed of 2 mm/s. Curing was performed over night at 150 °C. The PVDF films thus obtained contain a high density of macropores [16]. The last step consists in the pyrolysis of the PVDF–MWCNT-films that is conducted under flowing nitrogen at 550 °C for 60 min. The resulting films are approximately 2 µm thick and largely preserve the original porosity of the pristine film. They consist of amorphous carbon interspersed with homogeneously distributed MWCNT. The mechanisms underlying film formation can be found in our previous papers [16,17].

The TiN films of approximately 500 nm thickness were deposited on stainless steel substrates, using magnetron sputtering from a TiN-target (Goodfellow, UK) in a physical vapour deposition device (PVD75, Lesker, USA). The substrate temperature was 250 °C and the deposition rate 0.07 Å/s at a power of 220 W.

Sonication experiments were performed using Bandelin Sonorex RK31 (Schalltec, Germany) bath with an ultrasonic nominal output of 40 W and ultrasonic frequency of 35 kHz. For the processing of Au-NPs, the substrate was immersed either in a 2 mM or 1 mM solution of $HAuCl_4$ and sonicated for 90 s. For the AuPd and PtPd NPs a 1:1 mixture of $HAuCl_4$ and K_2PdCl_4 (H_2PtCl_6) was used under the same conditions.

UV–Vis spectra were recorded versus H_2O, using a spectrophotometer (Lambda 35, Perkin-Elmer, USA). The sonochemical experiment was conducted in a 1 mM $HAuCl_4$ solution, because of absorption saturation of the $AuCl_4^-$ complex at higher concentrations.

The microstructure and morphology of the NPs were characterized with a high-resolution scanning electron microscope (SEM Ultra Plus, ZEISS, Germany) operating in the secondary (SE) and energy selective backscattered (ESB) electron mode. Microanalysis was performed in the SEM with an energy dispersive X-ray spectroscopy (EDS) package (INCAx-act, Oxford Instruments, UK).

The structure was characterized by X-ray diffraction (XRD, X'Pert Pro diffractometer PANalytical, Holland) in grazing incidence diffraction mode with constant $\theta = 1°$, using monochromatic CuKα radiation with $\lambda = 1.5418$ Å and variable scanning range (2θ). The device has a full width to half maximum resolution of 0.03°.

The electrochemical experiments were performed using an electrochemical workstation (ZAHNER IM6e, Kronach, Germany).

The electrochemical current vs. time measurements during sonication experiments were performed at 0 V either in deionized water or a 2 mM $HAuCl_4$ aqueous solution in a three-electrode set-up with a Pt mesh and HydroFlex (reversible H_2 reference electrode) as counter and reference electrodes, respectively. For the electrocatalytic experiments, first cyclic voltammetry (CV) measurements, also in a three-electrode set-up as above, were conducted in 0.5 M H_2SO_4. For formic acid (FA) electrooxidation, 0.5 M H_2SO_4 + 0.5 M HCOOH aqueous electrolyte was used. The potentials are referred to the normal hydrogen electrode (NHE).

All electrolytes in the electrochemical experiments were saturated with bubbling nitrogen for at least 30 min before use.

3. Results and discussion

Au-NPs on porous nanocarbon surfaces: When an aqueous solution containing 2 mM of $HAuCl_4$ is sonicated even for longer time, e.g. 300 s, in the absence of a substrate no Au-NP formation is observed, as inferred from the spectrophotometry of the solution which shows only the transitions of the $AuCl_4^-$ complex (Fig. 1) [12] that is in agreement

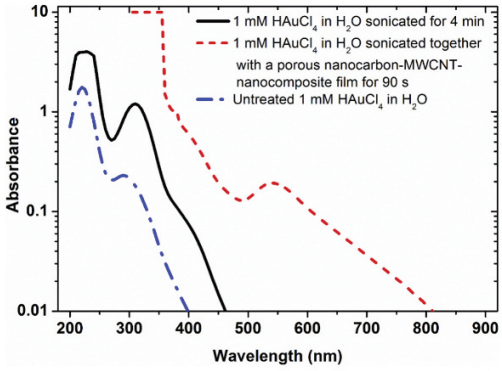

Fig. 1. A semi-logarithmic plot of absorbance vs. wave length of 1 mM $HAuCl_4$ solutions sonicated with and without the presence of the nanocarbon substrate in comparison to the absorbance of the pristine solution. The transitions below 450 nm belong to $AuCl_4^-$ ions (see Ref. [12] for more detail). The absorption peak centered at 550 nm is the plasmonic absorption peak of the Au-NPs that form in the solution.

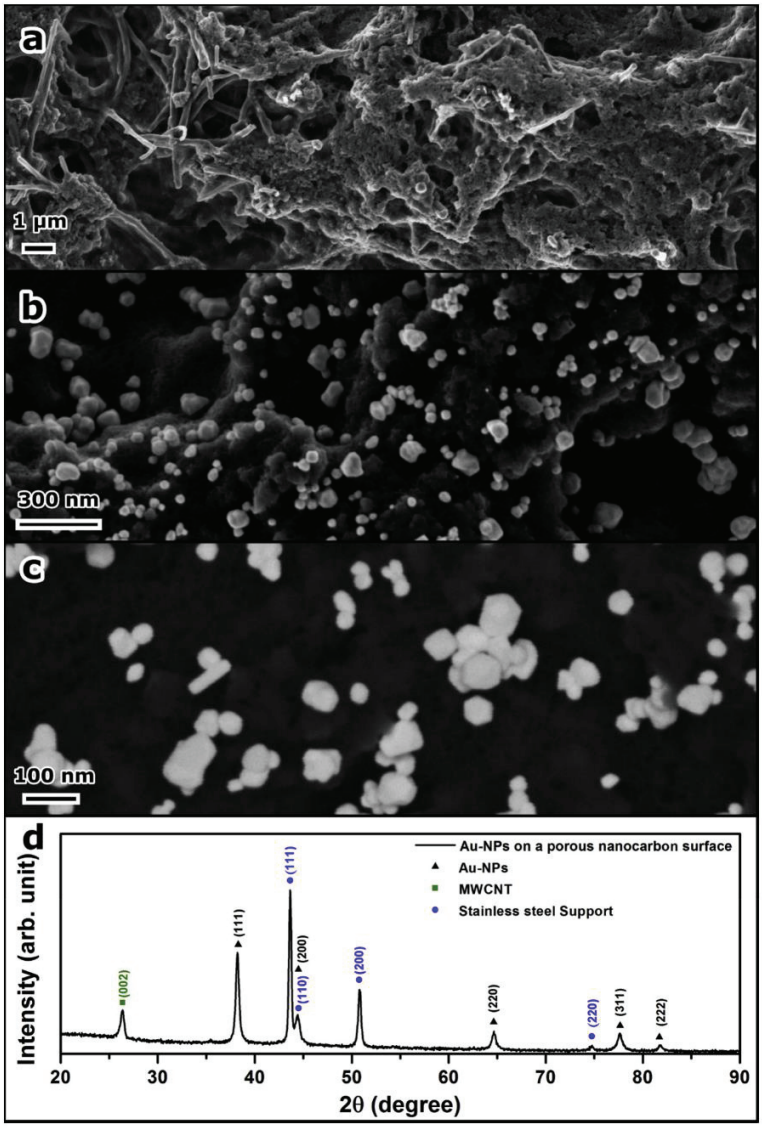

Fig. 2. (a) SEM secondary electron (SE) micrographs of the pristine porous nanocarbon surface. (b) SEM SE micrograph of Au-NPs on a porous nanocarbon surface. (c) High resolution backscattered electron (ESB) micrograph showing the different NP shapes that can be obtained. (d) XRD patterns of a sonicated nanocarbon substrate in a 2 mM solution of $HAuCl_4$. The support is an AISI316 (an austenitic stainless steel).

with previous reports [10–13]. However, in the presence of a porous nanocarbon substrate, Au-NPs readily form on the surface even after 60 s of sonication. This is demonstrated in Fig. 2 which shows a range of size distribution of NPs from 10 to 100 nm and various morphologies from spheroidal to faceted to nanorods. It should also be mentioned that, additionally, Au-NPs form in the solution, as illustrated in Fig. 1, where the Au-NP plasmonic peak centered at 550 nm is clearly visible. Fig. 2d shows the XRD patterns of the modified nanocarbon surface where the Au reflexions can be distinguished in addition to the reflexions of the stainless steel support and the 0 0 2 reflexion of the graphitized MWCNTs (the nanocarbon matrix is amorphous as reported in our previous work [16]). Apart from the 2 0 0 reflexion of Au which overlaps with the 1 1 0 substrate reflexion, all other Au reflexions are present denoting polycrystalline Au-NPs formation on the nanocarbon surface.

The method can be extended to process supported nanoalloy NPs simply from a mixture of aqueous solutions. This is shown in Fig. 3, exemplary for a PtPd and an AuPd nanoalloy that were fabricated by

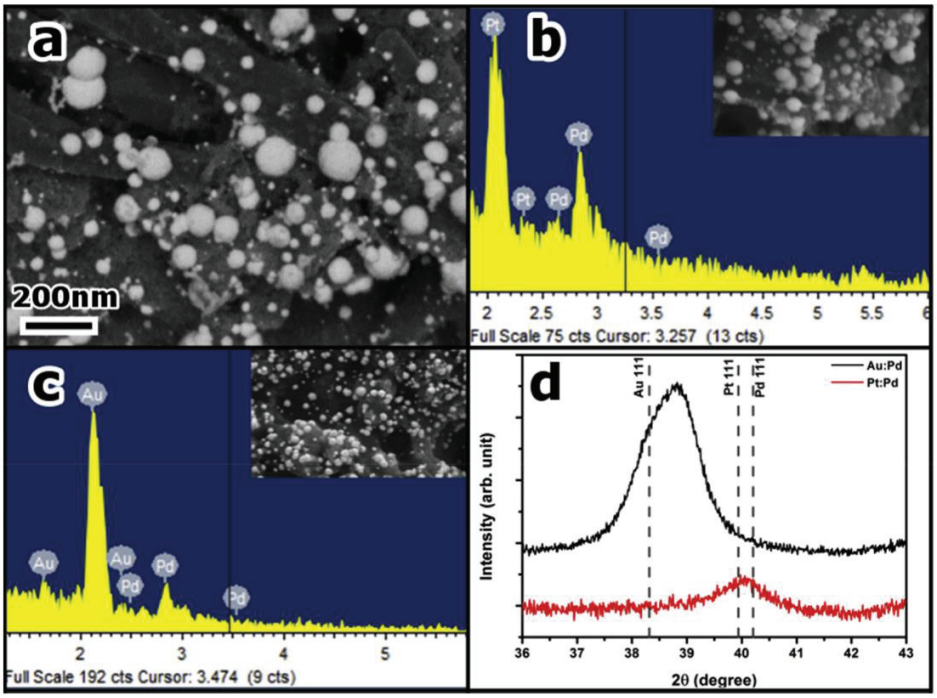

Fig. 3. (a) ESB micrograph of the PtPd nanoalloy NPs on a porous nanocarbon surface and corresponding EDS spectrum (b); (c) shows the EDS spectrum of the AuPd nanoalloy NPs (micrograph in the inset); (d) XRD patterns in the 2θ range of the 1 1 1 reflexions in grazing incidence mode.

mixing equal volumes of 2 mM solutions of H_2PtCl_6 and K_2PdCl_4, and $HAuCl_4$ and K_2PdCl_4, respectively. The XRD patterns obtained from AuPd and PtPd nanoalloy NPs in the 2θ range of the 1 1 1 reflexion are displayed in Fig. 3d. The broad peaks obtained lie between the corresponding 2θ positions of Au/Pd, and Pt/Pd, confirming the formation of AuPd and PtPd nanoalloys. The Pd and Pt concentration were obtained using the lattice parameters calculated from the 2θ positions of the 1 1 1 peaks and Vegard's law. The corresponding nanoalloys are AuPd22 and PtPd27.

The mechanisms underlying the sonochemical formation of NPs have been discussed in detail, and mainly involve the generation of highly reducing radicals, e.g. shown in the reactions (1)–(8) in Ref. [9]. With respect to noble metal NP formation so far reported, the presence of organic molecules or surfactants is indispensable for the generation of NPs in solution [9–13]. In the present paper we show that no NPs are observed when the aqueous solution is sonicated in the absence of the nanocarbon substrate, while when it is present, Au-NPs (and nanoalloy NPs) form both on the surface and in solution. This implies that the substrate must mediate the reduction of the noble metal ions, following one of two possible mechanisms. In the first mechanism water sonolysis that results in the generation of highly reducing radicals $^{\cdot}OH$ and $^{\cdot}H$ in collapsing cavitation at the substrate surface leads to the reduction of noble metal ions, as depicted in Reactions (1)–(3). Especially $^{\cdot}H$ is characterized by a high reduction potential as derived from the standard potential of −2.3 V at pH = 0 of the redox reaction $^{\cdot}H + 1e^- \leftrightarrow H^+$.

$$H_2O \rightarrow {}^{\cdot}OH + {}^{\cdot}H \quad (1)$$

$$3\,{}^{\cdot}H + AuCl_4^- \rightarrow Au^0 + 3HCl + Cl^- \quad (2)$$

$$nAu^0 \rightarrow Au_n^0 \quad (3)$$

The second and more likely mechanism implies a surface modification of the nanocarbon by collapsing cavitation that could generate reducing organic species, following reactions (4) and (5) (e.g. Okitsu et al. [10]). Indeed, a recent report demonstrates that graphite subjected to high power ultrasonic radiation may decompose, yielding in the last stadium different organic products down to phenols, acids and CO_2 [14]. Although the ultrasonic power used in this work is relatively moderate and the sonication time rather short, it nonetheless imparts enough power for the cavitation to create hot spots at the nanocarbon surface; organic radicals could be generated and the noble metal ions are thought to be reduced at those hot spots, followed by nucleation and growth.

$$^{\cdot}OH + RH \rightarrow {}^{\cdot}R({}^{\cdot}{}^{\cdot}R) + H_2O \quad (4)$$

$$({}^{\cdot}R, {}^{\cdot}{}^{\cdot}R) + Au^{3+} \rightarrow Au^0 \quad (5)$$

($^{\cdot}R$, $^{\cdot}{}^{\cdot}R$) are reducing radicals at the nanocarbon surface. $^{\cdot}OH$ is from water sonolysis. Au nucleation follows Eq. (3).

TiN-terminated substrates have also been tested under the conditions illustrated above. The results obtained (Fig. 4), unambiguously show that Au-NPs and nanoalloy NPs also attach to the TiN surface without need of any extraneous reducing agent. A possible mechanism could be the reduction of noble metal ions with nitrogen containing radicals, e.g. NH and NH_2 radicals, accompanied by the oxidation of TiN. TiN is easily oxidized at temperatures down to 350 °C [18,19], with the formation of nitrogen. Considering the high temperatures and pressures inside the cavitation, $^{\cdot}OH$ and $^{\cdot}H$ may react with TiN, leading to the formation of NH and NH_2 radicals at the hot-spots of collapsing cavitation on the surface, thus allowing the reduction of noble metals at these sites. Following this reasoning, it is expected that other substrates,

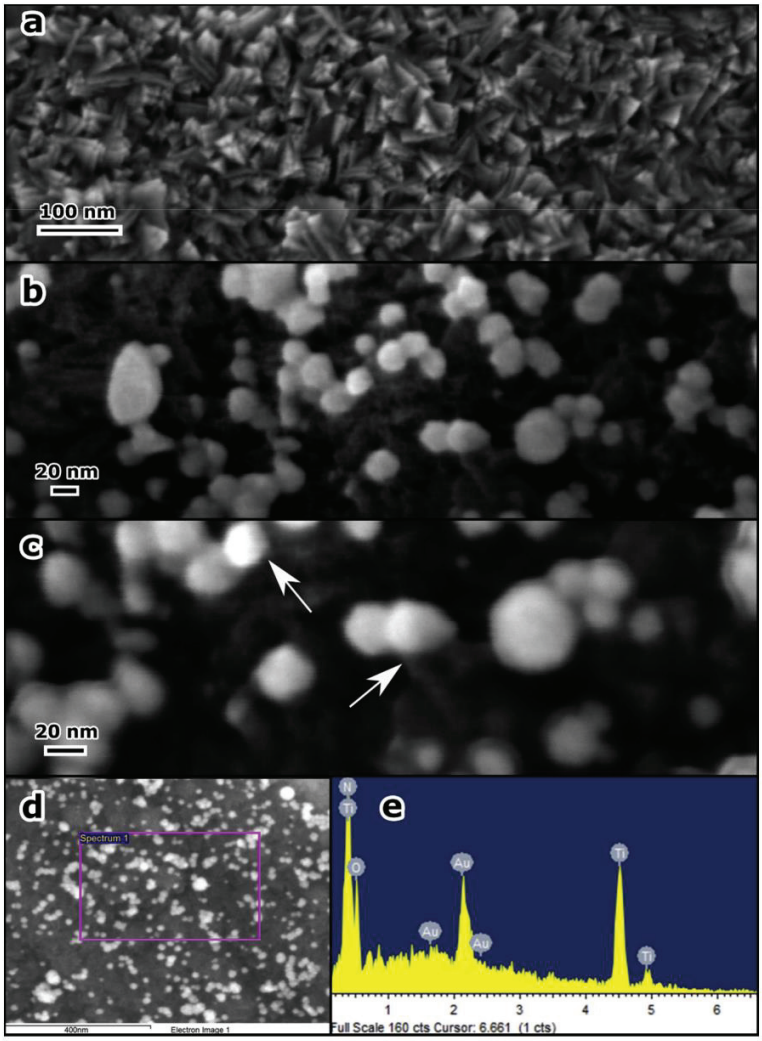

Fig. 4. (a) SEM SE micrograph of TiN surface showing the morphology of the TiN nanocrystallites. (b) Au-NPs attached to TiN surface. (c) BSE micrograph depicting a “continuous” interface between the TiN and the NPs (arrows). (d) and (e) EDS microanalysis: (d) analysed area, (e) EDS spectrum of Au-NPs on TiN.

such as diamond and DLC (diamond like carbon) coatings as well as other nitrides and carbides, may also be surface modified with noble metal ions, opening new perspectives for novel catalysts.

An attempt was made in order to understand what is occurring at the nanocarbon surface in terms of charges. Fig. 5 shows the current at 0 V, measured at the interface between deionized water and the working electrode (WE), i.e. nanocarbon, against a Pt foil of the same dimension, and using a standard hydrogen electrode (SHE) as the reference electrode (RE). Before switching on the ultrasound (US) a small and diminishing negative current is observed. Upon switching on US the current steeply increases towards positive values and eventually stabilizes at slightly smaller values. When US is switched off, there is a jump in the current towards negative values, but the original current is reached again after a certain, relatively short time. This behaviour is reproducible over the time range of the measurement (see black curve, Fig. 5). This indicates that oxidative processes are taking place at the interface between water and the WE. We surmise that collapsing cavitation and eventually sonolysis (Reaction (1)) lead to the oxidation of carbon speciesthe nature of which cannot yet be determined. But according to Guittonneau et al. [14] many oxidation products, mainly carbonate, can form through the action of ˙OH radicals (although the US power and frequency used in the present work are by no means matching theirs). When a 2 mM $HAuCl_4$ is used, we first observe a high negative current that appears to be stable in the time window shown. Switching on US results in the reverse behaviour depicted in water (compare the black and blue curve in Fig. 5), with steep and substantial decrease (towards negative values) of the measured current at the WE. The process is repeated several times with similar results. Regardless of

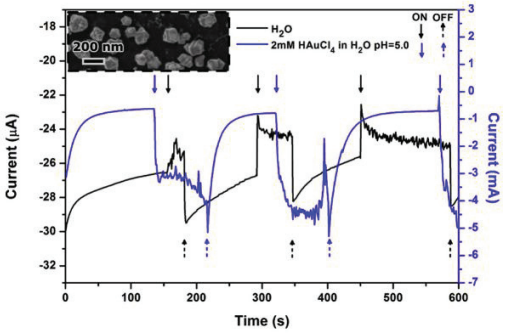

Fig. 5. Current-time behaviour measured at a potential of 0 V on a nanocarbon surface under chopped sonication in H_2O and 2 mM $HAuCl_4$. The inset shows a SEM micrograph of the nanocarbon surface after the chopped sonication in $HAuCl_4$. A high density of large Au particles is observed. (For interpretation of the references to color in this figure legend, the reader is referred to the web version of this article.)

the complexity of the system, comparison of the behaviour of the substrate in water to that in the Au-electrolyte suggests that when US is on, reductive processes take place at the interface between the nanocarbon and the Au-electrolyte, and these reductive processes mostly are related to the Au ion reduction at the nanocarbon surface, as evidenced by the microscopic observations (see also inset in Fig. 5). Although the results described above are probably contributed by complex electrochemical processes, they nonetheless constitute a first qualitative explanation of what is happening at collapsing cavitation on the substrate surface and how reduction at these sites occurs.

Finally, we explore the catalytic activity of the processed NPs on nanocarbon as one of the potential applications of these materials, focusing on the AuPd22 nanoalloy NPs. We target the electrooxidation of formic acid, because Pd and its alloys are very well-known catalysts for this reaction [20,21]. Fig. 6 illustrates the current–voltage (CV) curves in 0.5 M H_2SO_4 (a) and in 0.5 M H_2SO_4 + HCOOH (b). The CV curve in (a) shows in forward sweep only one oxidation peak corresponding to the AuPd alloy with an oxidation voltage intermediate between that of Au (approximately 1 V) and Pd (approximately 0.6 V). On backward sweep, however, we notice two distinct reduction peaks, a behavior that is known for Pd-alloys with less than 40%Pd [22]. The CV of the electrooxidation of formic acid (Fig. 6b), shows an extended activity range from approximately 0.1 V to 1.1 V. The forward and backward sweep curves describe a hysteresis with a smaller peak current density on backward sweep, while the activity range and the peak positions

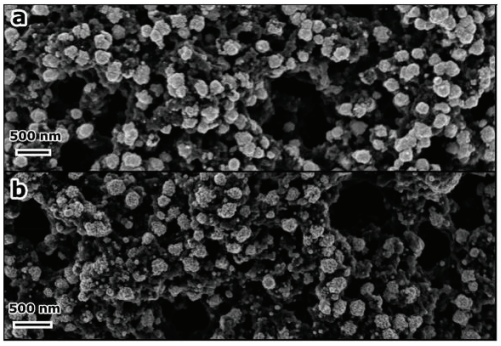

Fig. 7. SEM SE micrographs of AuPd22-NPs attached to a nanocarbon surface: (a) before, and (b) after the CV and electrocatalytic measurements.

remain very similar. This behavior is specific to the direct oxidation path and suggests a lower tendency to site poisoning by CO and intermediate oxidation species [23]. This might be amenable to the presence of Au atoms neighboring the active Pd atoms that should promote the oxidation of CO [24,25]. As to the magnitude of activity, the current density in Fig. 6b is normalized by the geometric surface area, and already suggests a high activity, taking into account that only the surface is modified with the nanoalloy NPs. A cursory estimate of the mass of metal contained in 0.72 cm^2 (the geometric area used in this work), using image analysis and an alloy density of 17.69 g/cm^3, yields a maximum value of 41 μg, which leaves us with a specific peak current of 400 A/g that lies in the upper range of what is reported so far for AuPd nanoalloys [26]. Fig. 7 shows the SEM micrographs of the AuPd22-NPs before and after the CV and electrocatalytic measurements. Barely a difference between the two surfaces can be noticed even after multiple sweeps in 0.5 M H_2SO_4 electrolytes and a voltage of up to 1.2 V, which attests to the stability of our electrocatalyst.

4. Conclusions

In the present work a simple sonochemical method is demonstrated that allows the reduction of noble metal ions directly on nanocarbon and TiN-terminated surfaces. This reduction occurs in aqueous solutions of the noble metal ions or mixtures thereof, dispensing of any reducing agent and using a low power ultrasonic device, in the present case solely a laboratory ultrasonic cleaner. It is postulated that the formation of reducing radicals in cavitation on nanocarbon and TiN surfaces is responsible for the observed noble metal and nanoalloy

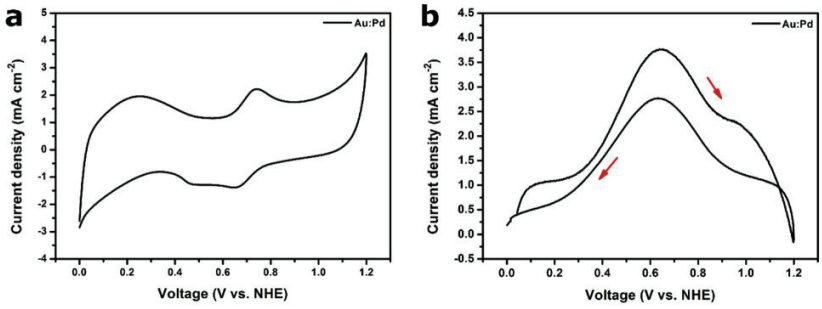

Fig. 6. (a) Cyclic voltammetry curves of the AuPd22 nanoalloy in 0.5 M H_2SO_4. (b) Current density vs. voltage of the AuPd22 sample electrodes in 0.5 M H_2SO_4 + 0.5 M HCOOH. The current is normalized by the geometrical surface area. Scan rate: 50 mV s^{-1}.

nanoparticles. Electrochemical current measurements at 0 V during chopped sonication seem to bolster this assumption. We demonstrate the method on Au, AuPd and PtPd-NPs, and show as an application example the electrocatalytic behavior of AuPd-NPs for the electro-oxidation of formic acid.

References

[1] C.M. Hussain, Handbook of Nanomaterials for Industrial Applications, Elsevier, 2018.

[2] B. Sepúlveda, P.C. Angelomé, L.M. Lechugaa, L.M. Liz-Marzán, LSPR-based nanobiosensors, Nano Today 4 (2009) 244–251, https://doi.org/10.1016/j.nantod.2009.04.001.

[3] S. Habouti, M. Mátéfi-Tempfli, C.-H. Solterbeck, Ma. Es-Souni, S. Mátéfi-Tempfli, M. Es-Souni, On-substrate, self-standing Au-nanorod arrays showing morphology controlled properties, Nano Today 6 (2011) 12–19, https://doi.org/10.1016/j.nantod.2010.11.001.

[4] M. Nesselberger, S. Ashton, J.C. Meier, I. Katsounaros, K.J.J. Mayrhofer, M. Arenz, The particle size effect on the oxygen reduction reaction activity of Pt catalysts: influence of electrolyte and relation to single crystal models, J. Am. Chem. Soc. 133 (2011) 17428–17433, https://doi.org/10.1021/ja207016u.

[5] S. Guo, E. Wang, Noble metal nanomaterials: controllable synthesis and application in fuel cells and analytical sensors, Nano Today 6 (2011) 240–264, https://doi.org/10.1016/j.nantod.2011.04.007.

[6] M.R. Jones, K.D. Osberg, R.J. Macfarlane, M.R. Langille, C.A. Mirkin, Templated techniques for the synthesis and assembly of plasmonic nanostructures, Chem. Rev. 111 (2011) 3736–3827, https://doi.org/10.1021/cr1004452.

[7] H. Wang, H.Y. Jeong, M. Imura, L. Wang, L. Radhakrishnan, N. Fujita, T. Castle, O. Terasaki, Y. Yamauchi, Shape- and size-controlled synthesis in hard templates: sophisticated chemical reduction for mesoporous monocrystalline platinum nanoparticles, J. Am. Chem. Soc. 133 (2011) 14526–14529, https://doi.org/10.1021/ja2058617.

[8] M.K. Corbierre, J. Beerens, R.B. Lennox, Gold nanoparticles generated by electron beam lithography of gold(I)-thiolate thin films, Chem. Mater. 17 (2005) 5774–5779, https://doi.org/10.1021/cm051085b.

[9] H. Xu, B.W. Zeiger, K.S. Suslick, Sonochemical synthesis of nanomaterials, Chem. Soc. Rev. 42 (2013) 2555–2567, https://doi.org/10.1007/978-1-4020-8903-9_33.

[10] K. Okitsu, M. Ashokkumar, F. Grieser, Sonochemical synthesis of gold nanoparticles: effects of ultrasound frequency, J. Phys. Chem. B Lett. 109 (2005) 20673–20675, https://doi.org/10.1021/jp0549374.

[11] Y. Mizukoshi, R. Oshima, Y. Maeda, Y. Nagata, Preparation of platinum nanoparticles by sonochemical reduction of the Pt(II) ion, Langmuir 15 (1999) 2733–2737, https://doi.org/10.1021/la9812121.

[12] Y. Mizukoshi, K. Okitsu, Y. Maeda, T.A. Yamamoto, R. Oshima, Y. Nagata, Sonochemical preparation of bimetallic nanoparticles of gold/palladium in aqueous solution, J. Phys. Chem. B 101 (1997) 7033–7037, https://doi.org/10.1021/jp9638090.

[13] H. Ataee-Esfahani, L. Wang, Y. Nemoto, Y. Yamauchi, Synthesis of bimetallic Au@Pt nanoparticles with Au core and nanostructured Pt shell toward highly active electrocatalysts, Chem. Mater. 22 (2010) 6310–6318, https://doi.org/10.1021/cm102074w.

[14] F. Guittonneau, A. Abdelouas, B. Grambow, S. Huclier, The effect of high power ultrasound on an aqueous suspension of graphite, Ultrason. Sonochem. 17 (2010) 391–398, https://doi.org/10.1016/j.ultsonch.2009.08.011.

[15] M. Es-Souni, D. Schopf, C.-H. Solterbeck, M. Dietze, Novel approach to the processing of meso-macroporous thin films of graphite and in situ graphite–noble metal nanocomposites, RSC Adv. 4 (2014) 17748–17752, https://doi.org/10.1039/C4RA00716F.

[16] D. Schopf, M. Es-Souni, Thin film nanocarbon composites for supercapacitor applications, Carbon 115 (2017) 449–459, https://doi.org/10.1016/j.carbon.2017.01.027.

[17] M. Es-Souni, Mar. Es-Souni, Matthias Dietze, A universal, template-free approach to porous oxide and polymer film processing, RSC Adv. 1 (2011) 579–583, https://doi.org/10.1039/c1ra00200g.

[18] F.O. Rice, M. Freamo, The formation of the imine radical in the electrical discharge, J. Am. Chem. Soc. 75 (1953) 548–549, https://doi.org/10.1021/ja01099a010.

[19] N.C. Saha, H.G. Tompkins, Titanium nitride oxidation chemistry: an X-ray photoelectron spectroscopy study, J. App. Phys. 72 (1992) 3072–3079, https://doi.org/10.1063/1.351465.

[20] N.V. Rees, R.G. Compton, Sustainable energy: a review of formic acid electrochemical fuel cells, J. Solid State Electrochem. 15 (2011) 2095–2100, https://doi.org/10.1007/s10008-011-1398-4.

[21] Md.A. Matin, J.H. Jang, Y.U. Kwon, PdM nanoparticles (M = Ni Co, Fe, Mn) with high activity and stability in formic acid oxidation synthesized by sonochemical reactions, J. Power Sources 262 (2014) 356–363, https://doi.org/10.1016/j.jpowsour.2014.03.109.

[22] M. Lukaszewski, A. Czerwinski, Electrochemical behavior of palladium–gold alloys, Electrochim. Acta 48 (2003) 2435–2445, https://doi.org/10.1039/B306307K.

[23] M. Arenz, V. Stamenkovic, T.J. Schmidt, K. Wandelt, P.N. Ross, N.M. Markovic, The electro-oxidation of formic acid on Pt–Pd single crystal bimetallic surfaces, Phys. Chem. Chem. Phys. 5 (2003) 4242–4251, https://doi.org/10.1016/S0013-4686(03)00270-6.

[24] A.D. Daigle, J.J. BelBruno, Density functional theory study of the adsorption of oxygen atoms on gold (1 1 1), (1 0 0) and (2 1 1) surfaces, Surf. Sci. 605 (2011) 1313–1319, https://doi.org/10.1016/j.susc.2011.04.025.

[25] W. Zeng, J. Tang, P. Wang, Y. Pei, Density functional theory (DFT) studies of CO oxidation reaction on M13 and Au18M clusters (M = Au, Ag, Cu, Pt and Pd): the role of co-adsorbed CO molecule, RSC Adv. 6 (2016) 55867–55877, https://doi.org/10.1039/C6RA07566E.

[26] T. Maiyalagan, X. Wang, A. Manthiram, Highly active Pd and Pd–Au nanoparticles supported on functionalized graphene nanoplatelets for enhanced formic acid oxidation, RSC Adv. 4 (2014) 4028–4033, https://doi.org/10.1039/C3RA45262J.

5 “Layered Au-Pd-Au Nanorod Catalysts: Pd-layer Thickness Effects on Catalyst Performance”

Ayoub Laghrissi, Mohammed Es-Souni
IMST Institute for Materials and Surface Technology, University of Applied Sciences Kiel, Kiel, Schleswig-Holstein, Germany
[DOI: 10.1016/j.ijhydene.2019.04.105] Reproduced by permission of Elsevier

In the previous chapter a cost-effective and sustainable processing method for noble-metal NPs supported on two different substrates have been presented: “Noble metal NPs and nanoalloys by sonochemistry directly processed on nanocarbon and TiN substrates from aqueous solutions”. It has been also shown that AuPd-NPs were characterized by a high electrocatalytic activity for the oxidation of formic acid. In this chapter, layered 1D nanostructures consisting of Au/Pd/Au and Au/Pd nanorods were processed in AAO template thin films using sequential electrodeposition in aqueous electrolytes of Au and Pd, and varying the Pd layer thickness. The main impetus was the higher electrocatalytic properties of 1D nanostructures, and the outstanding effects of near- interface alloys on them reported in the literature. The main observation is the increasing electrocatalytic performance with decreasing Pd-layer thickness. Cyclic voltammetry reveals that the PdO reduction peak is shifted toward the Au reduction peak with decreasing Pd-layer thickness which indicates the formation of a near-interface PdAu alloy the effect of which is more pronounced when the Pd-layer thickness is decreased to 15 nm. In thinner layers, a high content of the PdAu alloy over pure Pd translates in the domination of the PdAu electrocatalytic activity. DFT calculations suggest that Au atoms in PdAu alloys are an oxidant for the CO adsorbed on the nearest Pd atoms, preventing the poisoning of the Pd active sites.

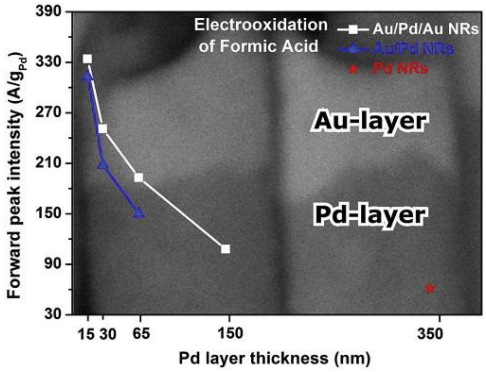

Prof. Dr. Mohammed Es-Souni designed the underlying concept. The author of the dissertation carried out the experiments and evaluated them. The author prepared the first draft and Prof. Dr. Mohammed Es-Souni validated the results and corrected the manuscript.

INTERNATIONAL JOURNAL OF HYDROGEN ENERGY 44 (2019) 14918–14926

Available online at www.sciencedirect.com

ScienceDirect

journal homepage: www.elsevier.com/locate/he

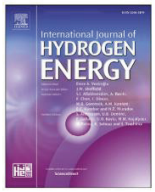

Layered Au-Pd-Au nanorod catalysts: Pd-layer thickness effects on catalyst performance

*Ayoub Laghrissi, Mohammed Es-Souni**

IMST Institute for Materials and Surface Technology, University of Applied Sciences Kiel, Kiel, Schleswig-Holstein, Germany

ARTICLE INFO

Article history:
Received 12 February 2019
Received in revised form
20 March 2019
Accepted 11 April 2019
Available online 4 May 2019

Keywords:
Au/Pd/Au nanostructure
Layered nanorod
CV behavior
Formic acid
Electrooxidation
CO adsorption

ABSTRACT

Au/Pd/Au and Au/Pd layered nanorods (NR) with different Pd thickness, down to 15 nm, are electrodeposited in Si-supported porous anodized aluminum thin film templates. These structures are, in contrast to Au-Pd core-shells, mechanically relaxed, so that chemical and electronic interaction effects between Au and Pd are expected to predominate in controlling their performance in the electrooxidation of formic acid. The XRD results are conclusive about the formation of pure metal layers, but a corrugated Au/Pd interface is revealed by scanning electron microscopy. The CV behavior of the different structures shows that the PdO reduction peak is shifted towards more noble values as the Pd thickness decreases. Regarding the electrocatalytic oxidation behavior there is a substantial increase in performance with decreasing Pd-layer thickness. It is further shown that the Au/Pd/Au nanostructures perform better than the Au/Pd bilayer structure for the same Pd layer thickness. Also the long term behavior is improved. Both CV and electrocatalytic behaviors are discussed in terms of interfacial intermixing between Pd and Au at the nanoscale and a higher interface contribution for thinner Pd layers.

Introduction

Noble metal catalysts play a prominent role in a variety of chemical processes, including chemical synthesis and energy harvesting [1–3]. For instance, fuel cell technology relies heavily on Pt nanoparticle catalysts or derivative structures thereof, e.g. alloys, core shell etc. [4–7] for oxygen reduction reaction (ORR) or methanol electrooxidation. One of the main motor for developing new catalysts is the necessity to reduce the Pt-loading, and hence cost, without all too much decreasing the reaction kinetics. Nørskov et al. [8] and Stephen et al. [9] show that catalyst performance may be boosted if one can design Pt-skin structures on a transition metal core, e.g. using an alloy or an intermetallic compound and heating them up to drive surface segregation of the noble metal. The mechanisms underlying the improvement of catalytic performance that, depending on core and ligand, translates in the so-called volcano effect were discussed in terms of compressive stresses arising from lattice mismatch between skin and underlying core and ligand effects. Both entail a change in the electronic structure of the noble metal, and in doing so mitigate the binding energy of intermediate reaction species. The design of core-shell nanoparticles, e.g. Pt@Ni [10–12], etc., has consequently seen an upsurge in research activities, although a large scatter in the results may be noted [13–15].

* *Corresponding author*. IMST Institute for Materials and Surface Technology, University of Applied Sciences Kiel, Grenzstr. 3, 24149 Kiel, Schleswig-Holstein, Germany.
E-mail address: mohammed.es-souni@fh-kiel.de (M. Es-Souni).
https://doi.org/10.1016/j.ijhydene.2019.04.105
0360-3199/

In the particular case of interest to the present work, namely Au/Pd structures and their application to electrooxidation, including that of formic acid (FA), there is few work mainly reporting on core-shell structures [16]. Montes de Oca et al. [17] report on Au-core-Pd shell nanoparticles with different Pd layer thickness and discuss their results with respect to strain effects. Their findings show that, while highly strained shells (very thin Pd layers, e.g. 1 nm) are characterized by equal forward and backward current density (for FA electrooxidation), relaxed structures (thicker Pd layers) have higher performance but also a higher backward current density that rather points to an indirect electrooxidation path of FA (see below). Overall, however, the electrooxidation performance is better than that of Pd-black. The authors explain their results with the occurrence of a polycrystalline Pd-structure with increasing Pd-thickness, thus affording more (100) planes with higher electrocatalytic activity. This contrasts with another work on similar nanostructures [18] that reports maximum activity for benzene alcohol electrooxidation (volcano effect) for one atomic Pd-layer covering Au. They argue that a minimum number of Pd atoms on the surface is required for the exothermic adsorption of the alcohol on the structure. Their results are rationalized in term of both strain and ligand effects, based on density functional theory (DFT) calculations. More work on Au/Pd shows that the thickness of the Pd-shell impacts the electrocatalytic performance, similarly to the results of Montes de Oca et al. [17] and Hsu et al. [19]. The shape of the underlying Au-NPs seems also to influence the electrocatalytic properties via structure control of the Pd-shell. Tetrahexahedral Au-cores purportedly promote the formation of polycrystalline Pd-shells with high index planes that are claimed to have better activity [20].

Au/Pd nanostructures are most widely applied to the electrocatalytic oxidation of FA. The overall reaction is given in Equations (1) and (2):

$$HCOOH \rightarrow 2H^+ + 2e^- + CO_2 \quad (1)$$

$$HCOOH \rightarrow CO_{ad} + H_2O \rightarrow CO_2 + 2H^+ + 2e^- \quad (2)$$

The oxidation of FA may follow two different paths [21,22]. The direct path as in Reaction (1) or the indirect path consisting of the dehydration of FA with the formation of adsorbed CO as intermediate product, Reaction (2). This results in specific electrochemical behavior on voltage sweep, e.g. a strong hysteresis in the forward and backward current densities for the indirect path. Pd catalysts usually behave in accordance with the direct path while for Pt the indirect path is rather favored, with consequent poisoning of the catalyst with site blocking species, among them CO [21].

Regardless of the targeted molecule, boosting catalyst performance has been in the focus of research in recent years, and nanomaterials with unusually high performance have been reported [23–25]. A particular interest has been devoted to core-shell structures [26–29], and nanoalloys [30,31], because they entail altering the electronic structure of the active metal (ligand effect) as discussed above. Such structures could lead to higher durability of the catalyst while decreasing the noble metal cost.

However, the brief literature review presented above about Au-Pd core-shell structure reveals a large scatter in the results with even contradictory findings, e.g. compare Montes de Oca et al. [17] and Silva et al. [18]. The question then arises as to whether electronic coupling (ligand effect), strain effects or crystallography control the electrocatalytic properties of Au-Pd nanostructures.

In the present work we explore an alternative structure based on on-substrate, layered NR of Au/Pd/Au with different Pd layer thickness, and investigate their electrocatalytic behavior in acidic FA solutions. The layered NRs of approximately 100 nm diameter were electrodeposited in an anodized aluminum oxide template film supported on silicon, using alternating aqueous baths of $HAuCl_4$ and K_2PdCl_4 (Au/Pd/Au). The Pd layer thickness was adjusted via controlling the deposition time. This procedure yields, regardless of the Pd-layer thickness, polycrystalline NRs with very similar structure. Because of the NR morphology the Pd-layers are relaxed, so that mechanical stresses are expected to be marginal. This should allow us to probe the effect of electronic coupling at the interface between Pd and Au while keeping the other effects (strain and structure) negligibly small.

Materials and methods

Synthesis and electrochemical measurements

Phosphoric acid 88%, oxalic acid dehydrates 99%, sodium hydroxide was purchased from Roth, Germany. Sulfuric acid was obtained from VWR chemicals, Formic acid from Fluka. And $HAuCl_4$ and K_2PdCl_4 from abcr, Germany.

Anodized aluminum oxide (AAO) template films supported on silicon were processed following the procedure described in detail in our previous work [32]. Briefly a 500 nm aluminum film is deposited on an Au/(6 nm)Ti(4 nm)/Si(wafer) heterostructure using electron beam evaporation in a PVD device (PVD75, Lesker, USA). Anodization is conducted in a two-electrode set-up in 0.2 M aqueous solution of oxalic acid under potentiostatic condition of 60 V using an electrochemical workstation (Keithley 2400 SM, Cleveland, OH, USA). A Pt foil was used as counter electrode. After anodization, barrier layer removal and pore widening are conducted in phosphoric acid (5 wt % in water) for 50 min at 30 °C.

The Au/Pd/Au NRs were grown into the pores by sequential electrodeposition from 8 mM $HAuCl_4$, and 10 mM K_2PdCl_4 aqueous electrolytes. A three-electrode set-up, with the Au/AAO template working electrode, a Pt counter electrode and an Ag/AgCl reference electrode, and an electrochemical workstation (Princeton Potentiostat/Galvanostat Model 263A, USA) were operated under potentiostatic conditions. Au is deposited at 0.1 V. Pd deposition was first initiated at −0.1 V for 100 s and subsequently the voltage was increased to 0.3 V for further deposition. After electrodeposition, the AAO template is dissolved in NaOH (5 wt % in water) to expose the nanostructures.

The microstructure and morphology of the NR were characterized with a high-resolution scanning electron microscope (SEM Ultra Plus, ZEISS, Germany) operating in the secondary (SE) and energy selective backscattered (ESB)

electron modes. The SEM is also equipped with an energy dispersive X-ray spectroscopy (EDS) package (INCAx-act, Oxford Instruments, UK).

The NR structure was characterized by X-ray diffraction (XRD, X'Pert Pro diffractometer PANalytical, Holland) in grazing incidence diffraction mode with constant $\theta = 1°$ using monochromatic CuKα radiation with $\lambda = 1.5418$ Å and a scanning range between 30° and 50° (2θ). The device has a full width to half maximum resolution of 0.03°.

An electrochemical workstation (ZAHNER IM6e, Kronach, Germany) was used for cyclic voltammetry (CV) measurements. The electrochemical experiments were performed in 0.5 M H_2SO_4 in a three-electrode set-up with a Pt mesh and HydroFlex (reversible H_2 reference electrode) as counter and reference electrodes, respectively. For FA electrooxidation, 0.5 M H_2SO_4 + 0.5 M HCOOH aqueous electrolyte was used. All potentials were referred to the normal hydrogen electrode (NHE). The current was normalized by the Pd or metal mass (Au+Pd) that are obtained from the time-current curves via integration and using the Faraday equation. The electrochemical active surface area (ECSA) was calculated using cyclic voltammetry measurements and the PdO reduction peak (with 424 μC cm^{-2} as the charge density for the reduction of one monolayer of PdO [33]). Chronoamperometric experiments (current vs. time) were also conducted at fixed voltages to probe the long term behavior of the nanostructures.

Computational methods

The ab-initio calculations were performed within density functional theory formalism implemented in Quantum espresso package [34], with generalized gradient approximation (GGA) in the framework of Perdew-Burke-Ernzerhof (PBE) functional [35], and projector augmented wave (PAW) potentials. The plane wave basis cut-off energy was set to 400 eV in our calculations. The structure was relaxed using Broyden–Fletcher–Goldfarb–Shanno optimization method, with a force convergence of 10^{-4} Ry per Bohr, and an energy convergence of 10^{-5} Ry. A k-point samplings of 5 × 5 × 1 were used for the structure relaxation, while denser meshes of 10 × 10 × 4 were used for the CO adsorption calculations. For high accuracy, the energy convergence of 10^{-8} Ry was chosen. The structures were modulated by pure Pd, Au/Pd and 1:1 random mixture of Pd and Au of (2 × 2) unit cell. Au:Pd and a bilayer Au/Pd with a sharp interface between Au and Pd are intended to simulate the interface between Au and Pd in the experimental study. Since CO is a key poisoning species, CO adsorption energy on the participating metal atoms was also calculated considering different adsorption sites based on the usual definition $E_{ads} = E(CO - Metal) - E(CO) - E(Metal)$.

Results and discussion

The deposited layered structures are listed in Table 1, together with the corresponding Pd and Au mass obtained by integrating the current-time curves and using the Faraday equation. It can be seen that two types of layered structures are investigated: Au/Pd/Au with variable Pd-layer thickness and Au/Pd structures. The latter were processed with the purpose of gaining insight into interfacial effects between Au and Pd.

Table 1 – The deposited layered structures with their calculated ECSA and Pd, Au and total mass. In all the structures the diameter was 100 nm.

Structure		Pd mass (mg)	Au mass (mg)	NRs mass (mg)	ECSA (cm^2/mg_{Pd})
Pd	350 nm	0.419	0.000	0.419	39.9
Au/Pd/Au	100/150/100 nm	0.312	0.401	0.713	54.7
Au/Pd/Au	100/65/100 nm	0.158	0.385	0.543	66.6
Au/Pd/Au	100/30/100 nm	0.067	0.475	0.542	94.8
Au/Pd/Au	100/15/100 nm	0.025	0.391	0.416	125.4
Au/Pd	110/65 nm	0.162	0.251	0.413	63.8
Au/Pd	100/30 nm	0.053	0.219	0.272	83.7
Au/Pd	100/15 nm	0.029	0.197	0.226	115.1

Microstructure

Scanning electron microscopy (SEM) micrographs of the NR structures depicted in Table 1 are displayed in Fig. 1 (see also the on-line supporting information for EDS mapping, Fig. S1).

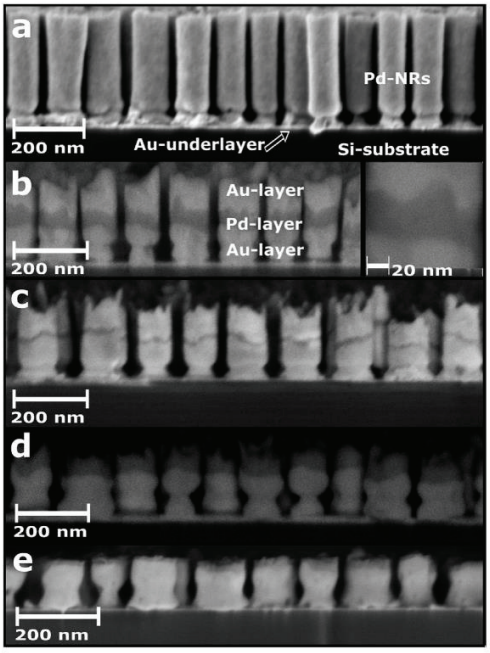

Fig. 1 – ESB micrographs (atomic number contrast at high resolution) of Pd, Au/Pd/Au and Au/Pd NRs with varying Pd layer thickness. From top to bottom: a) Pd-NRs, b) Au/Pd/Au 100/30/100 nm; c) Au/Pd/Au 100/15/100 nm; d) Au/Pd 100/30 nm; e) Au/Pd 100/15 nm.

It is interesting to notice the corrugated morphology of the interface between the two metals that is conspicuous in all the high resolution ESB micrographs. This morphology is probably contingent on the underlying NR morphology that presents an irregular shape as can be inferred from the morphology of both the Au and Pd end caps, but might also suggest dissolution-substitution processes at the interface during electrodeposition of the first layers. The XRD patterns shown in Fig. 2 are, however, conclusive about the formation of the two pure metals with rather a polycrystalline structure. The reflections of Au and Pd were assigned according to references [36,37], respectively. Calculation of peak area ratio of the 200/111 reflections listed in Table 2 for the different structures shows similar values lest for the monolithic Pd NR structure that exhibits a higher value.

Electrochemical behavior

CV behavior

The electrochemical behavior of the Au/Pd/Au layered structures is compared to that of Pd-NRs in Fig. 3. The CV curves are shown for the 10th cycle, but little difference as to the peak positions in comparison to the 1st cycle (on-line supporting information Fig. S2) is observed, apart from a slight increase in the peak intensity upon cycling that could be ascribed to the activation of the Pd-surface, e.g. via the application of potential.

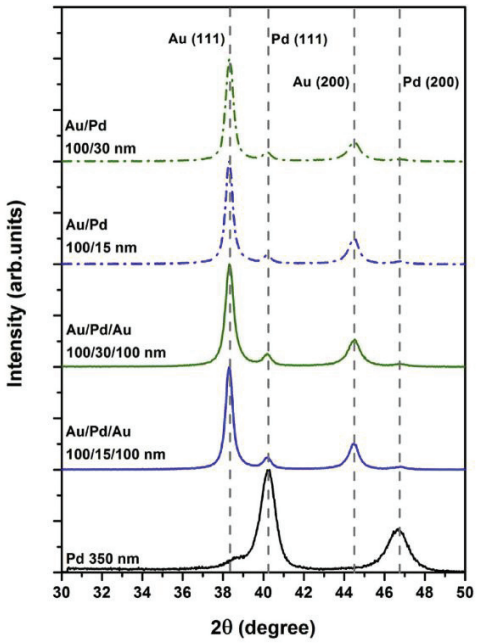

Fig. 2 – XRD patterns in the grazing incidence mode showing the (111) and (200) reflections of Au and Pd in the different layered structures.

Table 2 – The ratio of the Pd 200/111 peak area for the different nanostructures.

Pd 350 nm	0.46
Au/Pd/Au 100/150/100 nm	0.36
Au/Pd/Au 100/65/100 nm	0.34
Au/Pd/Au 100/30/100 nm	0.33
Au/Pd/Au 100/15/100 nm	0.33
Au/Pd 110/65 nm	0.34
Au/Pd 100/30 nm	0.34
Au/Pd 100/15 nm	0.32

Fig. 3 displays the CV curves of the different structures on backward sweep from 1.6 V. First, the Au-oxide reduction peak at approximately 1.2 V (on-line supporting information Fig. S3 for monolithic Au-NRs) is observed followed by the main PdO reduction peak, the position of which is between 0.63 V (Pd-NRs) and 0.68 V (Au/Pd: 110/65 nm), and appears to depend on the specific nanostructure and Pd-layer thickness. A weak peak at more positive voltages can also be seen with its peak position also being dependent on the specific nanostructure. Considering that with thinner Pd-layers the Pd/Au interfacial contribution is more important than in thicker Pd layers, it is straightforward to infer that the Pd atoms behave differently depending on whether they are at the interface with Au or in the Pd “bulk”. The peak at the more positive voltage might reflect PdO reduction of the Pd atoms that are neighboring the Au-atoms or building Pd-rich alloys with them at the interface. For thinner Pd layers, the main PdO reduction peak is displaced to more positive voltage values (towards the Au-oxide reduction peak) which probably indicates that the Pd atoms have more Au atoms as neighbors. The additional reduction hump at still higher voltages might be assigned either to the reduction of Pd atoms in a gold-rich alloy or to that of Au-oxide of the Au atoms neighboring Pd atoms. In all cases these results suggest that diffusion phenomena take place at the Pd/Au interface, and are to some extent in agreement with previous findings [38]. Although the XRD results are conclusive about the formation of separate Au and Pd layers, they nonetheless do not necessarily exclude the formation of thin alloy layers at the interface that cannot be detected with XRD because of the known detection limit of the method. Indeed, earlier investigations of Pd layers on Au suggest the formation of AuPd alloys at the interface at room temperature due to the high diffusion coefficient of Pd in Au [39]. As we should see later, the behavior above may be rationalized taking into account electronic effects arising from the interaction between Au and Pd at the interface.

To summarize this section, it can be stated that when the Pd-thickness is below 100 nm, the voltage of the PdO reduction peak shifts to higher values, with the appearance of an extra but weak peak towards the AuOx reduction peak. A rational explanation of this behavior is to suppose a different chemical environment of the Pd-atoms at the interface, eventually near interface alloys that affect the electrochemical behavior the more the thinner the Pd layers are.

The ECSA shown in Table 1 demonstrates that the layered structures possess a higher active area than bare Pd which is amenable to interfacial effects. In comparison with previously published data, the ECSA values reported for Au@Pd core-shell

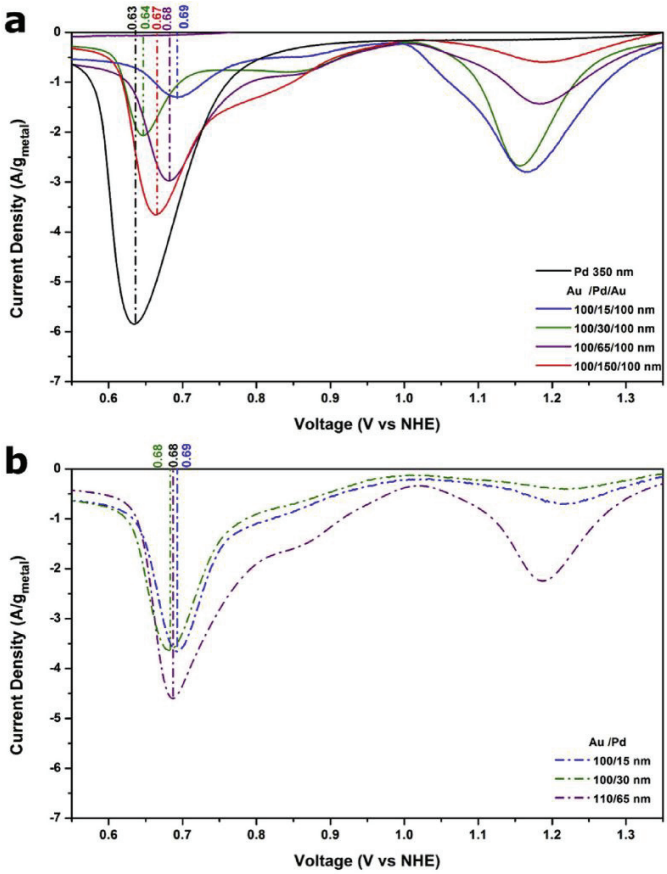

Fig. 3 – Cyclic voltammetry curves in 0.5 M H_2SO_4 for the different structures investigated: the backward sweep with the reduction peaks of AuOx and PdO and their positions is shown. Scan rate: 50 mV s^{-1}.

nanostructures were 1.4 m^2/g_{Pd} and 0.06 m^2/g_{Pd} for Au@Pd core-shell nanodendrites and nanocubes, respectively [27], which are smaller than our results. Dar et al. [40] reported 55.8 cm^2/mg for Pd-nanotubes (NTs) which is higher than that of the Pd-NRs, but the difference resides in the fact that the inner and outer surface in the NTs are active. Fig. 4 shows the ECSA/Geometric lateral area ratio *vs.* Pd-layer thickness. We estimated the geometric surface, using the lateral surface for one NR (diameter 100 nm), then we multiplied it by the estimated total number of NRs. The Pd-NRs show that 12% of the geometric area is active, whereas this value is increased to 43% for Au/15Pd/Au NRs.

Electrocatalytic behavior

The electrocatalytic behavior of the pure Pd-NRs is displayed in Fig. 5(a). It shows a monotonous increase in activity, starting from approximately 0.1 V, peaks at 0.96 V (peak current density: 61 A/g), before it is abruptly suppressed at 1.0 V. On backward sweep, the activity steeply increases at 0.8 V, leading to a sharp maximum that is smaller than the forward peak and a substantial hysteresis in the voltage range between 1 and 0.8 V. In the following decrease in activity, the curve almost overlaps with the forward sweep. This behavior is similar to what is known for Pd-based electrodes and is characteristic for the direct path [21,41]. The activity suppression at voltages higher than the peak voltage has been attributed to the adsorption of site blocking OH species [21] or the reduction of CO_2 (generated from the direct path) to CO [42]. That the adsorption of oxygen-containing species is responsible for catalyst deactivation may be inferred from the backward sweep, where reactivation abruptly starts when the reduction of PdO is initiated, and the maximum occurs at almost exactly the same voltage of the reduction peak, see Fig. 3.

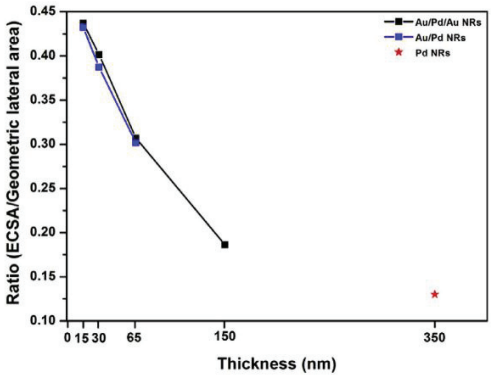

Fig. 4 – The ratio of the electrochemical active surface area, ECSA to the geometric lateral area for the different structures as a function of the Pd layer thickness.

The electrocatalytic behavior of the Au/Pd/Au layered structures, also displayed in Fig. 5, largely depends on the thickness of the Pd-layer, but overall the electrocatalytic activity is enhanced (see also Table 3). This can be first explained by the higher ECSA values of the layered structures. For the smallest Pd thickness (15 nm), Fig. 5(b), the activity starts at small voltages below 0.1 V with a first peak close to 0.2 V, probably denoting activation via hydrogen desorption. The activity slightly decreases before it starts to increase again and peaks at 0.53 V with a peak current density of 334 A/$g_{Pd,}$ before it starts decreasing with, however, a slightly higher slope than in the forward regime. The electrocatalytic activity spans a voltage range from approximately 0.1 V–0.9 V. In the backward sweep the activity starts steeply at 0.82 V, describing a somewhat broad hysteresis at the beginning and peaks at the same voltage of forward sweep with, however, a slightly lower peak current density value. Further decreasing the voltage results in a descending curve that overlaps with the ascending one, lest for the first peak observed on forward sweep. When the Pd thickness is increased to 65 nm, Fig. 5(b), the peak values

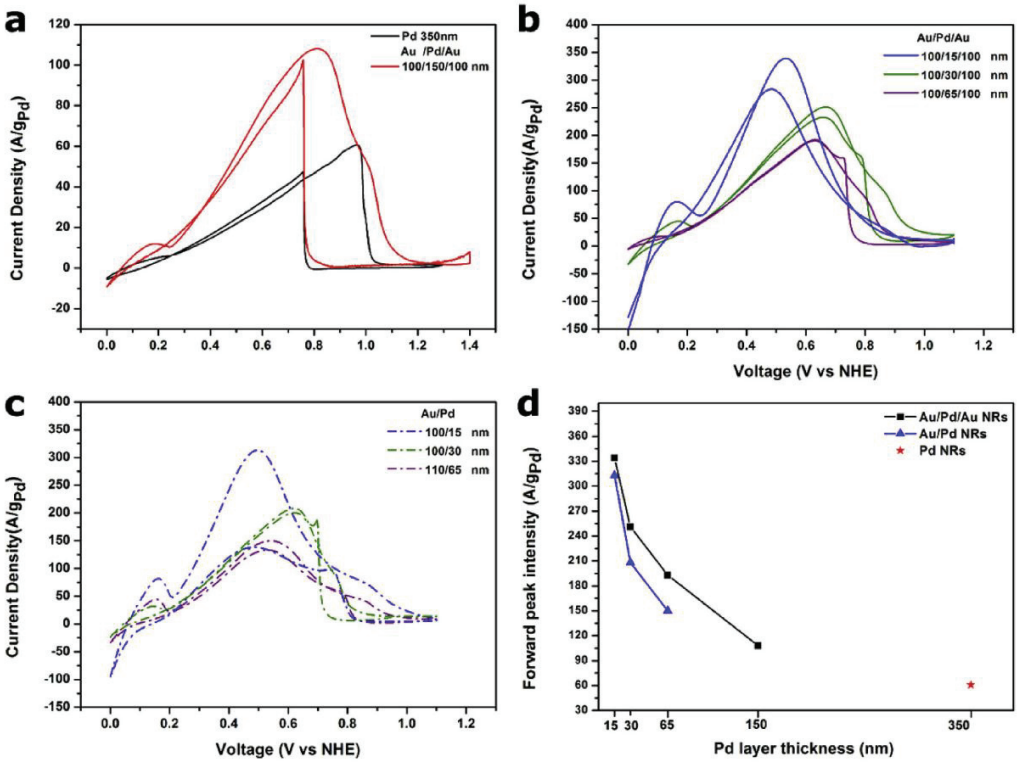

Fig. 5 – Current density (current normalized by the Pd-mass) vs. voltage of the sample electrodes in formic acid; (d) shows the forward peak current density as function of the Pd layer thickness. Scan rate: 50 mV s^{-1}.

Table 3 – Characteristic values derived from Fig. 5 for the electro-catalytic oxidation of formic acid in acidic solution (0.5 M H2SO4+0.5 M HCOOH).

	Forward peak Current Density in A/g_{Pd}	Backward peak Current Density in A/g_{Pd}
Pd 350 nm	61 (at 0.96 V vs NHE)	47.5 (at 0.75 V vs NHE)
100/150/100 nm	108 (at 0.81 V vs NHE)	103 (at 0.76 V vs NHE)
100/65/100 nm	193 (at 0.63 V vs NHE)	190 (at 0.61 V vs NHE)
100/30/100 nm	251 (at 0.66 V vs NHE)	233 (at 0.64 V vs NHE)
100/15/100 nm	334 (at 0.53 V vs NHE)	283 (at 0.48 V vs NHE)
Au/Pd 110/65 nm	150 (at 0.54 V vs NHE)	133 (at 0.52 V vs NHE)
Au/Pd 100/30 nm	208 (at 0.61 V vs NHE)	200 (at 0.62 V vs NHE)
Au/Pd 100/15 nm	313 (at 0.50 V vs NHE)	139 (at 0.48 V vs NHE)

decrease to approximately half the values of the previous structure (see Table 3), but there is little change as to the overall behavior, except for a shallower hysteresis. These results suggest that the Au/Pd interfaces play a major role in the electrocatalytic activity of Pd, resulting in improved behavior in terms of hysteresis, activity range and peak voltages, despite the fact that not all the Pd–sites are available. This is impressively demonstrated by the electrocatalytic behavior of the bilayer Au/Pd (100/15 nm, 100/30 nm and 110/65 nm) structures that are characterized by a lower peak activity than the corresponding Au/Pd/Au structure (Fig. 5(c)). This implies that the chemical interactions between the Pd and Au atoms at the interface control the electrocatalytic activity and may be rationalized in terms of changes in the electronic environment of those atoms. We contrast our results with those reported in previous work on Pd thin layers on polycrystalline Au substrates [42] and strained Pd nanoshells on Au core structures [17]. Thin Pd layers ranging from 1 monolayer (ML) to 17 ML are reported with increasingly higher activity up to 4 ML, before decreasing to slightly lower peak values (10–17 ML) [42]. But the overall behavior, e.g. hysteretic behavior and peak positions are very similar to those observed in the present work which is a further support of the higher activity of interfacial Pd atoms. That in their case the 1 ML Pd sample performed less than thicker films might be rationalized in terms of insufficient Pd surface sites because of the well-known high diffusion rate of Pd in Au (see above). Their work also suggests that a critical Pd layer thickness is necessary in order to boost the electrocatalytic activity of the layer system. This probably allows more surface sites to be occupied by Pd atoms while ensuring a long enough interaction range between them and the underlying Au atoms. Such an assumption is corroborated by DFT calculations (see supplementary information). In contrast, our results largely differ from those reported for strained Pd shell on Au core nanostructures [17]. Their results rather suggest a behavior that is more Pt than Pd like, particularly for their unstrained structures (CS3 to CS10 and Pd-NPs). They, however, show that the current density of FA oxidation increases with increasing Pd mass ratio in the nanostructure, which is in line with the critical Pd thickness mentioned above. Returning back to our results, we observe that further increase in the Pd-layer thickness (150 nm) drastically changes the electrocatalytic behavior towards that of monolithic Pd-NRs, compare Fig. 5(a) and (b). We also notice that the activity curve is shifted to higher voltages (see Table 3), but overall the activity is increased over that of the monolithic structure with peak values that increase with decreasing Pd-layer thickness.

As already mentioned above, the present results show that the interfacial Pd-atoms largely impact the electrocatalytic behavior of the layered structures. These atoms prove to have a higher activity as can be inferred when we compare the specific activity of the layered structures to that of the monolithic Pd-NRs. However, we also notice that when bulk Pd-atoms predominate as in the thicker Pd-layers, the electrocatalytic behavior tends to be more like that of Pd. In all cases the direct path, i.e. the dehydrogenation path, characteristic of Pd, operates for the electrooxidation of FA. But differences are to be outlined: activity suppression is progressive in the case of the thin Pd-layers (15, 30 and 65 nm), denoting a progressive site blocking with either so-called spectator species [21], or CO that is claimed to arise from the reduction of CO_2 (from the direct path) [42]. In contrast, for the thicker layers there is a sharp drop in activity with its complete suppression at approximately 1–1.1 V. We may infer from these results that the dynamics of FA electrooxidation are very much dependent on the electronic environment of the Pd atoms, particularly those with Au neighbors that are thought to form a near interface/surface alloy. DFT calculations published recently predict that such near surface alloys might show improved activity for CO_2 reduction and FA electrooxidation [43].

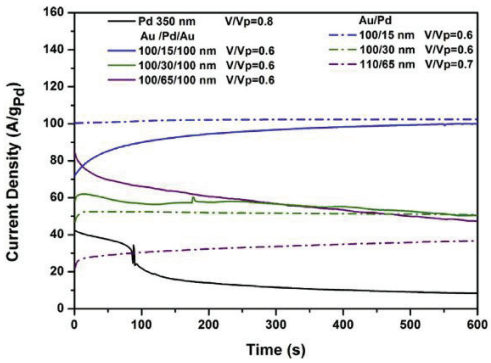

Fig. 6 – Chronoamperograms with current densities (current normalized by the Pd mass) vs. time in 0.5 M H_2SO_4 + 0.5 M HCOOH at specificvoltage ratios, V/Vp, where Vp is the forward peak voltage of the structure considered.

Considering the chronoamperometric results at fixed voltages below the peak maximum of the structure (see Figs. 5), Fig. 6, it can be seen that all the structures with thinner Pd layers exhibit a slower decrease in the activity than thicker Pd layers and monolithic Pd-NRs. For the thinnest Pd-layers of 15 and 30 nm and the bilayer structure, the activity remains constant with time. Because the contribution of the interface in these structures is higher than that of the thicker Pd layers, the neighboring Au atoms must play a key role in preventing activity suppression of the catalyst, e.g. via promoting the oxidation of poisoning species. DFT calculation used to rationalize our results, using 1Au:1Pd alloy to model the interfacial Pd atoms, show that the higher electrocatalytic performance of the NRs is not controlled by the adsorption of CO since the adsorption energy is more stable in AuPd than Pd, but rather by the impact of Au atoms in the oxidation of adsorbed CO [44] (a detailed description of the DFT results can be found in on-line supporting information).

Conclusions

Supported layered Au/Pd/Au and Au/Pd NRs with different Pd layer thicknesse were processed using sequential electrodeposition in an AAO template film on Si. The electrochemical behavior of these nanostructures and their performance for the electrooxidation of FA in an acidic solution is investigated in comparison to monolithic Pd NRs. The results show the formation of distinctive polycrystalline Pd and Au structures with no preferential orientation. A corrugated Au/Pd interface morphology is observed, regardless of Pd layer thickness. The CV behavior very much depends on the Pd layer thickness. Particularly, the PdO reduction peak voltage is displaced to more noble voltages as the Pd layer thickness decreases. The electrocatalytic behavior also depends very much on the Pd layer thickness and the specific nanostructure (Au/Pd/Au or Au/Pd) with increasing performance as the Pd layer thickness decreases. In all cases the electrooxidation performance of FA is higher than that of monolithic Pd NRs and follows the direct path. Further, the performance of Au/Pd/Au was found to be higher than that of Au/Pd bi-layer structures, stressing the impact of the Au/Pd interface on the catalyst properties. As the Pd layer thickness becomes very small, e.g. 15 nm, the electrocatalytic performance drastically increases, but also the long term behavior is improved. These results are interpreted in terms of chemical interaction between Pd and Au at the interface.

Acknowledgments

This research did not receive any specific grant from funding agencies in the public, commercial, or not-for-profit sectors.

Appendix A. Supplementary data

Supplementary data related to this article can be found at https://doi.org/10.1016/j.ijhydene.2019.04.105.

REFERENCES

[1] Chakraborty I, Pradeep T. Atomically precise clusters of noble metals: emerging link between atoms and nanoparticles. Chem Rev 2017;117:8208–71. https://doi.org/10.1021/acs.chemrev.6b00769.
[2] Freyschlag CG, Madix RJ. Precious metal magic: catalytic wizardry. Mater Today 2011;14:134–42. https://doi.org/10.1016/S1369-7021(11)70085-2.
[3] Hegde MS, Madras G, Patil KC. Noble metal ionic catalysts. Acc Chem Res 2009;42:704–12. https://doi.org/10.1021/ar800209s.
[4] Pérez-Rodríguez S, Barreras F, Pastor E, Lázaro MJ. Electrochemical reactors for CO2 reduction: from acid media to gas phase. Int J Hydrogen Energy 2016;41:19756–65. https://doi.org/10.1016/j.ijhydene.2016.06.130.
[5] Kosaka M, Kuroshima S, Kobayashi K, Sekino S, Ichihashi T, Nakamura S, Yoshitake T, Kubo Y. Single-wall carbon nanohorns supporting Pt catalyst in direct methanol fuel cells. J Phys Chem C 2009;113:8660–7. https://doi.org/10.1021/jp8105293.
[6] Feng Y, Song G, Zhang Q, Hu H, Feng M, Wang J, Kong D. Catalytic performance of non-alloyed bimetallic PtAu electrocatalysts for methanol oxidation reaction. Int J Hydrogen Energy 2017;42:30109–18. https://doi.org/10.1016/j.ijhydene.2017.10.102.
[7] Greeley J, Stephens IEL, Bondarenko AS, Johansson TP, Hansen HA, Jaramillo TF, Rossmeisl J, Chorkendorff I, Nørskov JK. Alloys of Platinum and early transition metals as oxygen reduction electrocatalysts. Nat Chem 2009;1:552–6. https://doi.org/10.1038/NCHEM.367.
[8] Nørskov JK, Bligaard T, Rossmeisl J, Christensen CH. Towards the computational design of solid catalysts. Nat Chem 2009;1:37–46. https://doi.org/10.1038/nchem.121.
[9] Stephens IEL, Bondarenko AS, Grønbjerg U, Rossmeisl J, Chorkendorff I. Understanding the electrocatalysis of oxygen reduction on platinum and its alloys. Energy Environ Sci 2012;5:6744–62. https://doi.org/10.1039/C2EE03590A.
[10] Sneed BT, Young AP, Jalalpoor D, Golden MC, Mao S, Jiang Y, Wang Y, Tsung CK. Shaped Pd–Ni–Pt core-sandwich-shell nanoparticles: influence of Ni sandwich layers on catalytic electrooxidations. ACS Nano 2014;8:7239–50. https://doi.org/10.1021/nn502259g.
[11] Godínez-Salomón F, Hallen-López M, Solorza-Feria O. Enhanced electroactivity for the oxygen reduction on Ni@Pt core-shell nanocatalysts. Int J Hydrogen Energy 2012;37:14902–10. https://doi.org/10.1016/j.ijhydene.2012.01.157.
[12] Duan D, Liu S, Yang C, Zhang Z, Hao X, Wei G, Li Y. Electrocatalytic performance of Nicore@Ptshell/C core–shell nanoparticle with the Pt in nanoshell. Int J Hydrogen Energy 2013;38:14261–8. https://doi.org/10.1016/j.ijhydene.2013.08.132.
[13] Almana N, Phivilay SP, Laveille P, Hedhili MN, Fornasiero P, Takanabe K, Basset JM. Design of a core–shell Pt–SiO_2 catalyst in a reverse microemulsion system: distinctive kinetics on CO oxidation at low temperature. J Catal 2016;340:368–75. https://doi.org/10.1016/j.jcat.2016.06.002.
[14] Strickler AL, Jackson A, Jaramillo TF. Active and stable Ir@Pt core–shell catalysts for electrochemical oxygen reduction. ACS Energy Lett 2017;2:244–9. https://doi.org/10.1021/acsenergylett.6b00585.
[15] Kim DY, Han SB, Lee YW, Park KW. Core–Shell nanostructure supported Pt catalyst with improved electrocatalytic stability in oxygen reduction reaction. Mater Chem Phys 2013;137:704–8. https://doi.org/10.1016/j.matchemphys.2012.11.006.

[16] Hsu C, Huang C, Hao Y, Liu F. Electro-oxidation of formate-based solutions on Au/Pd core–shell nanoparticles – experiment and simulation. Int J Hydrogen Energy 2013;38:15532–41. https://doi.org/10.1016/j.ijhydene.2013.09.019.

[17] Montes de Oca MG, Plana D, Celorrio V, Lazaro MJ, Fermín DJ. Electrocatalytic properties of strained Pd nanoshells at Au nanostructures: CO and HCOOH oxidation. J Phys Chem C 2012;116:692–9. https://doi.org/10.1021/jp208998j.

[18] Silva TAG, Teixeira-Neto E, López N, Rossi LM. Volcano-like behavior of Au-Pd core-shell nanoparticles in the selective oxidation of alcohols. Sci Rep 2014;4:5766. https://doi.org/10.1038/srep05766.

[19] Hsu C, Huang C, Hao Y, Liu F. Au/Pd Core–Shell nanoparticles for enhanced electrocatalytic activity and durability. Electrochem Commun 2012;23:133–6. https://doi.org/10.1016/j.elecom.2012.07.027.

[20] Lu CL, Prasad KS, Wu HL, Ho JA, Huang MH. Au Nanocube-directed fabrication of Au-Pd core-shell nanocrystals with tetrahexahedral, concave octahedral, and octahedral structures and their electrocatalytic activity. J Am Chem Soc 2010;132:14546–53. https://doi.org/10.1021/ja105401p.

[21] Arenz M, Stamenkovic V, Schmidt TJ, Wandelt K, Ross PN, Markovic NM. The Electro-oxidation of formic acid on Pt–Pd single crystal bimetallic surfaces. Phys Chem Chem Phys 2003;5:4242–51. https://doi.org/10.1039/B306307K.

[22] Jiang K, Zhang HX, Zou S, Cai WB. Electrocatalysis of formic acid on palladium and platinum surfaces: from fundamental mechanisms to fuel cell applications. Phys Chem Chem Phys 2014;16:20360–76. https://doi.org/10.1039/C4CP03151B.

[23] Zhang LJ, Wang ZY, Xia DG. Bimetallic PtPb for formic acid electro-oxidation. J Alloy Comp 2006;426:268–71. https://doi.org/10.1016/j.jallcom.2005.12.114.

[24] Pandey RK, Lakshminarayanan V. Electro-Oxidation of formic acid, methanol, and ethanol on electrodeposited pd-polyaniline nanofiber films in acidic and alkaline medium. J Phys Chem C 2009;113:21596–603. https://doi.org/10.1021/jp908239m.

[25] Fleischmann CW, Johnson GK, Kuhn AT. The Electrochemical oxidation of formic acid on platinum. J Electrochem Soc 1964;111:602–5. https://doi.org/10.1149/1.2426191.

[26] Metin Ö, Ho SF, Alp C, Can H, Mankin MN, Gültekin MS, Chi M, Sun S. Ni/Pd Core/Shell nanoparticles supported on graphene as a highly active and reusable catalyst for suzuki-miyaura cross-coupling reaction. Nano Res 2013;6:10–8. https://doi.org/10.1007/s12274-012-0276-4.

[27] Wang H, Sun Z, Yang Y, Su D. The growth and enhanced catalytic performance of Au@Pd core–shell nanodendrites. Nanoscale 2013;5:139–42. https://doi.org/10.1039/C2NR32849F.

[28] Kang Y, Qi L, Li M, Diaz RE, Su D, Adzic RR, Stach E, Li J, Murray CB. Highly active Pt_3Pb and core–shell Pt_3Pb–Pt electrocatalysts for formic acid oxidation. ACS Nano 2012;6:2818–25. https://doi.org/10.1021/nn3003373.

[29] Lu X, Zheng L, Zhang M, Tang H, Li X, Liao S. Synthesis of core-shell structured Ru@Pd/C catalysts for the electrooxidation of formic acid. Electrochim Acta 2017;238:194–201. https://doi.org/10.1016/j.electacta.2017.03.115.

[30] Choi JH, Jeong KJ, Dong Y, Han J, Lim TH, Lee JS, Sung YE. Electro-oxidation of methanol and formic acid on PtRu and PtAu for direct liquid fuel cells. J Power Sources 2006;163:71–5. https://doi.org/10.1016/j.jpowsour.2006.02.072.

[31] Eley DD, Luetic P. The Formic acid decomposition on palladium-gold alloys. Trans Faraday Soc 1957;53:1483–7. https://doi.org/10.1039/TF9575301483.

[32] Es-Souni M, Habouti S. Ordered nanomaterial thin films via supported anodized alumina templates. Front Mater 2014;1:19. https://doi.org/10.3389/fmats.2014.00019.

[33] Ojani R, Abkar Z, Hasheminejad E, Raoof JB. Rapid fabrication of Cu/Pd nano/micro-particles porous-structured catalyst using hydrogen bubblesd ynamic template and their enhanced catalytic performance for formic acid electrooxidation. Int J Hydrogen Energy 2014;39:7788–97. https://doi.org/10.1016/j.ijhydene.2014.03.081.

[34] Giannozzi P, Baroni S, Bonini N, Calandra M, Car R, Cavazzoni C, Ceresoli D, Chiarotti GL, Cococcioni M, Dabo I, Dal Corso A, De Gironcoli S, Fabris S, Fratesi G, Gebauer R, Gerstmann U, Gougoussis C, Kokalj A, Lazzeri M, Martin-Samos L, Marzari N, Mauri F, Mazzarello R, Paolini S, Pasquarello A, Paulatto L, Sbraccia C, Scandolo S, Sclauzero G, Seitsonen AP, Smogunov A, Umari P, Wentzcovitch RM. QUANTUM ESPRESSO: a modular and open-source software project for quantum simulations of materials. J Phys Condens Matter 2009;21:395502. https://doi.org/10.1088/0953-8984/21/39/395502.

[35] Perdew JP, Burke K, Ernzerhof M. Generalized gradient approximation made simple. Phys Rev Lett 1996;77:3865–8. https://doi.org/10.1103/PhysRevLett.77.3865.

[36] Straumanis ME. Neubestimmung der Gitterparameter, Dichten und thermischen Ausdehnungskoeffizienten von Silber und Gold, und Vollkommenheit der Struktur. Monatsh Chem 1971;102:1377–86. https://doi.org/10.1007/BF00917194.

[37] King HW, Manchester FD. A low-temperature X-ray diffraction study of Pd and some Pd-H alloys. J Phys F Met Phys 1978;8:15–26. https://doi.org/10.1088/0305-4608/8/1/007.

[38] Lukaszewski M, Czerwinski A. Electrochemical behavior of palladium–gold alloys. Electrochim Acta 2003;48:2435–45. https://doi.org/10.1016/S0013-4686(03)00270-6.

[39] Gossner K, Mizera E. Alloy formation at the deposition of palladium on gold at room temperature. J Electroanal Chem Interfacial Electrochem 1981;125:359–66. https://doi.org/10.1016/S0022-0728(81)80354-3.

[40] Dar FI, Habouti S, Minch R, Dietze M, Es-Souni M. Morphology control of 1D noble metal nano/heterostructures towards multi-functionality. J Mater Chem 2012;22:8671–9. https://doi.org/10.1039/C2JM16826J.

[41] Hoshi N, Kida K, Nakamura M, Nakada M, Osada K. Structural effects of electrochemical oxidation of formic acid on single crystal electrodes of palladium. J Phys Chem B 2006;110:12480–4. https://doi.org/10.1021/jp0608372.

[42] Obradović MD, Gojković SL. HCOOH Oxidation on thin Pd layers on Au: self-poisoning by the subsequent reaction of the reaction product. Electrochim Acta 2013;88:384–9. https://doi.org/10.1016/j.electacta.2012.10.033.

[43] Zhao Z, Lu G. Computational screening of near-surface alloys for CO_2 electroreduction. ACS Catal 2018;8:3885–94. https://doi.org/10.1021/acscatal.7b03705.

[44] Zeng W, Tang J, Wang P, Pei Y. Density functional theory (DFT) studies of CO oxidation reaction on M_{13} and $Au_{18}M$ clusters (M= Au, Ag, Cu, Pt and Pd): the role of co-adsorbed CO molecule. RSC Adv 2016;6. 55867–55777, https://doi.org/10.1039/C6RA07566E.

Supplementary Materials

Layered Au-Pd-Au Nanorod Catalysts: Pd-layer Thickness Effects on Catalyst Performance

Ayoub Laghrissi[a] and Mohammed Es-Souni[a, *]

[a] IMST Institute for Materials and Surface Technology, University of Applied Sciences Kiel, Kiel, Schleswig-Holstein, Germany

* Corresponding author at: IMST Institute for Materials and Surface Technology, University of Applied Sciences Kiel, Grenzstr. 3, 24149 Kiel, Schleswig-Holstein, Germany.
E-mail address: mohammed.es-souni@fh-kiel.de.

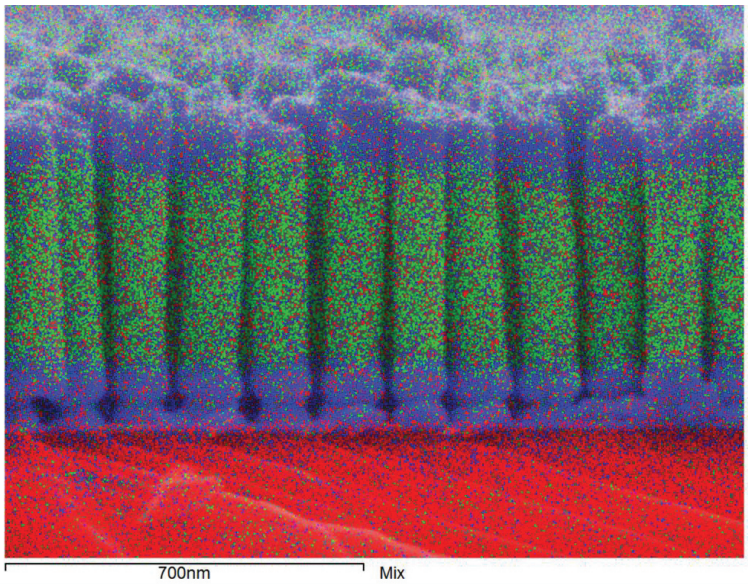

Fig. S1 – EDS mapping showing Pd (Green) and Au (bleu) layers.

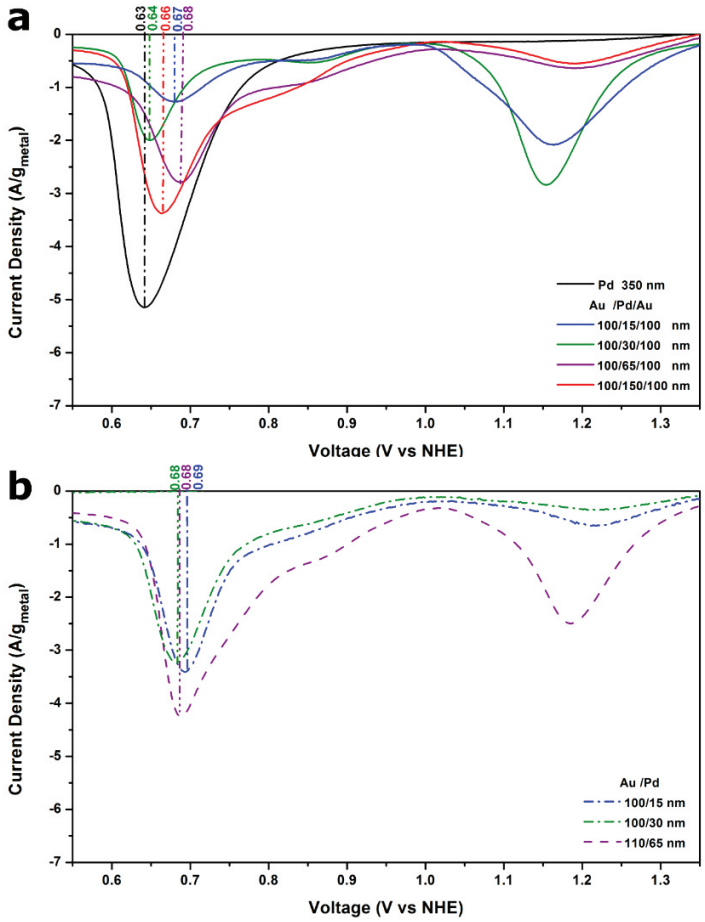

Fig. S2 – 1st Cycle backward sweep curves in 0.5M H_2SO_4 for the different structures. With AuOx and PdO reduction peaks and their positions. Scan rate: 50 mV s^{-1}.

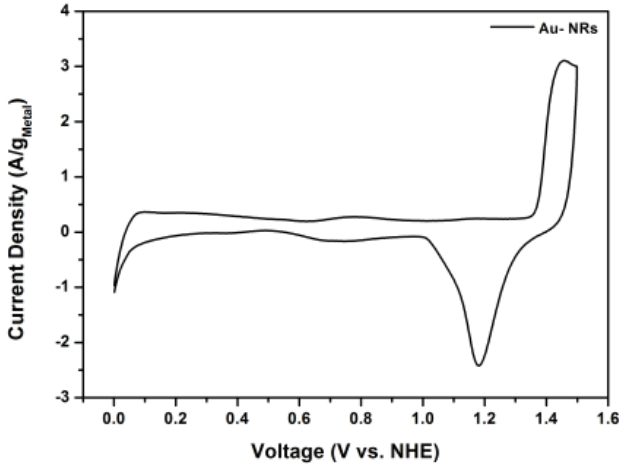

Fig. S1 – Cyclic voltammetry curves in 0.5M H_2SO_4 for Au-NRs

Density Functional Calculations:

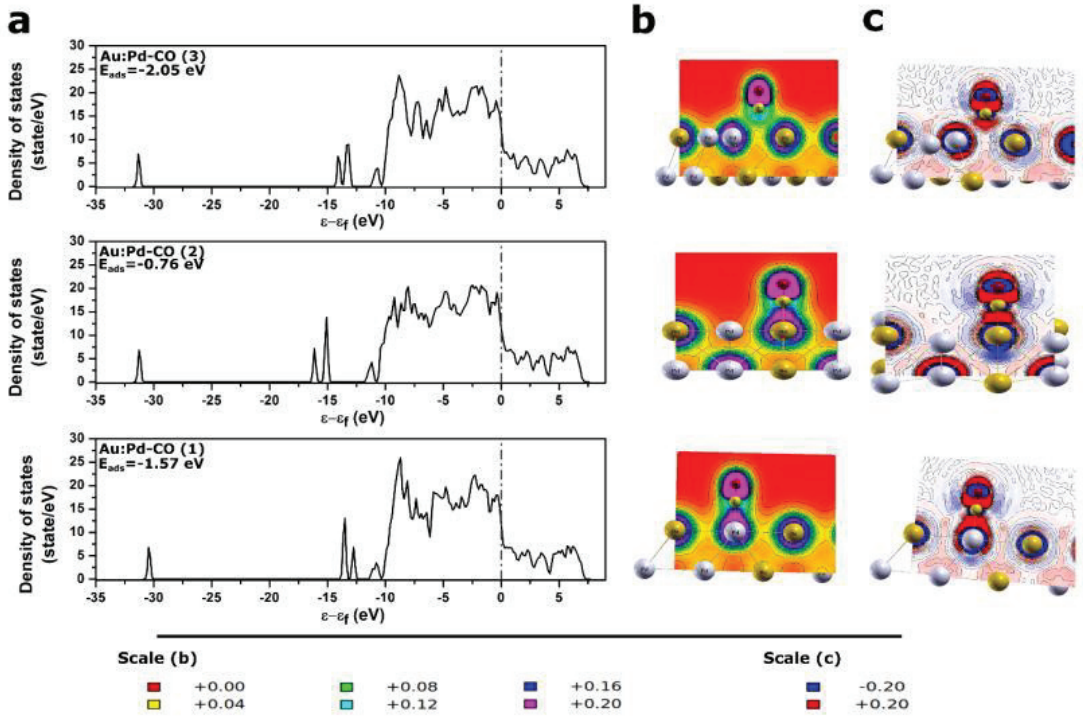

Fig. S4 – (a) Density of state calculations of (2x2x1) slab with a 1:1 Au:Pd mixture with adsorbed CO on different sites, including bridge sites; the corresponding adsorption energies are also shown; (b) the map of the charge density, (c) the difference between charge density of the system and the superposition of the charge density of neutral atoms.

For the sake of rationalizing the results above, and because CO can be considered as the main poisoning adsorbent, we conducted DOS calculations of CO adsorption on different sites of a (2x2x1) slab with a 1:1 Au:Pd random mixture (see also the experimental section). The results show that the bridge sites (CO bridging Pd-Au) are more stable than the top site (E_{ads} = -2.05 eV), Fig. S4. The calculated adsorption energies are slightly more negative than in the case of the Pd slab whereas CO adsorption on Au top site is higher than the value of -0.86eV reported for pure Au [1]. More calculations assuming a bent CO bridge configuration towards the Pd atoms prove to be even more stable (Fig. S5). When CO is adsorbed on top sites (either Au or Pd), e.g. Au:Pd-CO(1) and Au:Pd-CO(2) the charge transfer occurs only with one atom, whereas for the bridge site a charge sharing is taking place with the nearest 2 atoms, Fig. S4b. Also the charge distribution in the space is not intense and not concentrated in one region as in the case of the top site. This is clearly seen by comparing the charge accumulation and charge depletion plots of both sites.

However, the charge density contours pertaining to the bridge site do not mean that CO transfers fewer charges to the metal than in the case of the top site. Rather the transfer is shared with the surrounding atoms (nearest neighbor atoms). Similar results are obtained with a slab containing a Pd layer on top of an Au layer (Fig. S6).

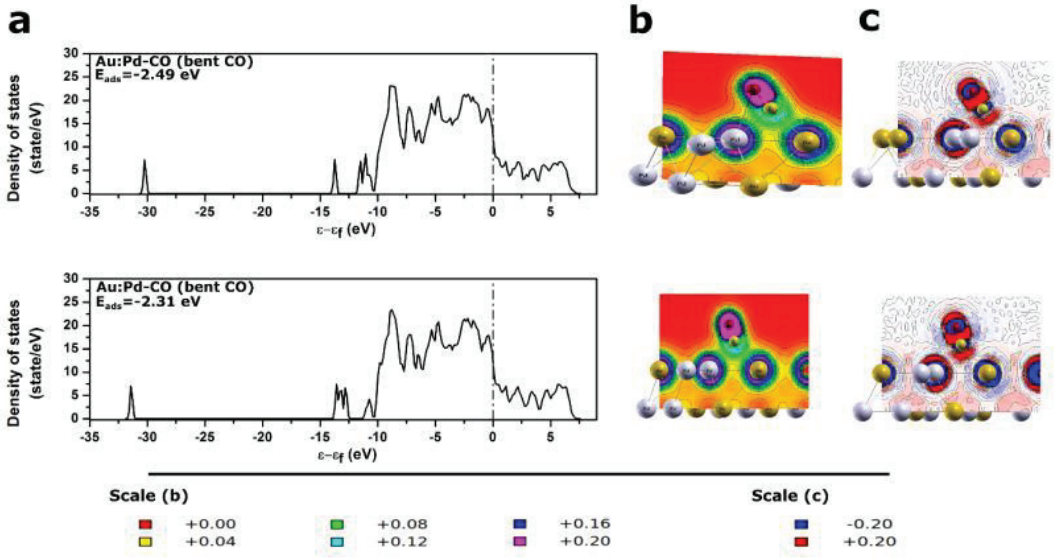

Fig. S5 – (a) Density of state calculations of (2x2x1) slab with a 1:1 Au:Pd mixture with bent CO bridge configuration towards the Pd atom, (b) the charge density, (c) the difference between charge density of the system and the superposition of the charge density of neutral atoms.

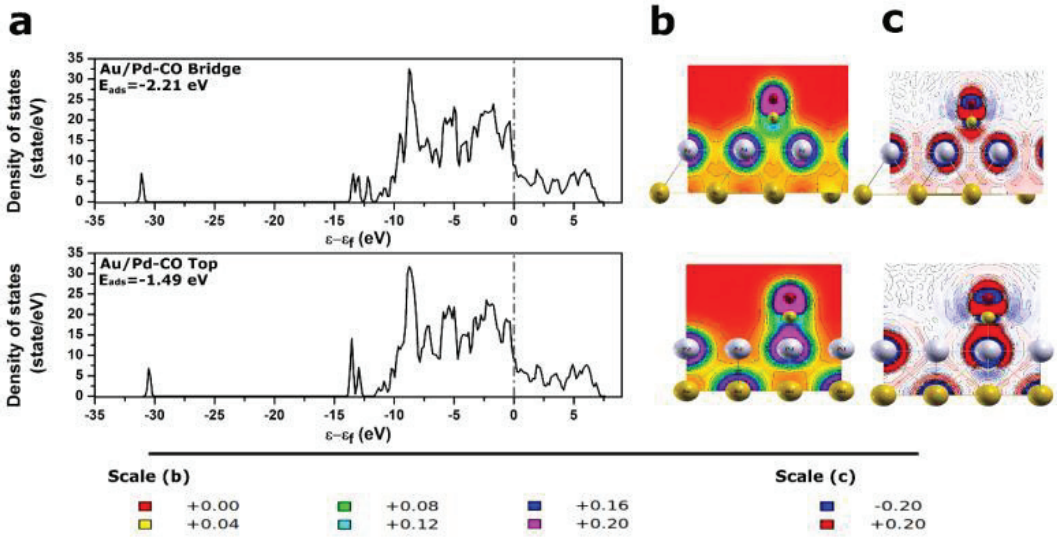

Fig. S6 – (a) Density of state calculations of (2x2x1) slab of a bilayer Au/Pd structure with adsorbed CO, (b) the charge density, (c) the difference between charge density of the system and the superposition of the charge density of neutral atoms.

The calculated adsorption energies suggest that CO adsorption, preferably on bridge sites, is favored for intermixed Au:Pd layers and Au/Pd bilayers over Pure Pd. This behavior can be rationalized taking into account charge transfer from Pd to Au that should increase the ability of Pd to accept charges from C, which in turn increases the CO-Pd interaction, as schematically depicted in Fig. S7. These results, however, also imply that the presence of Au atoms should rather impart a high poisoning rate to the Au-Pd catalysts, which contrasts with the experimental findings described above. This means that other dynamics are governing FA electrooxidation than CO adsorption alone.

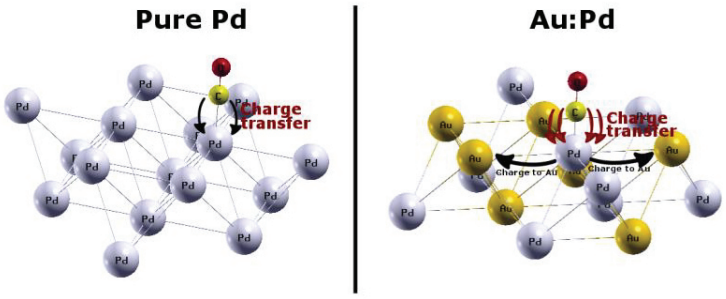

Fig. S7 – A schematic of the charge transfer between CO and metal atoms for pure Pd and mixed Au:Pd.

Previous studies had shown that gold tends to adsorb oxygen species (O, O_2) [2,3], and is a potent catalyst for CO oxidation [3]. The reaction between O_2 and CO is described by the bimolecular Langmuir-Hinshelwood mechanism, Equations 2-5:

$CO + * \rightarrow CO_{ads}$ (3), see also Fig. S8(a)

$O_2 + * \rightarrow O_{2\,ads}$ (4), see also Fig. S8(b-c)

$CO_{ads} + O_{2\,ads} \rightarrow OCOO_{ads} + *$ (5), see also Fig. S8(c)

$OCOO_{ads} \rightarrow CO_2 + O_{ads}$ (6), see also Fig. S8(d)

O_{ads} can also react with another CO molecule to form CO_2. This means that even if Au promotes CO adsorption on the nanostructure, it at the same time plays an important role as an oxidation agent for the adsorbed CO, and reduces the poisoning, in accordance with the experimental results.

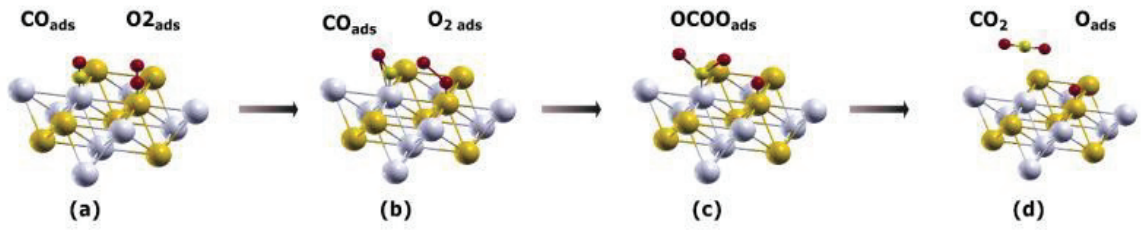

Fig. S8 – A schematic of bimolecular Langmuir-Hinshelwood mechanism in Au:Pd.

R E F E R E N C E S

[1] Gajdoš M, Eichler A, Hafner J, CO Adsorption on close-packed transition and noble metal surfaces: trends from ab initio calculations. J Phys: Condens Matter 2004;16:1141–1164.

[2] Daigle AD, BelBruno JJ, Density functional theory study of the adsorption of oxygen atoms on gold (111), (100) and (211) surfaces. Surf Sci 2011;605:1313–1319. https://doi.org/10.1016/j.susc.2011.04.025

[3] Zeng W., Tang J., Wang P., Pei Y., Density functional theory (DFT) studies of CO oxidation reaction on M_{13} and $Au_{18}M$ Clusters (M= Au, Ag, Cu, Pt and Pd): the role of co-adsorbed co molecule. RSC Adv 2016;6:55867–55777. https://doi.org/10.1039/C6RA07566E

6 “Porous PtPd alloy nanotubes. Towards high performance electrocatalysts with low Pt-loading”

Ayoub Laghrissi, Mohammed Es-Souni
IMST Institute for Materials and Surface Technology, University of Applied Sciences Kiel, Kiel, Schleswig-Holstein, Germany
[DOI: 10.1039/C9CY01145E] Reproduced with permission of The Royal Society of Chemistry

For electrocatalytic applications, the surface area of electrocatalysts is one of the important factors for increasing their activity: Increasing the surface area to the mass unit requires the tuning of the nanostructure shape. Compared to nanorods, tubular nanostructures exhibit a higher area due to the reduction of the bulk matter. The thinner the tubes walls, the lesser the loading of the electrocatalysts. Porosity can considerably increase the surface area of the electrocatalysts. In this paper, nanotubular structures are combined with porous ones, leading to porous nanotubes. Given the importance of the electrocatalyst composition to reduce the loading of expensive noble metals, such porous nanotubes were composed of PtPd alloys. The electrocatalytic performance of porous PtPd for methanol electrooxidation was investigated for several contents of Pt down to 5% Pt: The electrocatalytic performance was dependent on a Pt content with a maximum at 10% (ECSA of 1358 m^2/g_{Metal} and 932 A/g_{Pt}). This activity is even greater than that observed with Pt black, while the Pt content is comparatively low. The underlying mechanisms involve the increase in the surface area by the porous nanotubular structure, followed by preventing the poisoning by intermediate carbonaceous species that preferentially adsorb on Pd protecting the Pt active sites.

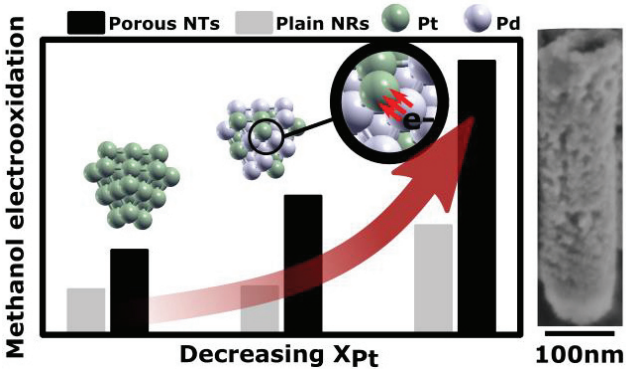

Prof. Dr. Mohammed Es-Souni designed the underlying concept. The author of the dissertation carried out the experiments and evaluated them. The author prepared the first draft and Prof. Dr. Mohammed Es-Souni validated the results and corrected the manuscript.

Catalysis Science & Technology

PAPER

View Article Online
View Journal | View Issue

Cite this: *Catal. Sci. Technol.*, 2019, **9**, 4355

Porous PtPd alloy nanotubes: towards high performance electrocatalysts with low Pt-loading†

Ayoub Laghrissi and Mohammed Es-Souni *

The electrochemical properties of Pt-based 1D electrocatalysts reported so far prove to be superior to those of known 0D nanomaterials. Particularly, the combination of Pt and Pd either as nanoalloys or Pt-coated Pd nanotubes (NTs) demonstrably boosts the catalyst performance. This provided the main impetus for the present work. The porous PtPd-NTs are processed into the nanopores of anodized aluminum oxide (AAO) template films using electrodeposition from an electrolyte containing appropriate concentrations of Pt and Pd ions and a small amount of a non-ionic surfactant. The range of PtPd alloys investigated is from 95 to 0 at% Pd. The deposition conditions allow diffusion-kinetics controlled growth along the AAO nanopore walls. The NTs with a wall thickness of approximately 15 nm exhibit closely-knit nanoparticles that are separated by mesopores. The salient result of this work is the strong dependence of the electrochemical properties on the Pt content with a maximum of 10 at% Pt. Below and beyond this value, both the electrochemical active surface area (ECSA) and the specific electrocatalytic activity towards methanol electrooxidation substantially decrease. The best ECSA values obtained amount to 138 $m^2\ g_{metal}^{-1}$. Even for the 5 at% Pt alloy, the ECSA value obtained is higher than that of Pt-black and pure Pt-NTs. These results are unsurpassed in comparison to similar nanostructures. The catalytic performance for methanol electrooxidation also behaves in the same way with a maximum of 932 A g_{Pt}^{-1} for the 10 at% Pt alloy NTs. Our results show a practical way to boost the catalyst performance while keeping the Pt content low. They are discussed in terms of structure and morphology effects, and rationalized using DFT calculations that show that in a Pd50 : Pt50 mixture, CO preferentially adsorbs on Pd top-sites, due to charge transfer from Pd to Pt, thus keeping the active Pt sites free from intermediate adsorbates.

Received 11th June 2019,
Accepted 13th July 2019

DOI: 10.1039/c9cy01145e

rsc.li/catalysis

1. Introduction

The advantages of 1D over 0D electrocatalysts have been highlighted in various reports,[1–3] because they afford outstanding properties as cathode and anode materials for applications in direct methanol fuel cells (DMFCs).[4] This holds particularly for Pt-based materials that are among the most widely used catalysts in DMFCs. However, the scarcity of Pt and consequently its prohibitively high price is an important cost position that certainly hampers the widespread use of these fuel cells. Therefore, emphasis in research activities has been placed in the last decade on minimizing Pt-loading, particularly *via* alloying Pt with less noble transition metals. The review articles by Lu *et al.*[5] and Koenigsmann *et al.*[3] summarized the research done so far on 1D nanostructures, including 1D nanoalloys. The advantages of 1D over 0D/C Pt catalysts are intimately related to their anisotropic growth which allows exposition of the low index planes (100) and (111) that possess the highest catalytic activity. In terms of Pt-alloy electrocatalysts, major advantages – that also hold for 0D – arise from the often-discussed ligand effect which alters the electronic environment of the active Pt atoms, and makes them less prone to poisoning.[6–9] While alloys of Pt with 3d transition metals (Fe, Ni, and Co) might present cost advantages, their lack of stability in oxidizing chemical environments constitutes a serious impediment to their use.[10–12] For instance, PtCo NWs were processed by Liu *et al.*[13] to take advantage of the preferential dissolution of Co in phosphoric acid and in this way generate porous Pt-NWs. Even though a number of 1D binary and ternary alloys were proposed which purportedly had high performance and stability,[14,15] pure Pt or Pt and Pd based alloys still constitute the catalysts of choice. The outstanding properties of their 1D nanostructures and their resistance to site blocking species are well established.[3,5]

Particularly, PtPd-nanoalloys have seen a flurry of research activities,[16–22] because of their promising potential as catalysts for the oxygen reduction reaction (ORR). Pd is also a precious metal but its cost is about one-third that of Pt.

Institute for Materials & Surface Technology, University of Applied Sciences, Kiel, Germany. E-mail: mohammed.es-souni@fh-kiel.de

† Electronic supplementary information (ESI) available. See DOI: 10.1039/c9cy01145e

Further, Pt and Pd have similar electronic structures and very close atomic radii which result in the formation of solid solutions, particularly in the case of nanoparticles.[23] With respect to their electrocatalytic properties, PtPd nanostructures show a peculiar composition-dependent behaviour. Depending on the catalytic reaction, the highest mass activities were reported for Pt-lean alloy NPs down to 9% Pt for formic acid electrooxidation,[24] 14% for the ORR,[16] and approximately 66% Pt for methanol electrooxidation.[25] As for 0D, the properties of 1D nanostructures are also affected by size, morphology, and chemistry. For instance, Koenigsmann *et al.*[3] demonstrated that Pt NWs with a diameter of a few nanometers are largely superior to Pt-NTs in their ORR activity. Replacing Pt with Pd in PtPd (50 : 50) only moderately decreases the performance while decreasing the material cost. The higher performance of the NWs was ascribed to surface contraction inherent to nanoscale structures and ensuing electronic properties. Further, promoting porosity in catalyst nanostructures is an efficient measure to increase the electrochemical active surface area. Mostly, porous nanostructures were generated *via* galvanic replacement and selective dissolution of a less noble metal in an alloy.[26–29] Porous Pt-NRs were processed by Li *et al.*[30] using electrodeposition in track-etched polycarbonate membranes and a Pt–electrolyte containing a surfactant. Their results show that porosity allows for the increase of the electrochemical active surface area (ECSA) to approximately 46 $m^2\ g_{Pt}^{-1}$. Moderate mass activities for methanol electrooxidation were obtained by them in perchloric acid electrolyte. Moreover, porous Pt-NTs and Pt-coated Pd-NTs were reported using galvanic displacement of Ag and partial displacement of Pd by Pt, respectively,[31] with ECSA values in excess of 100 $m^2\ g^{-1}$ and large mass activities. In the present communication, supported porous Pt and PtPd alloy NTs were fabricated using electrodeposition at a negative voltage, and using a surfactant. It will be shown below that the method yields reproducible results in terms of alloy composition, morphology and pore distribution. As will be discussed later, the nanostructures exhibit a huge ECSA and mass activity that are strongly dependent on the Pt-content of the alloy. A salient result of this work is the mass activity and ECSA peaks observed at 10PtPd (Pd-10 at% Pt). Lower or higher Pt contents lead to smaller values, but even at 5PtPd, both values are substantially higher than those of pure porous Pt-NTs. The critical Pt content of 10 at%, at which an ECSA of 100 $m^2\ g_{metal}^{-1}$ and a specific mass activity of 835 A g_{Pt}^{-1} in sulfuric acid (138 $m^2\ g_{metal}^{-1}$ and 932 A g_{Pt}^{-1} in perchloric acid) are obtained, allows us to propose catalysts with low Pt contents that are expected to substantially decrease catalyst cost. Moreover, our processing method can be applied on a large scale on any catalyst support which should make any further processing steps, *e.g.* suspension, mixing with carbon materials, *etc.*, unnecessary.

2. Experimental

2.1. Synthesis and electrochemical measurements

The following chemicals were used as purchased: methanol, phosphoric acid 88%, oxalic acid dihydrate 99%, and sodium hydroxide (Roth, Germany); sulfuric acid (VWR chemicals, Germany); perchloric acid (Fluka chemicals); H_2PtCl_6 and Brij58 (Sigma-Aldrich, Germany); K_2PdCl_4 (bcr, Germany); carbon monoxide gas (Westfalen A.G, Germany).

Anodized aluminum oxide (AAO) template films supported on silicon were processed following the procedure described in detail in our previous work.[32,33] Briefly, a 500 nm aluminum film is deposited on an Au(6 nm)/Ti(4 nm)/Si(wafer) heterostructure by electron beam evaporation using a PVD device (PVD75, Lesker, USA). Anodization is conducted using a two-electrode set-up in 0.2 M aqueous solution of oxalic acid under potentiostatic conditions of 70 V using an electrochemical workstation (Keithley 2400 SM, Cleveland, OH, USA). A Pt foil was used as a counter electrode. After anodization, barrier layer removal and pore widening are conducted in phosphoric acid (5 wt% in water) for 50 minutes at 30 °C.

The PtPd-NRs and porous PtPd-NTs were grown into the AAO channels of the AAO template film *via* electrodeposition from appropriate volume fractions of 10 mM H_2PtCl_6 and 10 mM K_2PdCl_4 aqueous electrolytes (Table S1†). For porous NTs, 3 wt% of non-ionic surfactant Brij58 was added to the solution. Porous Pt-NTs and porous PtPd-NTs were deposited at −0.5 V. The plain PtPd-NRs were deposited at −0.1 V. Deposition was performed using a three-electrode set-up, with a Au/AAO template working electrode, a Pt counter electrode and an Ag/AgCl reference electrode, under potentiostatic conditions using an electrochemical workstation (Princeton Potentiostat/Galvanostat Model 263A, USA). After electrodeposition, the 1D nanostructures were exposed by dissolving the AAO film in an aqueous solution of NaOH (5 wt%) at room temperature. This step takes up to 30 minutes. Subsequently, the nanostructures were thoroughly washed with distilled water followed by washing several times with ethanol; it should be pointed out that these multiple washing steps are necessary in order to remove residual Brij58, if any.

The microstructure and morphology of the NTs were characterized with a high-resolution scanning electron microscope (SEM Ultra Plus, ZEISS, Germany) operating in the secondary (SE) and energy selective backscattered (ESB) electron modes. The SEM is also equipped with an energy dispersive X-ray spectroscopy (EDS) package (INCAx-act, Oxford Instruments, UK), and a scanning transmission microscopy detector. For the STEM investigations, the nanostructures were carefully scratched from the surface and suspended in water, before “fishing” them with a Cu-TEM grid and mounting on the STEM sample holder. The STEM was operated at 30 kV.

The NT structure was characterized by X-ray diffraction (XRD, X'Pert Pro diffractometer PANalytical, Holland) in grazing incidence diffraction mode with constant θ = 1° using monochromatic CuKα radiation with λ = 1.5418 Å and a scanning range between 30° and 50° (2θ). The device has a full width at half maximum resolution of 0.03°. The interplanar spacing d_{111} was calculated from the 111 peak position ($2\theta_{111}$), after Lorentzian fitting.

An electrochemical workstation (ZAHNER IM6e, Kronach, Germany) was used for cyclic voltammetry (CV) measurements. The electrochemical experiments were performed in 0.5 M H_2SO_4, and 0.1 M $HClO_4$ using a three-electrode set-up with a Pt mesh and HydroFlex (reversible H_2 reference electrode) as counter and reference electrodes, respectively. For methanol electrooxidation, 0.5 M H_2SO_4 + 0.5 M CH_3OH aqueous electrolyte was used. All potentials were referenced to the normal hydrogen electrode (NHE). The current was normalized by the Pt or metal mass (Pt + Pd) that are obtained from the time–current curves *via* integration and using the Faraday equation (Table 1). The electrochemical active surface area (ECSA) was calculated using cyclic voltammetry measurements *via* the integrated charge of the underpotentially deposited hydrogen (H_{upd}) region after double-layer correction (with 210 μC cm^{-2} as the charge density for H_{upd}.[34,35]). The ECSA obtained with the H_{upd} method was compared to that using CO-stripping for the 10PtPd alloy NTs. For this purpose, the 0.5 M H_2SO_4 solution was first saturated with CO (after the usual bubbling with nitrogen). Subsequently CO was adsorbed onto the catalyst at 0.4 V for 10 min, and the CV curve was recorded starting from 0.4 V to prevent hydrogen adsorption. The ECSA was calculated considering that the oxidation of CO involves 2 electrons.

2.2. Computational methods

The *ab initio* calculations were performed within the density functional theory formalism implemented in the Quantum Espresso package,[36] with generalized gradient approximation (GGA) in the framework of the Perdew–Burke–Ernzerhof (PBE) functional[37] and projector augmented wave (PAW) potentials. The plane wave basis cut-off energy was set to 400 eV in our calculations. The structure was relaxed using the Broyden–Fletcher–Goldfarb–Shanno optimization method, with a force convergence of 10^{-4} Ry per Bohr and an energy convergence of 10^{-5} Ry. *k*-Point samplings of 5 × 5 × 1 were used for the structure relaxation, while denser meshes of 10 × 10 × 4 were used for the CO adsorption calculations. For high accuracy, an energy convergence of 10^{-8} Ry was chosen. The structures were modulated by pure Pd, pure Pt, and a 1 : 1 random mixture of Pd and Pt slabs of a (4 × 4 × 2) unit cell. Most papers predict that the hollow site is preferred for CO adsorption on transition metals, while experimental studies prove that CO adsorbs at the top site.[38] The PBE functional can overcome the underestimation of the CO preference of low-coordination sites. Hence we focused on the top site as the preferred site for CO adsorption. The density of states and the CO adsorption energy on the participating metal atoms were calculated with the adsorption energy being calculated based on the usual definition $E_{ads} = E(CO/metal) - E(CO) - E(metal)$.

Table 1 The deposited nanostructures with their calculated ECSA, and Pt, Pd and total mass

Porous PtPd NTs				
Pt-Content	Metal mass (mg)	Pt mass (mg)	ECSA (m^2 g_{metal}^{-1}) (H_2SO_4)	ECSA (m^2 g_{metal}^{-1}) ($HClO_4$)
5 at%	0.2417	0.0121	60.1	—
10 at%	0.2305	0.0231	100.3	137.7
18 at%	0.2359	0.0424	88.5	—
23 at%	0.2271	0.0476	84.2	91.3
43 at%	0.2924	0.1257	47.4	—
100 at%	0.1610	0.1610	34.6	49.5
PtPd NRs, ECSA in H_2SO_4 in m^2 g_{metal}^{-1}				
17 at%	0.2172	0.0593	37.3	
41 at%	0.2661	0.1491	20.6	
69 at%	0.3614	0.2902	12.7	
100 at%	0.3742	0.3742	17.6	

3. Results and discussion

3.1. Processing and microstructure characterization

Fig. 1 shows the SEM micrographs of the Pt and PtPd NTs, and Fig. 2 shows the EDS spectra and EDS mapping of a PtPd alloy NT sample. Plain NRs are also shown for comparison in the ESI† (Fig. S1). Fig. 1a is a top-view micrograph revealing the NT morphology with an NT wall thickness of approximately 15 nm. The inner tube diameter is approximately 65 nm. The porous characteristic of the NTs can be seen in Fig. 1b–d. Estimates of the pore size using the STEM micrographs in Fig. 3 yield a range between 2 and 3.5 nm. Further, a close look at Fig. 3 unveils a NT wall structure akin to a

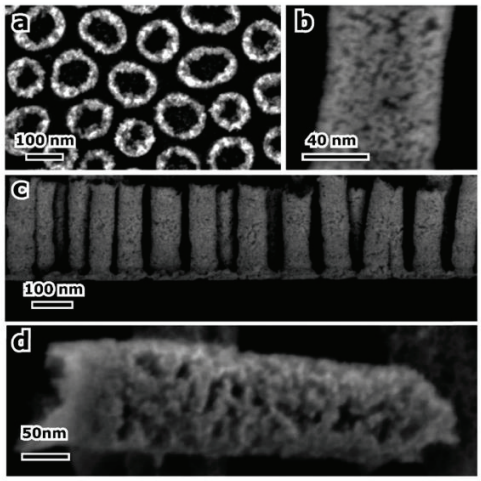

Fig. 1 SEM micrographs using the ESB mode (atomic number contrast at high resolution): (a) top view of the nanotubes. It shows the corrugated morphology of the NTs and suggests that the NTs are composed of NPs (see the main text for the discussion of the formation mechanisms of the NTs); (b and c) cross-section of the NT array showing their porous characteristic along their length; (d) an isolated NT (notice the rough morphology of the walls and their particulate characteristic).

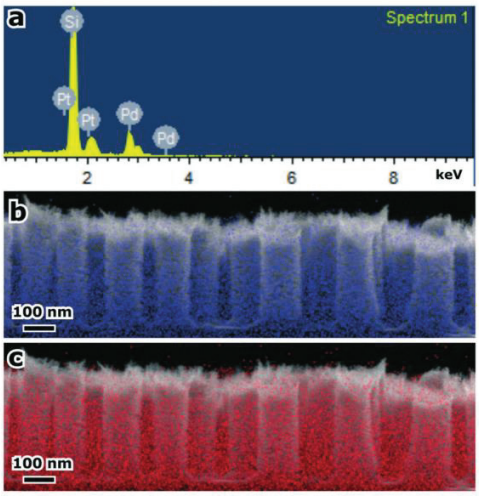

Fig. 2 (a) EDS spectrum of 43PtPd alloy NTs. The Si peak belongs to the substrate; (b and c) EDS mapping showing the homogeneous distribution of Pt (b) and Pd (c).

basket-weave structure having mesopores between the closely-knit nanocrystals.

Fig. 4 shows the XRD spectra of the Pt and PtPd NTs. The alloy composition is determined from the d_{111} interplanar spacing, assuming that Vegard's law holds for this system which is pretty much verified with the linear dependence of $d_{111} = f(X_{Pt})$. The composition is slightly different from EDS analysis (Table S1†), due to the difference in the analysed areas (XRD probes macroscopic volumes while EDS probes only microscopic ones). Using the Scherrer formula, the crystallite size amounts to 1.5 nm, assuming a shape factor, K = 1. A similar result of 1.6 nm was also obtained for the plain NRs. Further, the XRD results show the predominance of the 111 peak, but the ratio of the 200 peak area to that of 111 is roughly constant for all alloy NT compositions (Table 2). This also holds for the plain NRs. This structural similarity is important for a meaningful comparison of the electrocatalytic properties of the different alloys.

Considering the NT morphology obtained, we may infer that nucleation first occurs at the bottom of the pores (Au-electrode) and growth accrues from the nucleated clusters/NPs by attachment of newly formed NPs. Growth occurs vertically along the pore walls which are thought to act as heterogeneous nucleation sites. The result is akin to a vertically growing film on a substrate wall. The formation mechanisms of the porous NTs may further be discussed considering the time–current curves recorded during electrodeposition that are shown in Fig. 5 for Pt and PtPd alloys, and assuming complete wetting of the AAO pore channels (which is the case, because otherwise we wouldn't have electrodeposition in the pores). In the case of Pt-NTs, the current first increases with time culminating in a sharp maximum that denotes the formation of a high density of Pt nuclei. This regime is followed by a drop in the current that is generally an indication of diffusion-limited nucleation and growth because of

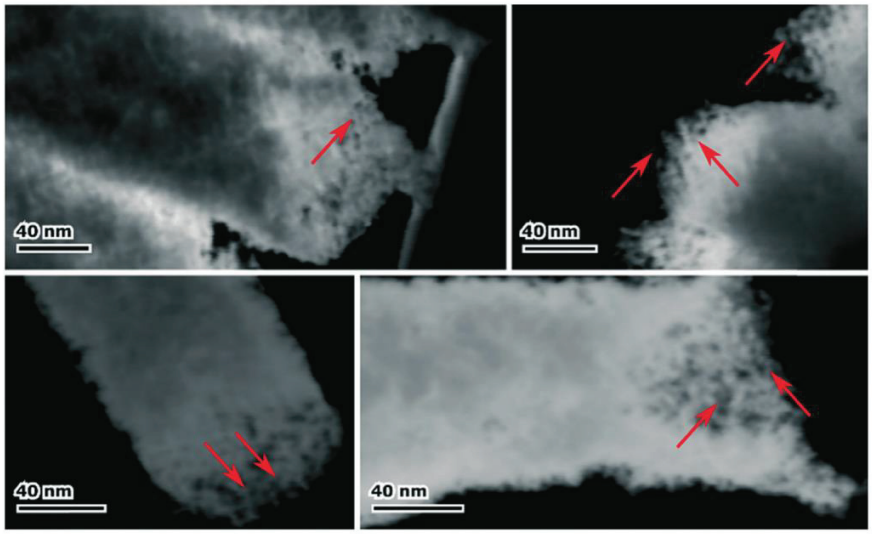

Fig. 3 STEM micrographs of PtPd NTs. The NTs were scratched from the sample surface and mounted on a TEM grid for STEM analysis. Regardless of alloy NT composition, all the micrographs illustrate the porous characteristic of the NT walls. Notice also the closely-knit NPs with a basket-weave structure displaying mesopores (arrows).

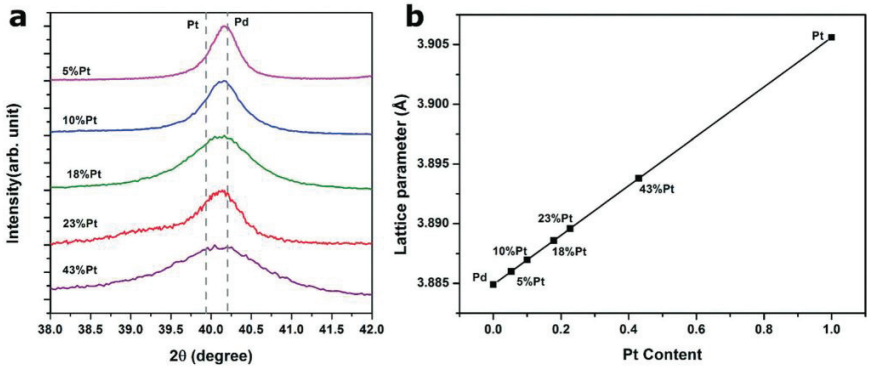

Fig. 4 (a) XRD patterns in the 2θ range of the 111 reflection in grazing incidence mode; (b) Pt concentration obtained from the calculated lattice parameters and Vegard's law.

solute depletion at the particle–electrolyte interface (due to nucleation and growth). At longer times, the current slowly increases again. In this regime, diffusion and kinetics control of nucleation proceeds.[39] A quasi-steady state regime follows where kinetics control predominates. Normally at high overpotential, where the driving force for nucleation and growth is large, agglomeration of NPs occurs leading to larger NPs and/or dendritic growth.[40,41] This is not the case in the present work, because the surfactant stabilizes the nuclei *via* the formation of micelles. At low Pt content (*e.g.* 10 at%), nucleation proceeds at low current over a longer lapse of time in comparison to pure Pt, leading to a broad maximum; a short diffusion limited and a steady state regime follow. This suggests that the kinetics of nucleation and growth of PtPd-NPs is more sluggish than in the case of Pt. With increasing Pt content, the nucleation and growth are even more sluggish that the diffusion-controlled regime is suppressed, meaning that the ion concentration at the electrode interface remains almost constant. We presume that the electrodeposition of PtPd is controlled by the degree of interaction between the Pd and Pt ions at the electrolyte–substrate interface. However, more studies are necessary in order to elucidate the electrodeposition mechanisms of PtPd alloys. In all cases, the NT microstructure remains unchanged, because of the effect of the surfactant in limiting the NP growth. Fig. S2† shows electrodeposited Pt from a Brij58-free electrolyte. The porosity is reduced, with the formation of shorter NRs for the same deposition time. A schematic of the electrodeposition mechanism is shown in Fig. 6.

Table 2 The ratio of the 200/111 peak area for the different Pt concentrations

Porous PtPd NTs	
5 at%	0.24
10 at%	0.28
18 at%	0.22
23 at%	0.21
43 at%	0.26
100 at%	0.31
Plain PtPd NRs	
17 at%	0.23
41 at%	0.27
69 at%	0.27
100 at%	0.30

3.2. Electrochemical properties

The electrochemical active surface area (ECSA) results are summarized in Fig. 7 that comparatively shows the ECSA of the porous NTs and the plain PtPd NRs. In Fig. 7b, the ratios of the ECSAs of the PtPd alloy NTs to those of pure Pt are shown. Noteworthy is the high ECSA ratio of the porous PtPd NTs to Pt-NRs which culminates at approximately 10 at% Pt. This shows that making porous PtPd NTs is an efficient way to substantially increase the ECSA in general. Moreover, the ECSA ratio of the same PtPd NTs to porous Pt NTs also shows a substantial increase with decreasing Pt content which

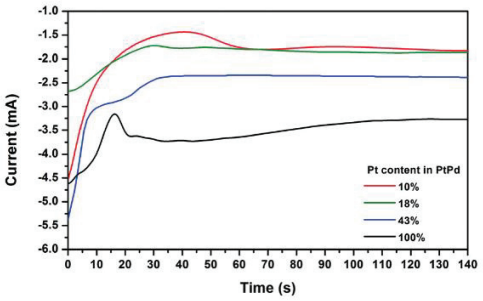

Fig. 5 The chronoamperometric curves corresponding to the potentiostatic electrodeposition of the Pt and PtPd NTs at −0.5 V (see the main text for discussion).

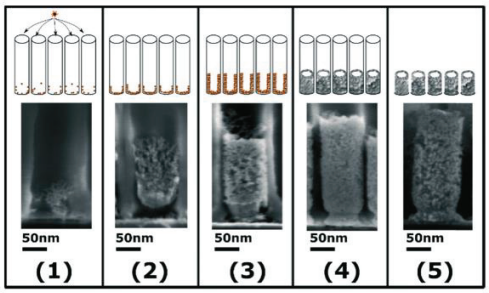

Fig. 6 A schematic of the deposition steps of the NTs from an electrolyte containing 3 wt% Brij58, and corresponding micrographs. (1) The NPs surrounded by Brij58 are nucleated on the bottom of the pore walls; (2) the newly formed NPs attach to the already formed NPs along the pore walls. This process involves mesopore formation; (3) and (4) the process proceeds under kinetics control; (5) NT deposition is finished and the AAO template is dissolved to expose the NTs.

points the way to better, Pt-lean catalysts. It should be pointed out that the metal mass in our work is calculated from the Faraday equation by integrating the deposition current *vs.* time, after subtracting the charge corresponding to the hydrogen evolution at −0.5 V (Fig. S3†). Because the charge necessary for the metal deposition is an accurate measure of the tiny masses, down to few micrograms, usual in electrocatalysis experiment, this entitles us to claim that our results are accurate inasmuch as any uncertainties related to weighing very small masses can be precluded (even high precision laboratory balances are not precise enough for weighing such masses, unless a quartz microbalance is used).

A salient feature in Fig. 7 is the existence of an ECSA maximum at 10 at% Pt with a value of roughly 100 m^2 g_{metal}^{-1} that is approximately twice the values reported for Pt-black.[42] Even the 5 at% Pt alloy is characterized by a higher ECSA than pure porous Pt-NTs and Pt-black. The ECSA of NTs with Pt contents higher than 10 at% first smoothly decreases, followed by a steeper decrease between 23 and 43 at% Pt, and saturates at higher Pt values. It goes without saying that the values of the Pt-NRs are smaller than those of the NTs. The values above were obtained using the H_{upd} method. According to Mayrhofer *et al.*,[43] this method rather yields values that are approximately 70 to 90% of the values obtained with the CO stripping method, depending on the particle size. Our results using the CO stripping method (Fig. S4†) for the 10PtPd NTs confirm this tendency. The ECSA value of 119 m^2 g_{metal}^{-1} is approximately 1.2 times higher than the 100 m^2 g_{metal}^{-1} obtained with the H_{upd} method in 0.5 M H_2SO_4. We may then state that the ECSA values tabulated in Table 1 are rather on the conservative side.

Further, for the sake of comparison with the results reported elsewhere,[30,44] Fig. 7 also shows the ECSA values obtained in 0.1 M perchloric acid, because most of the data on the PtPd nanocatalysts were generated in this electrolyte. The values obtained are approximately 16% higher with a maximum of 138 m^2 g^{-1} for the 10 at% Pt alloy that surpasses the ECSA reported on nanoscale Pt and PtPd nanowires,[30,44,45] Pt-coated Pd-NTs,[46] and Pt-containing quaternary alloy NTs.[47]

The overall high ECSA obtained in this work probably accrues from the positive interplay of different factors. The accessibility of both the inner and outer tube surfaces to the electrolyte and the nanometre-sized clusters certainly play a prominent role that is amplified by the mesoporous structure of the NTs. This probably entails full utilization of the Pt sites (*e.g.* Liu *et al.*[47] and Tian *et al.*[48]). Concerning the ECSA of the PtPd-NTs, there are additional contributing factors, among them the electron transfer between the two elements (transfer of d-electrons from Pd to Pt) and stress effects due to the lattice mismatch. Although the atomic radii of Pd and Pt are very close, lattice contraction in PtPd alloys has been claimed to have a positive effect on the electrocatalytic activity, *e.g.* for the ORR, as it lowers the affinity of Pt for oxygen, consequently enhancing the kinetics of O–H formation.[18,49,50]

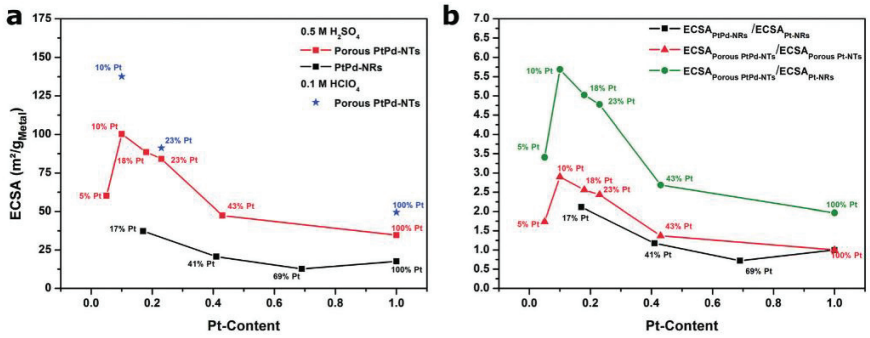

Fig. 7 (a) ECSA in 0.5 M H_2SO_4 for PtPd-NRs and porous PtPd NTs: the results in 0.1 $HClO_4$ are also shown for the sake of comparison with previous work (blue stars, see also the main text); (b) comparison of the ECSA ratios of the different nanostructures to stress the overall higher performance obtained for the PtPd alloys, and in particular that of the porous alloy NTs. The lines are guides for the eye.

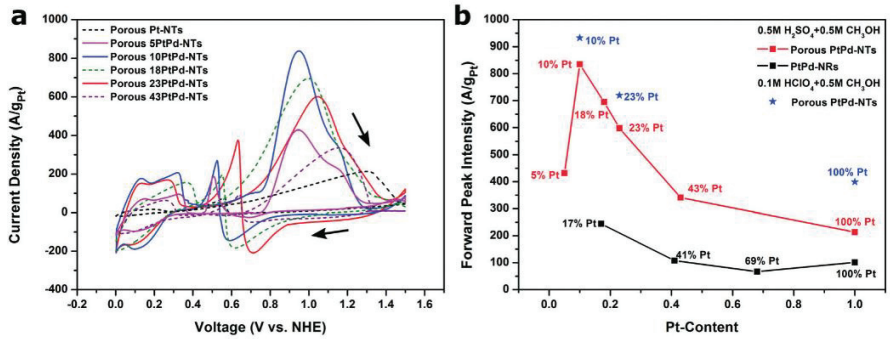

Fig. 8 (a) Current density (current normalized by the Pt-mass) *vs.* voltage of the sample electrodes in methanol; (b) the forward peak current density as a function of the Pt concentration. Scan rate: 50 mV s^{-1}.

The electrocatalytic activity for methanol oxidation is plotted in Fig. 8. The specific current density *vs.* voltage is plotted for the porous NTs in Fig. 8a. Broad forward peaks with a hump at higher voltages are observed. The forward peak is always more intense than the backward peak which is generally accepted as a result of lower propensity of the structure to poisoning with intermediate reaction species. This contrasts with the results obtained for plain Pt and PtPd NRs where the magnitude of the forward and backward peaks is roughly the same (Fig. S5†). Close examination of the forward peak of the lean Pt alloys reveals a main peak at peak voltages that tend to decrease with decreasing Pt concentration, followed by a hump at higher voltages with peak voltages showing the same tendency. Because the hump lies at peak voltages close to those of the Pt-rich alloy, it is intuitive to understand this result as a consequence of the existence of Pt-rich regions in the NTs. Recent investigations of segregation phenomena in PtPd alloys showed that when Pt is present as a solute, moderate segregation is predicted,[51] with Pt-segregation to the center of low index facets in nanoparticles.[52] At higher Pt concentration, *e.g.* 1:1, the same work predicts multishell chemical ordering with the formation of islands of the individual elements on low index facets, *e.g.* 111 for Pt and 100 for Pd, and a reverse order in the second shell. This contrasts with the well-known Pd-segregation in bulk PtPd alloys[51,53] that is explained by the lower surface energy of Pd.

Because methanol electrooxidation occurs solely on Pt surface sites, we may infer Pt-segregation at the surface of the PtPd-NTs and/or the presence of Pt sites at the surface. At low Pt-concentration, *e.g.* 10 to 20 at%, the formation of a Pt skin, as predicted by Barcaro *et al.*,[52] should explain the maximum activity obtained. We presume that lower concentrations (than 10 at%) result in less Pt surface sites. In other terms, a “percolation limit” is not reached to form the Pt clusters predicted in the work above. Higher concentrations are supposed to lead to more Pd-sites on the surface which again decreases the electrocatalytic activity. We contrast our results to those obtained by Wu *et al.*[16] who reported two maxima for the ORR activity of their PtPd nanoalloy NPs; the

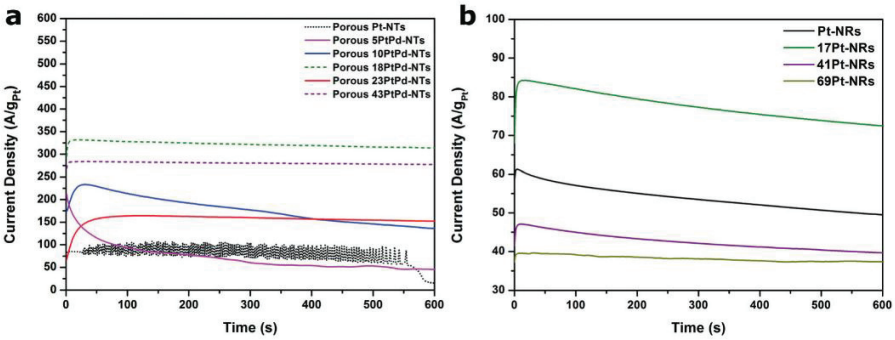

Fig. 9 Chronoamperometric curves of the different 1D nanostructures of methanol electrooxidation in 0.5 M H_2SO_4. The test voltage was fixed at 80% of the peak voltage of the corresponding structure (obtained from Fig. 8a). (a) Porous NTs and (b) plain NRs.

Table 3 Adsorption energies (E_{ads}), distance C–O (d_{C-O}), and distance C–metal (d_{C-M})

Surface site	E_{ads} (eV)	d_{C-O} (Å)	d_{C-M} (Å)
Pt-top	−1.751	1.157	1.821
Pd-top	−1.346	1.141	1.549
PtPd, Pt-top	−1.286	1.139	1.315
PtPd, Pd-top	−1.859	1.192	1.702

first one is observed for Pt lean alloys (14 at% Pt) and the second one for Pt-rich alloys (64 at% Pt). A minimum is obtained by them at roughly 50 at% Pt. They explain their results, based amongst others on XPS and DFT calculations, with “subtle” electron transfers from Pt to Pd, depending on composition. We cannot confirm their findings, at least with regard to our methanol electrooxidation results. Rather, (the trend shown in Fig. 8b for both the NTs and the NRs is proof enough) electron transfer processes from Pd to Pt (see also our DFT calculations below), segregation phenomena as predicted by Nielekar *et al.*,[51] and lattice contraction effects are thought to dominate the electrocatalytic activity of our nanostructures.[49,50]

Chronoamperometric experiments for methanol electrooxidation were conducted in 0.5 M H_2SO_4 at a fixed voltage V/V_p ratio of 0.8, where V_p is the peak voltage. Although the test time is too short for a conclusive assessment of the long-term property stability, it nonetheless allows us to compare the different nanoalloy NTs. The results reveal morphology and composition specific behaviours. In the case of the porous NTs, Fig. 9a, it is noteworthy that the alloys with higher Pt-concentration are more stable than the Pt-lean ones. For instance, all the alloys with Pt >10 at% barely show a variation in their performance with time, at least for the lapse of time tested. For the 10 at% and 5 at% Pt, a decrease in performance of approximately 38% is revealed. A similar trend can be suggested for the plain PtPd NRs, Fig. 9b. These results indicate that the concentration of Pd in the alloy, in other words, the number of Pd atoms neighbouring Pt, must play a role in preventing site blocking by intermediate species during the electrocatalytic reaction. We should now shed some light on these observations *via* DFT calculations, particularly considering CO adsorption energies on Pt, Pd and PtPd alloys.

4. Density functional theory calculations

Table 3 shows the calculated CO adsorption energies on the top-sites of Pt and Pd atoms in the pure metals and the 1 : 1 alloy (Pt or Pd in the bimetallic PtPd). For the pure metals, we first note the higher stability of adsorbed CO on Pt atoms, with a difference of 0.405 eV, in comparison to the adsorption on Pd atoms. Gajdoš *et al.*[54] reported a lower adsorption energy difference between Pt and Pd (0.16 eV), probably because of the different calculation methods involved. But qualitatively, our results are in good agreement with theirs in terms of the preferential adsorption of CO on Pt. The PtPd alloy, however, shows a completely different behaviour with the adsorption of CO being now preferred on Pd rather than on Pt (an energy difference of roughly 0.5 eV in favour of CO adsorption on Pd might be exaggerated, but qualitatively confirms the tendency above). This result can be rationalized considering that the charge transfer from Pd to Pt should

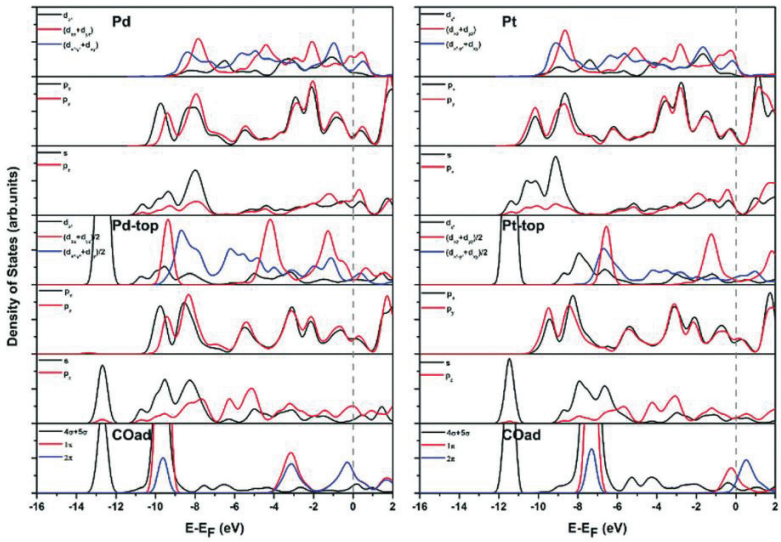

Fig. 10 Orbital electronic density of states for Pt/Pd atoms in a Pt1 : Pd1 alloy. The Pt/Pd top sites and adsorbed CO are shown.

increase the ability of Pd to accept charges from CO. In fact, the underlying mechanisms for the interaction between CO and transition metals can be described in terms of two contributions, a strong σ-donation of electrons from CO to the empty metal orbitals, and a good back-donation of electrons from the metal to the unoccupied molecular orbitals π^*.[55]

The density of states calculated for the pure metals and adsorbed CO is shown in Fig. S6.† They are qualitatively in agreement with the literature.[38]

Considering Pt and Pd in the PtPd mixed structures (Fig. 10), the d band of Pt is shifted to a lower energy (−3.63 eV) and is almost fully occupied in comparison with that of pure Pt (Fig. S6†). The Pd d band covers a larger energy range than that of pure Pd, and its center blue-shifts to −2.67 eV. The interaction between Pt and Pd translates to a transfer of charges from Pd to Pt as suggested by the full occupation of the Pt d-band, and the shift of the p_y band (to lower energies for Pt and to higher energies for Pd). From the panels Pd-top and Pt-top, the hybridization between the d-band of the Pd atoms and CO σ lies at lower energies than that for the Pt atoms. One can easily see the rise of new Pd band states (sp_z and d) arising from the donation of charges from CO. This donation seems much more important than in the case of pure Pd (Fig. S6†), since the transfer of charges from Pd to Pt atoms increases the capacity of Pd to accept more charges from CO. One can also observe from the CO panel that the $4\sigma + 5\sigma$ is shifted to more positive energies when CO adsorbs on Pt in the PtPd alloy. Further, a weak occupation of the 2π states is observed on Pd atoms, proving some degree of back-donation from Pd to 2π. Fig. 11 shows a summary of the d-band changes from pure Pt/Pd to Pt/Pd in the PtPd alloy structure.

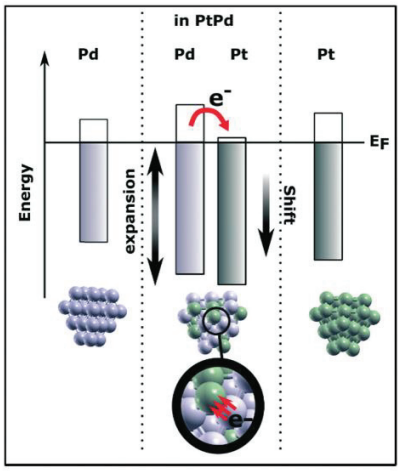

Fig. 11 A schematic summary of d-band changes of pure Pt/Pd and Pt/Pd in the mixed PtPd structure. The transfer of charges from Pd to Pt causes d-band filling of empty states above the Fermi level which translates to a d-band shift to lower energies. In contrast, the d-band of Pd in PtPd expands over a larger energy range due to Pt–Pd interaction.

The DFT calculations above, although still at the preliminary stage and certainly need more refinement for a better description of the PtPd nanoalloys, qualitatively explain the electrocatalytic performance observed in this work. Considering our experimental results, the presence of Pd in the NTs plays an important role, first by charge transfer to Pt atoms which reduces the capacity of Pt to be poisoned by CO. Second, the preferential adsorption of CO on Pd leaves more free, active Pt sites. The enhancement of the activity for Pt-lean alloys depicted in Fig. 8b can be explained in terms of more Pd atoms neighbouring Pt sites.

5. Conclusion

Supported 1D PtPd nanostructures with different Pt concentrations in the range from 5 to 100 at% were processed using electrodeposition in the pores of aluminum oxide template films. Using a negative deposition voltage of −0.5 V together with a small amount of a non-ionic surfactant allows the processing of mesoporous NTs. The electrochemical performance of the different nanostructures and alloys in sulfuric acid and occasionally also in perchloric acid electrolytes is compared. Both the electrochemical active surface area (ECSA) and the activity for methanol electrooxidation very much depend on the Pt concentration. We show that the ECSA increases with decreasing Pt-content towards a maximum at 10 at% and decreases at lower values. The maximum values obtained for the ECSA of the NT structures amount to 100 $m^2\ g_{metal}^{-1}$ in 0.5 M H_2SO_4 and 138 $m^2\ g_{metal}^{-1}$ in 0.1 M $HClO_4$. Even at 5 at% Pt, the ECSA value obtained is higher than those of Pt-black and pure Pt-NTs. Understandably, the catalytic performance for methanol electrooxidation also increases with decreasing Pt content, with a maximum of 835 A g_{Pt}^{-1} in 0.5 M H_2SO_4 and 932 A g_{Pt}^{-1} in 0.1 M $HClO_4$. The NT structure, mesoporosity, lattice contraction and charge transfer from Pd to Pt are thought to contribute to these results. Furthermore, the chronoamperometric tests suggest the long-term stability of the nanostructures investigated. At the atomic level, DFT calculations show that charge transfer from Pd to Pt as well as the preferential adsorption of CO on Pd in the PtPd alloy might account for the properties observed.

Conflicts of interest

There are no conflicts to declare.

Acknowledgements

This work has no financial support.

Notes and references

1 C. Lin, S. S. Shinde, Z. Jiang, X. Song, Y. Sun, L. Guo, H. Zhang, J.-Y. Jung, X. Li and J.-H. Lee, *J. Mater. Chem. A*, 2017, 5, 13994.

2 S. Du, C. Koenigsmann and S. Sun, *One-dimensional Nanostructures for PEM Fuel Cell Applications*, Hydrogen and fuel cells primers, Academic Press an imprint of Elsevier, London, San Diego CA, 2017.
3 C. Koenigsmann, M. E. Scofield, H. Liu and S. S. Wong, *J. Phys. Chem. Lett.*, 2012, **3**, 3385.
4 C. Koenigsmann and S. S. Wong, *Energy Environ. Sci.*, 2011, **4**, 1161.
5 Y. Lu, S. Du and R. Steinberger-Wilckens, *Appl. Catal., B*, 2016, **199**, 292.
6 H. Huang, L. Ma, C. S. Tiwary, Q. Jiang, K. Yin, W. Zhou and P. M. Ajayan, *Small*, 2017, **13**, 1603013.
7 H. Qiu and F. Zou, *ACS Appl. Mater. Interfaces*, 2012, **4**, 1404.
8 B. Narayanamoorthy, K. K. R. Datta, M. Eswaramoorthy and S. Balaji, *ACS Catal.*, 2014, **4**, 3621.
9 X. Du, S. Luo, H. Du, M. Tang, X. Huang and P. K. Shen, *J. Mater. Chem. A*, 2016, **4**, 1579.
10 V. R. Stamenkovic, B. S. Mun, K. J. J. Mayrhofer, P. N. Ross and N. M. Markovic, *J. Am. Chem. Soc.*, 2006, **128**, 8813.
11 E. Antolini, J. R. C. Salgado and E. R. Gonzalez, *J. Power Sources*, 2006, **160**, 957.
12 Y. Bing, H. Liu, L. Zhang, D. Ghosh and J. Zhang, *Chem. Soc. Rev.*, 2010, **39**, 2184.
13 L. Liu, E. Pippel, R. Scholz and U. Gösele, *Nano Lett.*, 2009, **9**, 4352.
14 C. Zhu, S. Guo and S. Dong, *Adv. Mater.*, 2012, **24**, 2326.
15 B. Y. Xia, H. B. Wu, N. Li, Y. Yan, X. W. D. Lou and X. Wang, *Angew. Chem., Int. Ed.*, 2015, **54**, 3797.
16 J. Wu, S. Shan, H. Cronk, F. Chang, H. Kareem, Y. Zhao, J. Luo, V. Petkov and C.-J. Zhong, *J. Phys. Chem. C*, 2017, **121**, 14128.
17 J. Ying, X.-Y. Yang, Z.-Y. Hu, S.-C. Mu, C. Janiak, W. Geng, M. Pan, X. Ke, G. Van Tendeloo and B.-L. Su, *Nano Energy*, 2014, **8**, 214.
18 N. M. Marković, T. J. Schmidt, V. Stamenković and P. N. Ross, *Fuel Cells*, 2001, **1**, 105.
19 Z. Chen, M. Waje, W. Li and Y. Yan, *Angew. Chem.*, 2007, **119**, 4138.
20 H.-Y. Chen, M.-X. Jin, L. Zhang, A.-J. Wang, J. Yuan, Q.-L. Zhang and J.-J. Feng, *J. Colloid Interface Sci.*, 2019, **543**, 1.
21 J.-J. Lv, J.-N. Zheng, S.-S. Li, L.-L. Chen, A.-J. Wang and J.-J. Feng, *J. Mater. Chem. A*, 2014, **2**, 4384.
22 S.-S. Li, J.-N. Zheng, X. Ma, Y.-Y. Hu, A.-J. Wang, J.-R. Chen and J.-J. Feng, *Nanoscale*, 2014, **6**, 5708.
23 T. Ishimoto and M. Koyama, *J. Phys. Chem. Lett.*, 2016, **7**, 736.
24 H. X. Zhang, C. Wang, J. Y. Wang, J. J. Zhai and W. B. Cai, *J. Phys. Chem. C*, 2010, **114**, 6446.
25 Y. Liu, M. Chi, V. Mazumder, K. L. More, S. Soled, J. D. Henao and S. Sun, *Chem. Mater.*, 2011, **23**, 4199.
26 Y. Xu and B. Zhang, *Chem. Soc. Rev.*, 2014, **43**, 2439.
27 L. Kuai, B. Geng, S. Wang and Y. Sang, *Chemistry*, 2012, **18**, 9423.
28 X. Xia, Y. Wang, A. Ruditskiy and Y. Xia, *Adv. Mater.*, 2013, **25**, 6313.
29 H. Duan and C. Xu, *Electrochim. Acta*, 2015, **152**, 417.
30 C. Li, T. Sato and Y. Yamauchi, *Angew. Chem., Int. Ed.*, 2013, **52**, 8170.
31 S. M. Alia, G. Zhang, D. Kisailus, D. Li, S. Gu, K. Jensen and Y. Yan, *Adv. Funct. Mater.*, 2010, **20**, 3742.
32 M. Es-Souni and S. Habouti, *Front. Mater.*, 2014, **1**, 19.
33 N. Berger and M. Es-Souni, *Langmuir*, 2016, **32**, 6985.
34 E. J. Coleman, M. H. Chowdhury and A. C. Co, *ACS Catal.*, 2015, **5**, 1245.
35 H. Liu, C. Koenigsmann, R. R. Adzic and S. S. Wong, *ACS Catal.*, 2014, **4**, 2544.
36 P. Giannozzi, S. Baroni, N. Bonini, M. Calandra, R. Car, C. Cavazzoni, D. Ceresoli, G. L. Chiarotti, M. Cococcioni, I. Dabo, A. Dal Corso, S. De Gironcoli, S. Fabris, G. Fratesi, R. Gebauer, U. Gerstmann, C. Gougoussis, A. Kokalj, M. Lazzeri, L. Martin-Samos, N. Marzari, F. Mauri, R. Mazzarello, S. Paolini, A. Pasquarello, L. Paulatto, C. Sbraccia, S. Scandolo, G. Sclauzero, A. P. Seitsonen, A. Smogunov, P. Umari and R. M. Wentzcovitch, *J. Phys.: Condens. Matter*, 2009, **21**, 395502.
37 J. P. Perdew, K. Burke and M. Ernzerhof, *Phys. Rev. Lett.*, 1996, **77**, 3865.
38 A. Stroppa, K. Termentzidis, J. Paier, G. Kresse and J. Hafner, *Phys. Rev. B: Condens. Matter Mater. Phys.*, 2007, **76**, 195440.
39 L. Guo and P. C. Searson, *Electrochim. Acta*, 2010, **55**, 4086.
40 J. Ustarroz, B. Geboes, H. Vanrompay, K. Sentosun, S. Bals, T. Breugelmans and A. Hubin, *ACS Appl. Mater. Interfaces*, 2017, **9**, 16168.
41 J. Ustarroz, T. Altantzis, J. A. Hammons, A. Hubin, S. Bals and H. Terryn, *Chem. Mater.*, 2014, **26**, 2396.
42 X. Yu, D. Wang, Q. Peng and Y. Li, *Chem. Commun.*, 2011, **47**, 8094.
43 K. J. J. Mayrhofer, D. Strmcnik, B. B. Blizanac, V. Stamenkovic, M. Arenz and N. M. Markovic, *Electrochim. Acta*, 2008, **53**, 3181.
44 S. Du, Y. Lu and R. Steinberger-Wilckens, *Carbon*, 2014, **79**, 346.
45 Q. Xiao, M. Cai, M. P. Balogh, M. M. Tessema and Y. Lu, *Nano Res.*, 2012, **5**, 145.
46 S. M. Alia, K. O. Jensen, B. S. Pivovar and Y. Yan, *ACS Catal.*, 2012, **2**, 858.
47 L. Liu and E. Pippel, *Angew. Chem., Int. Ed.*, 2011, **50**, 2729.
48 X. L. Tian, Y. Y. Xu, W. Zhang, T. Wu, B. Y. Xia and X. Wang, *ACS Energy Lett.*, 2017, **2**, 2035.
49 J. Greeley, I. E. L. Stephens, A. S. Bondarenko, T. P. Johansson, H. A. Hansen, T. F. Jaramillo, J. Rossmeisl, I. Chorkendorff and J. K. Nørskov, *Nat. Chem.*, 2009, **1**, 552.
50 B. Lim, M. Jiang, P. H. C. Camargo, E. C. Cho, J. Tao, X. Lu, Y. Zhu and Y. Xia, *Science*, 2009, **324**, 1302.
51 A. U. Nielekar, A. V. Ruban and M. Mavrikakis, *Surf. Sci.*, 2009, **603**, 91.
52 G. Barcaro, A. Fortunelli, M. Polak and L. Rubinovich, *Nano Lett.*, 2011, **11**, 1766.
53 L. Fiermans, R. D. Gryse, G. D. Doncker, P. A. Jacobs and J. A. Martens, *J. Catal.*, 2000, **193**, 108.
54 M. Gajdoš, A. Eichler and J. Hafner, *J. Phys.: Condens. Matter*, 2004, **16**, 1141.
55 G. Blyholder, *J. Phys. Chem.*, 1964, **68**, 2772.

Supplementary materials

Porous PtPd alloy nanotubes. Towards high performance electrocatalysts with low Pt-loading

Ayoub Laghrissi [a] and Mohammed Es-Souni * [a]

[a] Institute for Materials & Surface Technology, University of Applied Sciences, Kiel, Germany

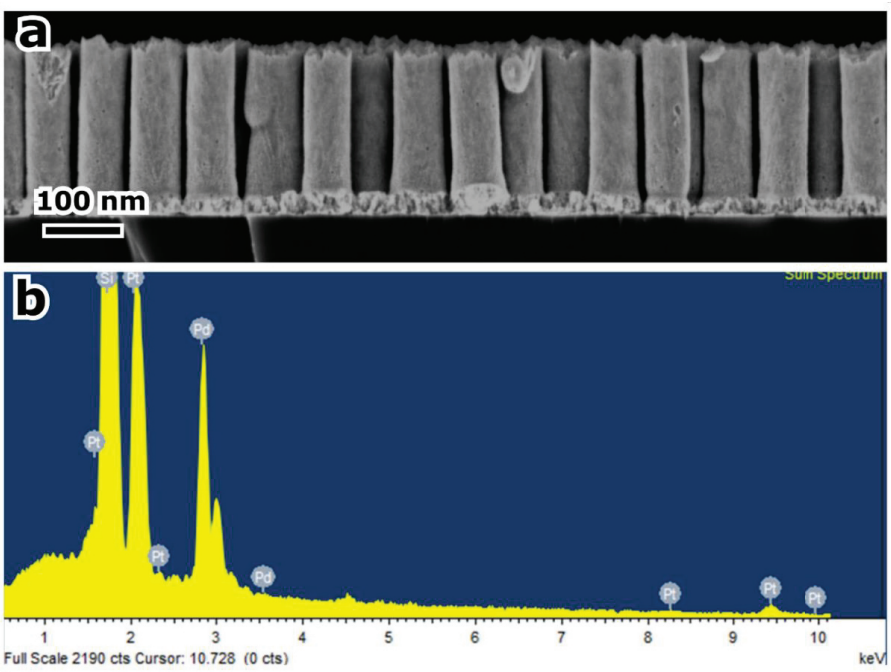

Fig. S1 SEM micrograph showing a cross section of a PtPd alloy NRs sample (a) , and corresponding EDS spectrum (b).

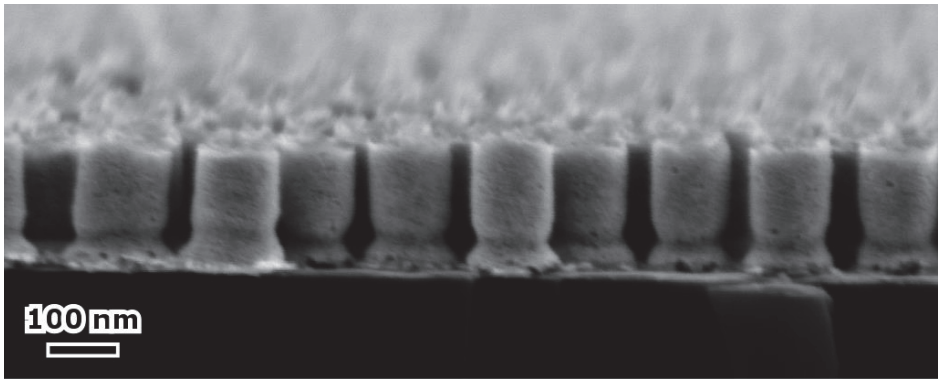

Fig. S2 Cross-section of Pt array electrodeposited at -0.5 V with no Brij58 in the solution.

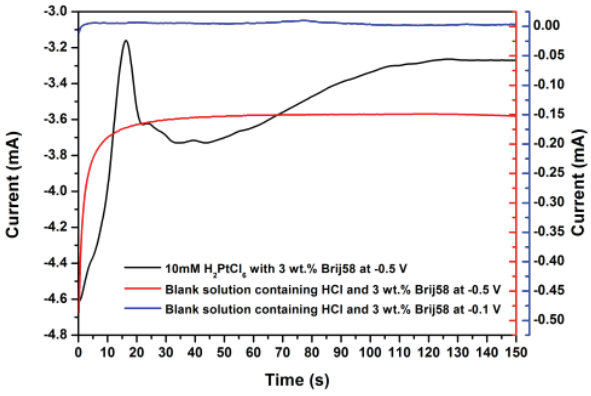

Fig. S3 The chronoamperometric curves corresponding to the potentiostatic electrodeposition of the porous Pt NTs at -0.5 V, and hydrogen evolution test done in a blank solution containing HCl and 3 wt.% Brij58 (pH=2.5) at -0.1 V and -0.5 V.

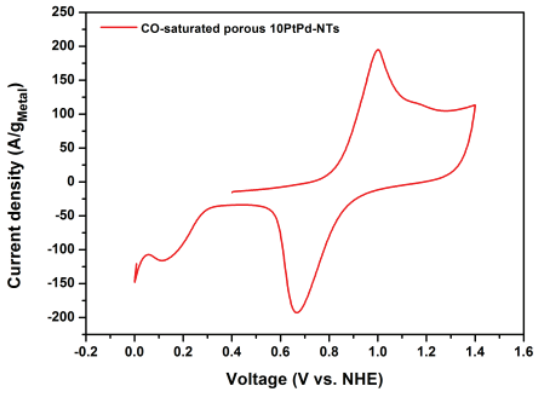

Fig. S4 CO oxidation voltammogram of a CO-saturated porous 10PtPd-NTs in CO-free 0.5 M H_2SO_4 electrolyte. Scan rate: 50 mV s^{-1}.

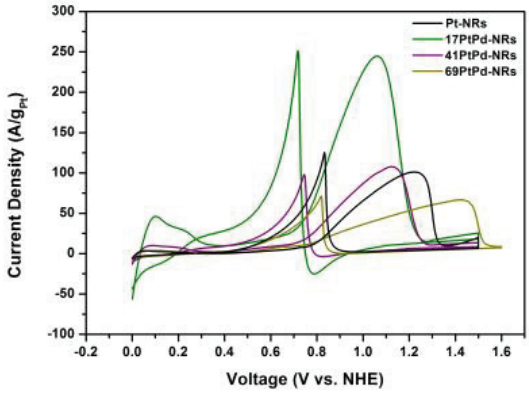

Fig. S5 Current density (current normalized by the Pt-mass) vs. voltage of the plain PtPd-NRs containing different Pt-contents in 0.5 M H_2SO_4 + 0.5 M CH_3OH. Scan rate: 50 mV s^{-1}.

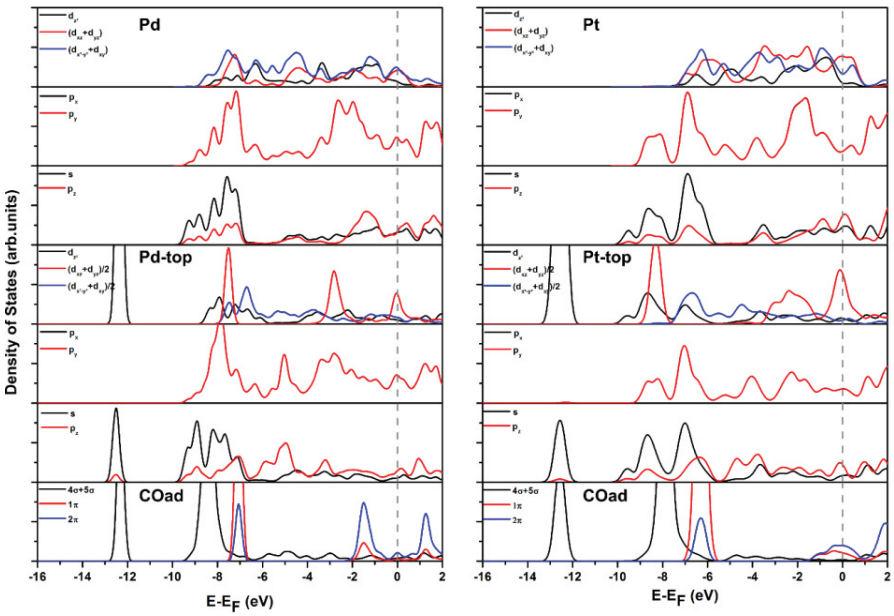

Fig. S6 Orbital electronic density of states for top sites of pure Pt, and Pd atoms, and adsorbed CO. This Figure shows s, p, and d –states for pure Pd and Pt. The d band center is -2.41 eV for Pt and -1.94 eV for Pd, the s- and p-band are covering a large energy range. p_x and p_y degenerate, and the p_z show different behavior than later ones. Considering the effect of CO molecule on the metal states Pd and Pt, one can observe different qualitative behaviors, the d-band is extended to a large energy range; more important new states were a rise in d_z^2 and sp_z from the interaction with σ. For CO the 4σ+5σ peaks positions for Pt (-8.5 eV) and Pd (-8 eV), the 2π get partially occupied at the same energy level with 1π.

Table S1 Volume fractions of 10 mM H_2PtCl_6 and 10 mM K_2PdCl_4 aqueous electrolytes, and their corresponding Pt-content obtained from EDS analysis, and from XRD (the calculated lattice parameters and Vegard’s law).

Volume Fraction	Pt-Content from EDS (at%)	Pt-Content from XRD (at%)
Porous PtPd NTs		
1:19	5.5	5
2:18	10.54	10
3:16	17.44	18
4:16	22.40	23
7:12	49.04	43
Plain PtPd NRs		
1:4	10.78	17
4:5	42.24	41
7:4	68.51	69

7 “Au-Nanorods supporting Pd and Pt nanocatalysts for the hydrogen evolution reaction: Pd is revealed a better catalyst than Pt”

Ayoub Laghrissi, Mohammed Es-Souni
IMST Institute for Materials and Surface Technology, University of Applied Sciences Kiel, Kiel, Schleswig-Holstein, Germany

Electrodeposited monolithic Au nanorods (NRs) of 100 nm in length, Au/Pd NRs of 100/20 nm in length, and Pt and Pd nanodiscs (NDs) with a 20-nm thickness are compared to magnetron sputtered Pt and Pd on Au-NRs’ supports. The sputtered Pt and Pd form a thin layer of nanoparticles (NPs) that is distributed across the entire surface area of the Au NRs. The linear sweep voltammetry behavior at 0.5 M H_2SO_4 of electrodeposited nanostructures shows a moderate performance for both Pt and Pd discs. Those behaviors largely improve with sputtered Pt and Pd due to NPs morphology, which increases the interfacial electronic interaction between Au and Pt/Pd. Surprisingly, sputtered Pd shows superior activity compared to sputtered Pt (Pd 32 and Pt 23 mA/cm² at -0.4 V). the Tafel slopes decrease for sputtered Pt and Pd compared to monolithic structures. Density functional theory calculations reveal the underlying effect of Au on both the hydrogen diffusion ability over Pt and Pd and on the HER mechanisms, which seem to follow Heyrovsky-Tafel mechanisms when sputtering Pd on Au NRs and strengthen Volmer-Tafel mechanisms for sputtered Pt on Au NRs.

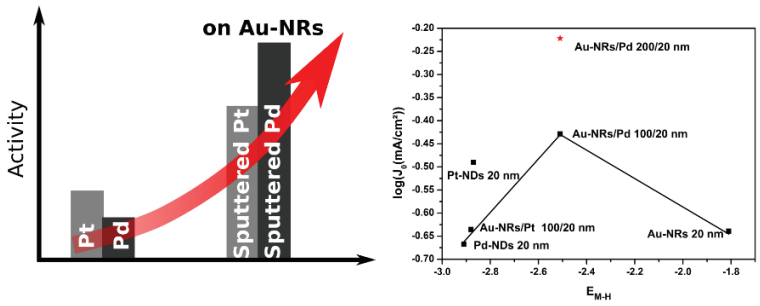

Prof. Dr. Mohammed Es-Souni designed the underlying concept. The author of the dissertation carried out the experiments and evaluated them. The author prepared the first draft and Prof. Dr. Mohammed Es-Souni validated the results and corrected the manuscript.

Au-Nanorods supporting Pd and Pt nanocatalysts for the hydrogen evolution reaction: Pd is revealed a better catalyst than Pt

Ayoub Laghrissi and Mohammed Es-Souni *

Institute for Materials & Surface Technology, University of Applied Sciences, Grenzstrasse 3, D-24149 Kiel, Germany.

*Correspondence: mohammed.es-souni@fh-kiel.de

Abstract

Ordered thin films of Au nanorods (NRs) on Ti/Au/Si heterostructure substrates are electrodeposited in thin film aluminum oxide templates, and serve, after template removal, as supports for Pd and Pt nanocatalysts. Based on previous work which showed a better electrocatalytic performance for layered Au/Pd nanostructures than monolithic Pd, electrodeposited 20 nm Pd discs on Au-NRs are first investigated in respect to their catalytic activity for the hydrogen evolution reaction (HER) and compared to monolithic 20 nm Pd and Pt discs. To boost performance still more, the interfacial interaction area between the Au-NRs supports and the active metals (Pt and Pd) was then increased via magnetron sputtering an extremely thin layer of Pt and Pd (20 nm overall sputtered thickness) on the Au-NRs after template dissolution. In this way the whole NR surface, top and lateral, was covered with Pt and Pd nanoparticles, ensuring a maximum interfacial contact between the support and the active metal. The HER performance obtained then was substantially higher than that of the other nanostructures. A Salient result of the present work, however, is the superior activity obtained for sputtered Pd on Au in comparison to that of sputtered Pt on Au. It is also shown that increasing the Au-NR length translates in a strong increase in performance. Density functional theory calculations show that the interfacial electronic interactions between Au and Pd lead to suitable values of hydrogen adsorption energy on all possible sites thus promoting faster (barrier-free diffusion) of adsorbed hydrogen and its recombination to H_2. A Volmer-Heyrovsky mechanism for HER is proposed and a volcano plot is suggested based on the results of the Tafel plots and the calculated hydrogen adsorption energies.

KEYWORDS

Hydrogen evolution reaction; Bimetallic Au-Pt-Nanorods; Bimetallic Au-Pd-Nanorods; Nanoelectrocatalysts; Hydrogen adsorption energy; density functional theory

Introduction

The ever-increasing share of renewables in the energy mix is understandably driven by environmental concerns. In many regions of the world the share of renewables is now at least 20%, and is expected to increase during the coming decade to 40 or even 50% [1,2]. Primarily, this trend has been boosted by recent developments in Li-ion battery modules that became much more competitive as Li price on the world market continues to fall [3]. Nevertheless, an efficient exploitation of renewables will also have to draw into consideration other energy storage possibilities, such as (super)capacitors and water electrolysis, to mention only the electrochemical methods. In particular, water electrolysis, mainly for the production of hydrogen via the hydrogen evolution reaction (HER), is highly attractive, and could afford a powerful way for energy storage that is clean and sustainable, and could be used even in remote and desertic regions.

HER is a complex electrochemical interfacial process that follows specific mechanisms depending on pH, catalyst and applied voltage. These mechanisms and the type of reactions involved at the interface between electrolyte and catalyst are outlined in the review article by Conway and Tilak [4]. The generally accepted reaction steps using a metal (M) catalyst under acidic conditions are [4-6]:

$H_3O^+ + M + e^- \rightarrow MH_{ads} + H_2O$ (Volmer reaction) (1)

followed by either Reaction (2) or (3)

$MH_{ads} + H_3O^+ + e^- \rightarrow H_{2\uparrow} + M + H_2O$ (Heyrovsky reaction) (2)

$2MH_{ads} \rightarrow H_{2\uparrow} + 2M$ (Tafel reaction) (3)

The mechanisms of HER have been rationalized by different authors in terms of the governing equations specific to the mechanisms above, taking into account the different acting kinetics parameters such as adsorbed hydrogen surface coverage and overpotential (e.g. Conway and Tilak [4], Bhardwaj et al. [7]). A number of catalysts have been reported for the HER, including transition metals and various compounds, as compiled in the review article of Eftikhari [8]. Catalyst performance is generally weighed in terms of the magnitude of overpotential necessary for HER at a given pH, the current density generated/weight of the active catalyst and durability. The noble metals (Pt, Pd) that are mostly used in acidic conditions are well known for their outstanding performance. In particular, Pt-NPs are the best known HER catalysts to date, performing at very

low overpotentials. Although other non-noble metal catalysts such as Ni and Ni-Mo [9], as well as non-metallic catalysts, including FeS_2, MoS_2 [10], as well as C_3N_4 [11] are now in the focus of research, Pt-group metals still enjoy vivid interest, particularly as to strategies to decrease their loading and the governing HER mechanisms (see results and discussion below).

In a previous work, we have shown that layered Au-Pd-nanorods (NRs) are powerful electrocatalysts for formic acid electrooxidation [12]. Controlling the Pd-layer thickness to few nanometers was shown to drastically increase the performance of the catalyst. Further, it was shown, also using functional density calculation, that Au plays an active role in preventing catalyst poisoning by catalyzing the oxidation of CO. Based on this work, the feasibility of these catalysts for HER is explored. In particular, it is shown that increasing the interfacial contact area between Au and the active metals Pd and Pt results in performances that by far surpass those of the layered and monolithic Pt and Pd nanostructures. This is achieved by magnetron sputtering a very thin layer of overall 20 nm thickness of the metals on exposed Au-NRs (i.e NRs after removal of porous aluminum oxide template) which leads to nanoparticle formation and distribution on top and lateral surfaces of the Au-NRs thus maximizing the interfacial contact area between the support and the active metal. Our results unambiguously show that sputtered Pd on Au-NRs has a substantially higher HER performance than that of sputtered Pt on the same Au-NRs. The results are rationalized in terms of hydrogen adsorption energy on different sites of Au-Pd(Pt)-bimetallic structures, using density functional theory calculations.

Materials and methods

Synthesis and characterization

The following chemicals were used as purchased: oxalic acid dihydrate 99 % (Roth, Karlsruhe, Germany), phosphoric acid 85 % (Roth, Karlsruhe, Germany), and sodium hydroxide (Roth, Karlsruhe, Germany). Gold (III) Chloride Trihydrate (Sigma-Aldrich, Steinheim, Germany). Potassium tetrachloropalladate(II) (abcr, Karlsruhe, Germany). Chloroplatinic acid hexahydrate (Sigma-Aldrich, Steinheim, Germany). Deionized water was used to prepare aqueous solutions.

Aluminum thin films of approximately 500 nm were deposited on a Silicon/Ti (2 nm)/Au (5 nm) heterostructure via electron beam evaporation (PVD75, Lesker, Jefferson Hills, USA equipped with an electron beam system (Ferrotec GmbH, Unterensingen, Germany). Anodization was conducted potentiostatically in 0.1 M oxalic acid at 70 V in a two-electrode set-up with a Pt

mesh as the counter electrode, using an electrochemical workstation (Keithley 2400 SM, Cleveland, USA). After anodization, barrier layer removal and pore widening were conducted in phosphoric acid (5 wt.% in water) for 50 minutes at 30° C [13,14]. Au-NRs, Pt-NRs and Pd-NRs were grown into the AAO pores via electrodeposition in 8 mM $HAuCl_4$, 10 mM H_2PtCl_6, and 10 mM K_2PdCl_4 aqueous electrolyte using a three-electrode set-up, with the Au/AAO template working electrode, a Pt counter electrode and an Ag/AgCl reference electrode, under potentiostatic conditions (Au at 0.1 V, Pt at -0.2 V, and Pd was first initiated at -0.1 V for 30 s and subsequently the voltage was increased to 0.3 V) using an electrochemical workstation (Princeton Potentiostat/Galvanostat Model 263A, Oak Ridge, USA). Au/Pd-NRs were grown into the pores by sequential electrodeposition from aqueous electrolytes. The NRs length was controlled via the deposition time. After electrodeposition, the 1D nanostructures were exposed by dissolving the AAO film in an aqueous solution of NaOH (5 wt.%) at room temperature.

Subsequently, the supported Au-NRs were introduced into the sputtering chamber. 20 nm thick Pt, and Pd films were RF sputtered on the Au-NRs samples and the supporting substrate using pure targets (Pt and Pd (ESG Edelmetall GmbH, Rheinstetten, Germany)) under an approximate Argon partial pressure of 10^{-3} mbar. The sputtering power was set to 100 W for Pt, and 120 W for Pd at room temperature. The film thickness was monitored by a quartz crystal microbalance. The Sputtering of 20 nm Pt layer on a Silicon/Ti (2 nm)/Au substrate (the same substrate used to grow the Au-NRs) was introduced together with Au-NRs to the sputtering chamber.

The microstructure and morphology of the samples were characterized with a high-resolution scanning electron microscope (SEM Ultra Plus, ZEISS, Oberkochen, Germany) operating in the secondary (SE) and energy selective backscattered (ESB) electron modes. The SEM is also equipped with an energy dispersive X-ray spectroscopy (EDS) package (INCAx-act, Oxford Instruments, High Wycombe, UK). The structure was characterized by X-ray diffraction (XRD, X’Pert Pro diffractometer PANalytical, Eindhoven, Netherland) in grazing incidence diffraction mode with constant $\theta = 1°$ using monochromatic CuKα radiation with $\lambda = 1.5418$ Å. The device has a full width to half maximum resolution of 0.03°.

An electrochemical workstation (ZAHNER IM6e, Kronach,Germany) was used for linear sweep voltammetry (LSV) measurements from -0.8 V to 0.3 V. The electrochemical experiments were performed in 0.5 M H_2SO_4 solution with pH 0.36, using a three-electrode set-up with a Pt mesh and HydroFlex (reversible H_2 reference electrode) as counter and reference electrodes,

respectively. All potentials were referenced to the reversible hydrogen electrode (RHE). The current was normalized by the sample’s measured area. All the H_2SO_4 solutions were saturated with Forming gas (after the usual bubbling with nitrogen).

Computational methods

Ab initio calculations based on density functional theory implemented in Quantum ESPRESSO package were employed to simulate the adsorption of hydrogen on different (111)-oriented Au, Pt, Pd, AuPt, and AuPd sites [15]. Electron–ion interaction was described by projector augmented wave (PAW) potentials, while the exchange correlation was represented by generalized gradient approximation (GGA) in the Perdew–Burke–Ernzerhof (PBE) framework [16]. The plane wave basis cut-off energy was set to 400 eV. The structures were initially optimized by permitting the relaxation of atom positions by using the Broyden–Fletcher–Goldfarb–Shanno (BFGS) method. To attain high accuracy, the self-convergence-field convergence criterion was set to 10^{-6} eV.

(111)-oriented Au, Pt, Pd, AuPt, and AuPd surfaces were modelled with the 4x3x2 slab. Fig. 1a shows different hydrogen adsorption sites, namely top, bridge, fcc, and hcp for for Au, Pt, and Pd. For AuPt and AuPd, hydrogen adsorption was examined on the Au/Pt (Au/Pd) interface; in this case, new possible adsorption sites were as follows (Fig. 1b): bridge sites Au–Au and Pt–Pt (Pd–Pd). The hydrogen atom and the top layer of the slab were allowed to relax their atomic positions to attain the most stable surface-hydrogen distance $d_{S\text{-}H}$. Hydrogen adsorption energies were calculated on the basis of the usual definition eq. (4):

$$E_{ads} = E_{Metal-H} - E_H - E_{Metal} \qquad (4)$$

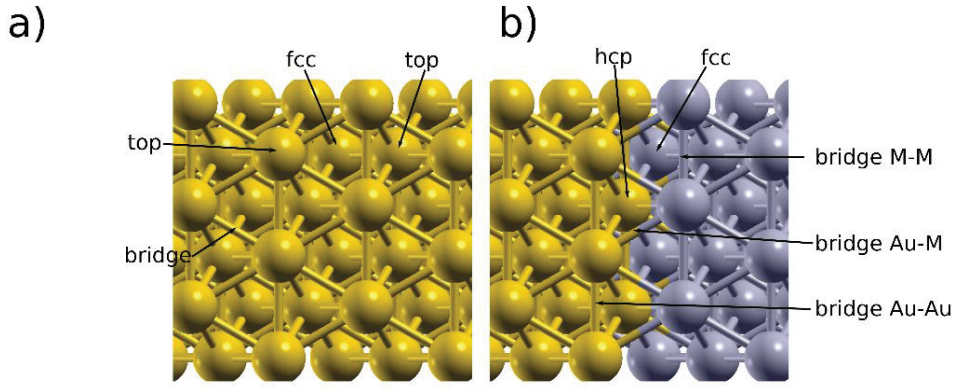

Fig. 1 Adsorption possible sites for: **a** Au, Pt, and Pd (111), **b** AuPd, AuPt (111).

Results and discussion

Structure and morphology

Here we focus on the Au/Pd(Pt) nanostructures. The structure and morphology of the monolithic nanostructures are shown in supplementary material (Fig. S1). A high-resolution back-scatter electron micrograph of electrodeposited Au/Pd 100/20 nm NRs is shown in Fig. 2a together with the corresponding EDS spectrum. Based on atomic number contrast, Pd (outlined, dark-contrast layer) forms caps of mean thickness of 20 nm on the Au-NR tips. There is no evidence that Pd is deposited on the lateral surface of the NRs, e.g. compare Fig. 2 a with supplementary material Fig. S1a where smooth lateral surfaces can be seen in both cases. In another experiment, and in order to explore the effect of the deposition method and Pd (Pt) morphology, 20 nm thick layers of Pd and Pt were also deposited on the Au-NRs (after template removal) via physical vapor deposition from pure Pd and Pt targets. In this case, Pd and Pt are deposited on the whole surface area of the Au-NRs. By comparing Fig. 2b,c,d to supplementary material Fig. S1a it is conspicuous from the rough morphology and the particulate structure of the NR surfaces that Pd and Pt distribute as NPs over the whole surface of the NRs.

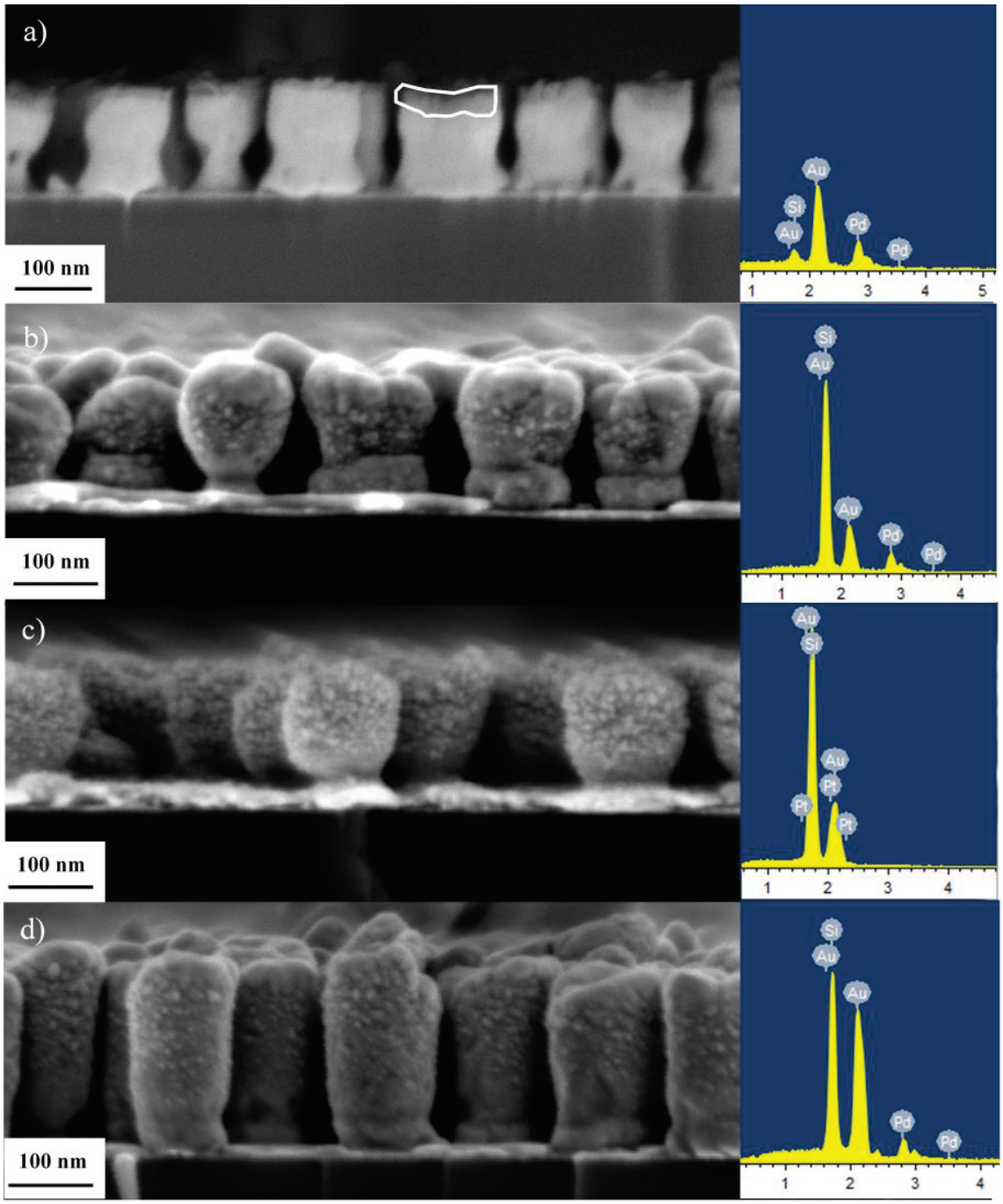

Fig. 2 SEM micrographs and EDS spectra of: **a** layered Au/Pd-NRs, **b** Au-NRs/Pd (Sputtered) 100/20 nm, **c** Au-NRs/Pt (Sputtered) 100/20 nm, , **d** Au-NRs/Pd (Sputtered) 200/20 nm; **a** shows a high-resolution back-scatter electron micrograph of the electrodeposited Pd-caps (delineated), approximately 20 nm thick on top of the Au-NRs; sputtering of Pd **b,d**, and Pt **c** on the Au-NRs leads to complete coverage of the Au-NRs surface area with Pd and Pt-NPs.

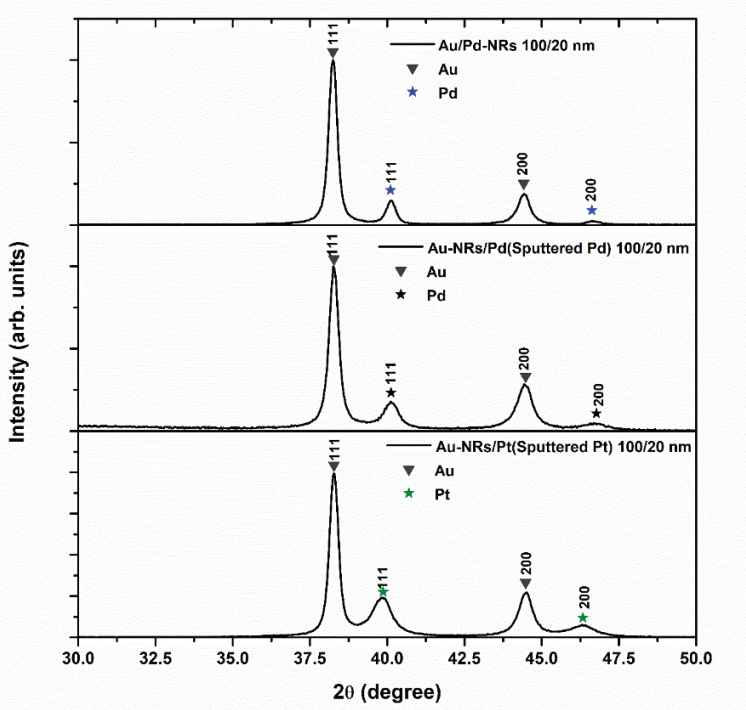

Fig. 3 XRD patterns in the range of 111 and 200 reflections in grazing incidence mode.

The XRD-patterns of the nanostructures investigated are shown in Fig. 3 with the usual reflections of Au, Pd and Pt. In the case of sputtered Pd and Pt, a broadening of the peaks can be observed, underscoring the nanoscale dimensions of the deposited materials. The mean particle size calculated using the Scherrer-Formula is 26 nm for electrodeposited Pd, 15 nm for sputtered Pd, and 12 nm for sputtered Pt. The ratios of the 200 to 111 peak areas are 0.19 for Pd and 0.37 for Pt delineating the predominance of the 111 orientation in both cases.

Electrochemical Investigations, HER

Linear sweep voltammetry (LSV) results as well as corresponding Tafel plots in 0.5 M H_2SO_4 electrolyte, pH = 0.36, are displayed in Fig. 4. The results clearly reflect that the electrocatalytic performance very much depends on the processing method of the catalyst.

Interestingly, the Au-NRs show a catalytic activity that is not far away from that of the sputtered Pt layer (approximately -1 mA/cm^2 difference at -0.4 V). That Au-nanostructures show HER activity has been documented in few reports. For instance, Kiani et al. report moderate catalytic activity of nanoporous Au-films [17], though at fairly higher overpotentials as the ones

observed in this work, and similar results to ours were obtained on Au-aerogel supported on graphitic carbon nitride, and Au-NPs by Kundu et al. [18].

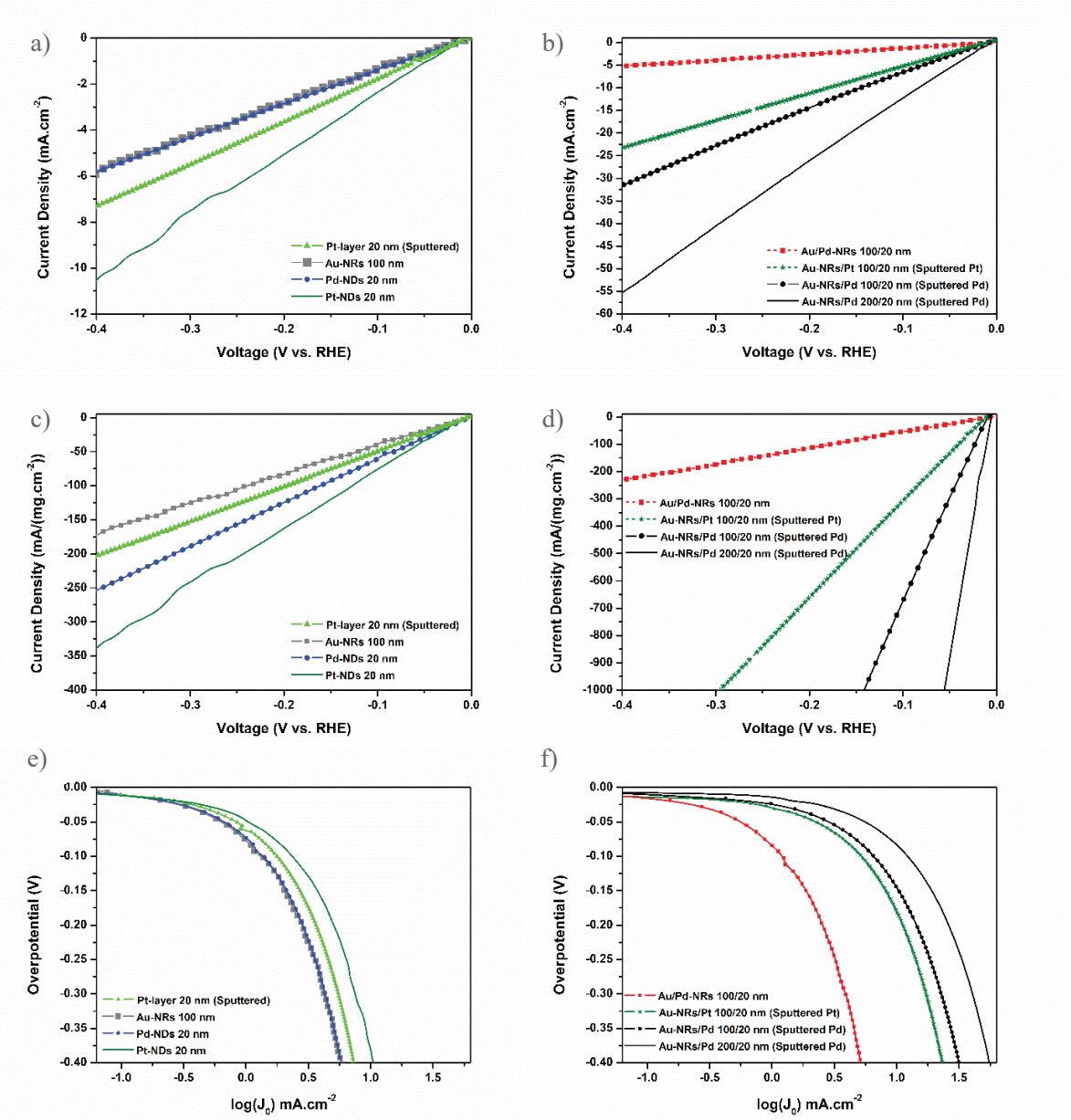

Fig. 4 IR corrected linear sweep voltammograms in 0.5 M H_2SO_4 of: **a,c** monolithic and **b,d** bilayer structures with electrodeposited Pt and Pd as well as sputtered Pt and Pd on Au-NRs. The current density is normalized by the geometric surface area, in **a,b** and by catalyst loading in **c,d**. Current density values at overpotentials of -0.4 and -0.1V are listed in Table 1 for the different catalyst nanostructures. **e,f** Tafel plots corresponding to the LSV curves. Sputtered Pd and Pt nanostructures are indicated. All others were electrodeposited. The current density in the Tafel plots refers to the geometric surface area. The Tafel slopes are listed in Table 1.

The electrodeposited layered and monolithic (except Au) nanostructures, including Pt, which is known to be the best catalyst under acidic conditions, all show moderate performance in the range from approximately -11 (for electrodeposited 20 nm Pt discs) to -7 mA/cm^2 at -0.4 V (see Table 1). It can also be seen that Au barely affects the performance of electrodeposited Pd.

A performance increase is obtained with sputtered Pt on Au-NRs in comparison to the sputtered Pt film which is understandably due to the NP-morphology and the increase in the surface area of Pt. However, sputtered Pd on Au-NRs is characterized by a substantially higher HER activity that is in terms of current density (at a constant overvoltage) is more than thrice that of comparable, electrodeposited Pd nanostructures, e.g. at -0.4 V (see Table 1). Using 200 nm Au-NRs supports improves the performance still more which is amenable to the higher surface area of Pt-NPs achieved with longer Au-NRs. Most surprising is the behavior of sputtered Pt on Au-NRs (Au/Pt 100/20 nm) which is characterized by a substantially lower current density at a voltage of -0.1 V vs. RHE than the sputtered Pd on Au-NRs structures. Because it is known that Pd-NPs on carbon (Pd/C) have a substantially lower activity than Pt/C [19], it appears that combining Pd-NPs are with Au in an Au/Pd bimetallic nanostructure results in a performance boosting of the catalytic activity that even overrides that of a similar Pt/Au bimetallic structure. That AuPd bimetallic nanocrystals are more efficient a catalyst than Pd/C has been also reported by Feng et al. [20], although their results show that Pt/C is a slightly better catalyst. From our results we can surmise that the nature of electronic interactions at the Pd (Pt)/Au interface must play a key role in controlling catalyst performance (see below for discussion).

The Tafel plots are displayed in Fig. 4e,f. For all structures at least two different slopes can be distinguished; at overpotentials higher than -0.1V (versus RHE)) the current density exponentially depends on the overpotential. This behavior has been reported by Conway and Bai [21], and rationalized in terms of the hydrogen surface coverage’s dependence on the overpotential for the Volmer-Heyrovsky mechanisms [21,22].

Table 1 Catalyst loading, current density, Tafel slopes, and exchange current density of different structures.

	Catalyst loading (mg/cm^2)	Current Density (mA/cm^2)		Current Density ($mA/(mg.cm^{-2})$)		Tafel Slope (mV/dec)	Exchange Current Density $\log(J_0$ (mA/cm^2))
		At -0.1 V	At -0.4 V	At -0.1 V	At -0.4 V		
Pt-layer 20 nm (Sputtered)	0.063	-1.80	-7.34	-49.3	-203.4	87	-0.65
Au-NRs 100 nm	0.044	-1.30	-5.83	-39.0	-171.5	119	-0.64
Pt-NDs 20 nm	0.041	-2.35	-10.50	-75.5	-337.6	98	-0.49
Pd-NDs 20 nm	0.031	-1.40	-5.79	-59.9	-253.7	103	-0.66
Au/Pd NRs 100/20 nm	0.029	-1.20	-5.22	-51.0	-229.5	93	-0.79
Au-NRs/Pt (Sputtered) 100/20 nm	0.022	-5.20	-23.30	-313.5	-1370.5	56	-0.63
Au-NRs/Pd (Sputtered) 100/20 nm	0.013	-6.60	-31.55	-480.0	-3263.1	53	-0.42
Au-NRs/Pd (Sputtered) 200/20 nm	0.008	-12.3	-55.12	-1939.0	-8731.7	52	-0.22

The slopes calculated at low overpotentials are listed in Table 1; they range from values of 119 to 52 mV/dec that probably reflect different, structure dependent HER mechanisms (see below

for discussion). The Au-NRs show the highest slope (119 mV/dec) followed by the slopes of the electrodeposited Pd (103 mV/dec), layered Au/Pd (98 mV/dec) nanostructures, and sputtered Pt layer (87 mV/dec). The electrodeposited Pt-nanodiscs show an intermediate value of 98 mV/dec that is higher than what is known for carbon supported Pt-NPs [23], but lower than the values reported for polycrystalline Pt [24,25]. For the Au/ sputtered Pt and Pd nanostructures the values decrease to roughly 56 mV/dec for Au/Pt and 53 mV/dec for Au/Pd, although the lowest value is shown by Pd sputtered on the longer, 200 nm Au-NRs.

From the Tafel slopes above, we can definitely state that the operating HER mechanisms are dependent on structure and material’s morphology. Particularly, the Au/sputtered Pd nanostructures seem to stand out both through highest performance and lowest Tafel slope.

Chronoamperometric measurements were conducted in 0.5 M H_2SO_4 at a fixed voltage of -0.4 V for 120 minutes to test the long-term property stability (Fig. 5). It can be seen that the activity of both Au-NRs/Pd and Au-NRs/Pt keep increasing for some time before it saturates probably because of activation and the full coverage of all surface sites. As expected, Au-NRs/Pd saturates at a higher (absolute value) than Au-NRs/Pt. Further, Au-NRs/Pd saturates faster than Au-NRs/Pt which might be attributed to fast diffusion of and coverage with hydrogen because of less potential barriers. We should now shed some light on these observations via DFT calculations, particularly considering hydrogen adsorption energies on different sites of the structures.

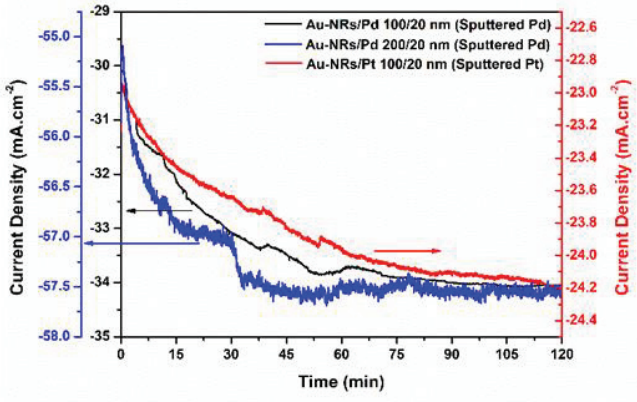

Fig. 5 Chronoamperometric curves of Au-NRs/Pt 100/20 nm, Au-NRs/Pd 100/20 nm and Au-NRs/Pd 200/20 nm in 0.5 M H_2SO_4 at -0.4 V for 120 minutes.

DFT calculations

Table 2 Adsorption energies (E_{ads}), and hydrogen surface distance (d_{H-S}) for Au, Pt, and Pd surfaces.

	E_{ads} (eV) / d_{H-S} (A)			
	top	**bridge**	**fcc**	**hcp**
Au	-1.57 / 1.60	-1.75 / 0.99	-1.81 / 0.81	-1.62 / 1.08
Pt	-2.76 / 1.57	-2.85 / 1.07	-2.87 / 0.94	-2.84 / 0.95
Pd	-2.28 / 1.57	-2.78 / 1.05	-2.91 / 0.87	-2.87 / 0.88

Table 2 summarizes the calculated H adsorption energies on different sites of monolithic, (111)-oriented Au, Pt, and Pd surfaces. Obviously, the hydrogen adsorption energy is material and site dependent, with Au (111) being characterized on all sites by the lowest hydrogen adsorption energies. Pt and Pd exhibit competitive site stability, with the strongest hydrogen adsorption on fcc Pd(111). The results obtained are in agreement with those reported by Ferrin et al. [26]. As different events occur in the HER process, including hydrogen adsorption, hydrogen diffusion, and H_2 formation, the low stability of Au sites for hydrogen adsorption might point to the hydronium ions discharge on Au as the rate limiting step (Volmer reaction) which also explains the high Tafel slope obtained. Comparing the adsorption energy on the different sites, it can be seen that the Pt sites are characterized by close values (variance of 0.11 eV) than those of Pd (variance of 0.63 eV). Since the capacity of hydrogen diffusion over the catalyst surface facilitates easy surface coverage with hydrogen as well as recombination of the adsorbed hydrogen, and according to the diffusion mechanisms explained by Watson et al. [27], the diffusion of hydrogen over the surface is progressively more rapid on Pt than over Pd. In the case of Pd, the diffusion pathway is through the top site; hence, diffusion over the Pd surface is hampered as H adsorbates need to go through the top site, leading to a critical energy barrier compared to Pt.

Table 3 Adsorption energies (E_{ads}), and hydrogen surface distance (d_{H-S}) for AuPt, and AuPd surfaces. M=Pt, Pd

	E_{ads} (eV) / d_{H-S} (A)						
	top		**bridge**			**fcc**	**hcp**
	Au	**M**	**Au-Au**	**Au-M**	**M-M**	**Au2M**	**2AuM**
AuPt	-2.20/ 1.59	-2.88/ 1.57	-2.19/ 1.36	-2.23/ 1.49	-2.52/ 1.12	-2.10/ 1.60	-2.34/1.33
AuPd	-2.37/ 1.60	-2.51/ 1.56	-2.29/ 1.41	-2.25/ 1.65	-2.48/ 1.11	-2.28/ 1.50	-2.29/ 1.39

Bimetallic nanocatalysts behave differently, as depicted in the experimental results above. To understand these behaviors, two (111) layers of Au and M (Pt, Pd) were placed in lateral contact (Fig. 1b) and left for the relaxation of atomic positions.

Additional adsorption sites ensue from this procedure: two top Au and M (Pt, Pd) sites, three bridge Au–Au, Au–M, and M–M sites, and several hollow sites. Since the sputtered layer covers the whole Au-NR surface leading a core-shell like structure, the relevant sites for H-adsorption should be Au-M and M-M. Table 3 summarizes the adsorption energies and the distance from the surface for different sites of (111)-oriented AuPd and AuPt surfaces. The first observation is that top Au and bridge Au–Au become more stable for both surfaces compared to the bare Au surface (difference of >0.6 eV), but this is rather secondary to our context, since Au is buried under the Pt/Pd metal layer. Compared to bare Pt and Pd, the top sites become most favorable sites for hydrogen adsorption. Comparison of the present results to others, Hu et al. also similarly reported that top-site adsorption of hydrogen on platinum–gold nanoparticles are more stable for all Pt content of AuPt–NP than the top site of pure Pt–NP [28]. The variance in adsorption energies between different sites is 0.26 eV for AuPd and 0.78 eV for AuPt. The hydrogen diffusion ability over the surfaces becomes easier for the Pd-containing surface than for the Pt-containing one, leading to a high hydrogen coverage of the surface for AuPd and helping to boost the HER activity as shown in the experimental results.

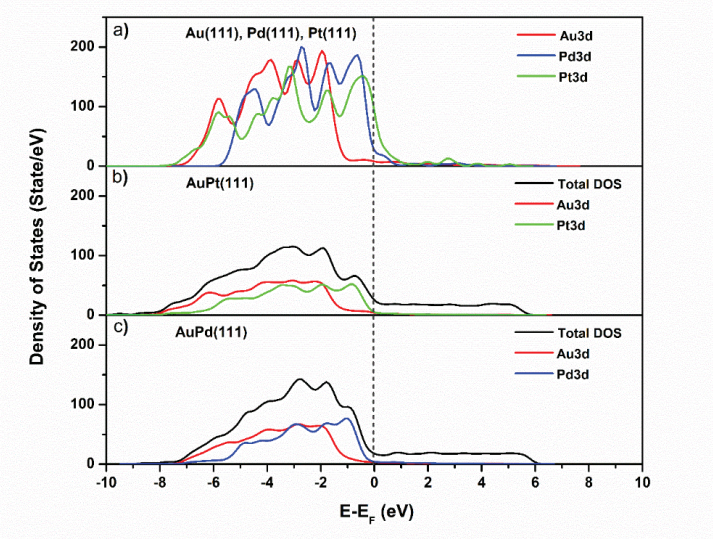

Fig. 6 Orbital electronic density of states for 111-oriented **a** Au, Pt, Pd, **b** AuPt, **c** AuPd. E_F denotes Fermi level. Notice the change in the occupied states distribution and intensities for Pt in AuPt, and Pd in AuPd.

The different behaviors of AuPd and AuPt may be understood, considering the density of states. Fig. 6 shows the density of states calculated for the pure metals and the AuPt and AuPd surfaces. The results are in qualitative agreement with the results published so far on Au, Pt, and

Pd for the pure metals [29,30]. The d-states occupation of the metals in AuPt and AuPd largely differs from those of the pure metals, both in intensity and energy range (compare Fig. 6a to Fig. 6b, c).

The interaction between hydrogen and the metal is directly proportional to the distance between the d-band center and the Fermi level of the metal [31-33]. The interaction energy can be described by eq. (5) [31-33]:

$$\Delta\varepsilon \sim \frac{V^2}{|\varepsilon_d - \varepsilon_H|} \qquad (5)$$

where V is the coupling matrix, assumed to be constant for similar configurations. $|\varepsilon_d\text{-}\varepsilon_H|$ is the d-band shift which controls the interaction energy and consequently the bond formation. In the monolithic metals, the d-band centers calculated are -2.82 eV, -2.33 eV, and -2.62 for Pt, Pd and Au surfaces, respectively. In the case of AuPt and AuPd interfaces, the d-band center gradually shifts to higher energies for Pt and lower energies for Pd toward the Fermi level (-2.77 eV for Pt, -2.96 eV for Au in AuPt, and -2.51 eV for Pd, -2.58 eV for Au in AuPd). When Au is alloyed with Pt, the charges are directly transferred from the Pt d-band to fill the empty states of the Au d-band, leading to a shift of the d-band center to lower energies for Au and higher energies for Pt. This result is in agreement with those reported by Mott et al. [29] who also observed a linear Pt d-band center shift with increasing Au concentration in AuPt-NPs.

In the case of AuPd, Lee et al. [30] investigated the redistribution of charges in an AuPd alloy. They concluded that Au loses d-charges and gains sp charges together with the depletion of Pd sp charges and the gain of d charges. This charge redistribution leads to a small net charge transfer from Pd to Au. In this case, there is a transfer of charges from Pd to Au, but this is accompanied with sp-d hybridization which compensates the charges by injecting them into the Au sp band. This explains the charges added into the Pd d-band (d-band center shift) with the preservation of the charge transfer predicted by the difference in electronegativity (see Fig. 7 for a schematic description of the d-band shift).

Combining the calculated adsorption energies with the d-band center model, the introduction of Au into the matrix should moderately favor the adsorption of H on Pt ($|\varepsilon_d\text{-}\varepsilon_H|$ decreases) while slightly decreasing adsorption affinity on Pd ($|\varepsilon_d\text{-}\varepsilon_H|$ increases). In all cases, however, full coverage of the metal surface (Pt, Pd) with hydrogen is expected, but AuPd should be a better catalyst owing to the lower hydrogen adsorption energy and the lower d-band center

shift. This result is principally in line with the results of Kibler et al. [34], who investigated pseudomorphic Pd monolayers on Au(111), and explained their findings from the point of view of the ligand theory (change in the interatomic distance of the Pd monolayer, consequently altering the d-band center [33]).

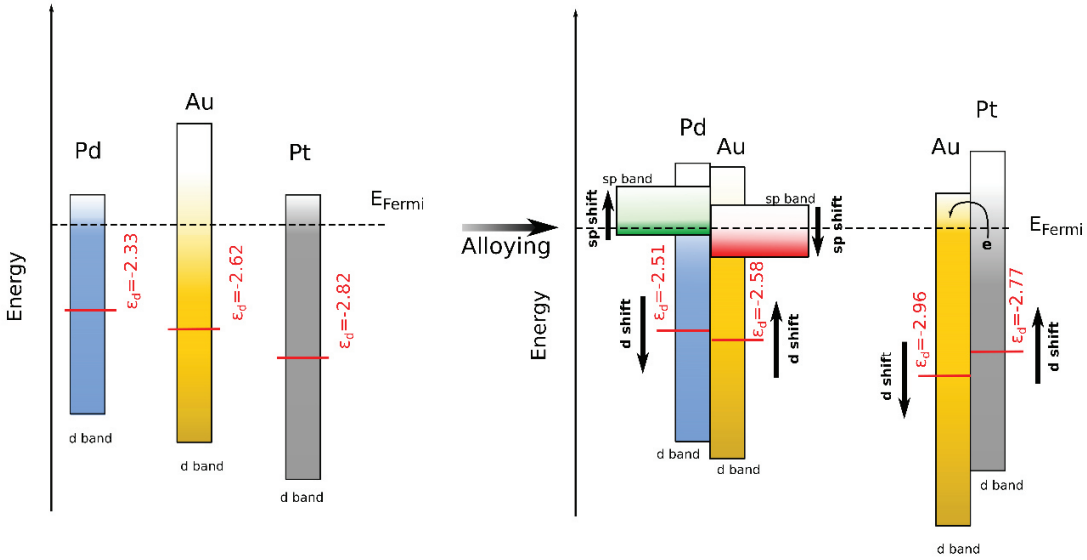

Fig. 7 Schematic representation of the d-band shift in Au, Pt, Pd, AuPt and AuPd. ε_d is the d-band center. A direct charge transfer from Pt to Au results in a d-band shift to higher energies for Pt in AuPt; the charge transfer mechanisms in AuPd is more complex, and involve the sp-band as mediator for the charge redistribution in Au and Pd.

Discussion and conclusions

The experimental results depicted above reveal that while the monolithic nanostructures all show a moderate HER activity, including a sputtered Pt-layer and electrodeposited Pt-nanodiscs, a drastic increase in performance occurs when thin layers of Pt and Pd are sputtered on Au-NRs allowing for a large interfacial area between the active metal and the support to be achieved. The structure thus obtained is akin to Au-core-Pt (Pd)-shell. This unambiguously suggest that interfacial electronic interactions in bimetallic Au/Pt and Au/Pd are of paramount importance in controlling electrocatalytic activity. Comparing the bimetallic Au-NRs/sputtered Pd and Pt catalysts, it is readily seen that Au/Pd is far more active than Au/Pt which must be amenable to specific changes in the density of state of Pd and d-band center shift as discussed above, which endows it with higher performance. This finding is particularly interesting, since Pt (e.g. Pt/carbon) is known to a better catalyst than Pd (e.g. Pd/C) [19,20,34].

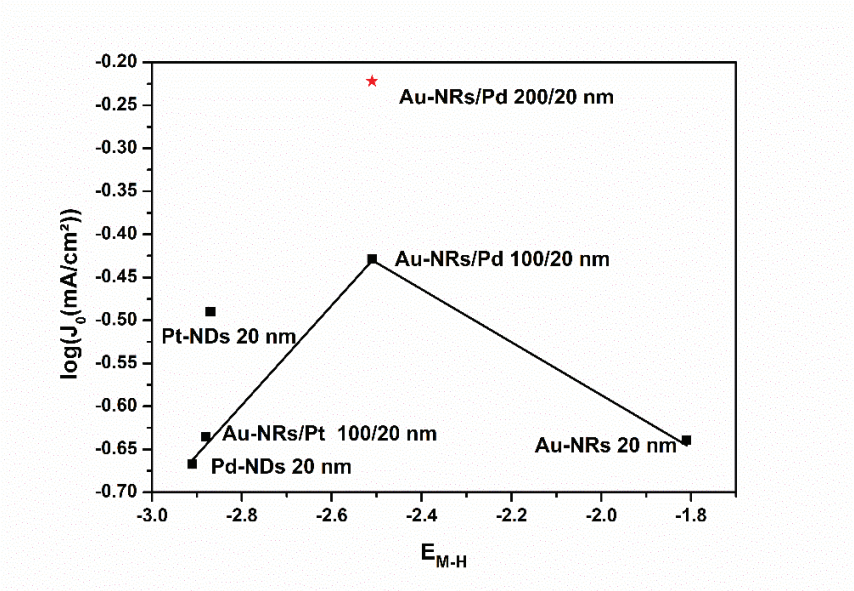

Fig. 8 Exchange current density, $\log(J_0)$, as a function of the calculated hydrogen adsorption energies. Only the stable adsorption sites were considered for each structure. Au-NRs/Pd is located on the top of the volcano; the Au-NRs/Pt lies below Pt-NDs indicating a change in the HER mechanism. For the sake of direct comparison similar nanostructures are considered, e.g. Au-NRs/Pt 100/20 nm and Au-NRs/Pd 100/20.

Fig. 8 shows a tentative volcano plot of the hydrogen evolution reaction that relates the exchange current density to the calculated adsorption energies. As mentioned above, Pt is known to be located at the top of the volcano with the highest activity and a moderate adsorption energy, which is strong enough to activate the HER, and prevent the formation of stable intermediates that suppress the HER. The mechanisms of HER for Pt and Pd are reported to obey the Volmer-Tafel mechanisms [31,32], although this has been questioned by Durst et al. [19] with respect to our results, and taking into account the Tafel slopes obtained, as well as the calculated adsorption energies of H on Pt, Pd, AuPd and AuPt, there is rather a trend towards a parallel Volmer-Heyrovsky mechanism with a fast Volmer step. The Au effect on Pd indicates that electronic interactions at the interface between Au and Pd lead to a suitable change in the adsorption energy of H on all Pd sites, and this translates in a fast Volmer-Heyrovsky mechanism. That the interfacial interactions between Au and Pd play a paramount role in controlling performance can be further demonstrated on Au-NR/Pd 200/20 nm where an increase in the interfacial area between Au and Pd results in a higher activity (without change in the HER mechanism).

In conclusion, Au NRs, Au/Pd NRs, and Pt and Pd nanodiscs of 100, 100/20, and 20 nm, respectively, were processed using electrodeposition in AAO template film on Si. Subsequently,

the 100-nm Au NRs were used as supports for sputtering 20 nm thick Pt and Pd thin layers. Microscopic analysis shows that sputtering of Pt and Pd layers lead to nanoparticle formation over the entire surface of the nanorods, resulting in a high interfacial area between Au and the sputtered metals. The nanostructures were evaluated as electrocatalysts for the hydrogen evolution reaction via linear sweep voltammetry and Tafel plots. While the electrodeposited nanostructures all show a rather moderate performance, the bimetallic Au-NR/sputtered Pt and Pd are characterized by a higher activity. Interestingly, and most surprisingly, the sputtered Pd on Au NR support outperforms sputtered Pt (on Au-NR). This unusual result-Pt is known to be best catalyst for HER under acidic conditions- is thought to be a direct consequence of the specific electronic interactions between Pd and Au that lead to a more suitable hydrogen adsorption energy on the different Pd sites, and consequently a faster HER mechanism. That the Au-Pd electronic interactions at the Au-Pd interface are beneficial to HER is demonstrated using sputtered Pd on 200 nm Au-NR which lead to a doubling of the current density (at -0.1 V) in comparison to the shorter NRs. Based on the Tafel slopes, the Heyrovsky-Volmer mechanism is suggested as the dominant mechanism. The results are corroborated by DFT calculations which show that interfacial Pt/Pd–Au electronic interactions are accompanied with charge transfer and redistribution in the d-band of Au, Pt, and Pd. This translates in a d-band shift which in turn directly affects the hydrogen adsorption energy. In particular it is shown that hydrogen adsorbs on all Pd-sites with marginal difference in the adsorption energy thus leading to better surface coverage and most importantly to barrier-free surface diffusion and recombination. Finally, based on the results obtained a tentative volcano plot is proposed.

Conflicts of interest

There are no conflicts to declare.

Acknowledgements

This work has no financial support.

References

1. O. H. Hohmeyer and S. Bohm, Trends toward 100% renewable electricity supply in Germany and Europe: a paradigm shift in energy policies. WIREs Energy Environ. **4**, 74-97 (2015). https://doi.org/10.1002/wene.128
2. I. Dincer and C. Acar, Innovation in hydrogen production. Int. J. Hydrog. Energy **42**, 14843-14864 (2017). https://doi.org/10.1016/j.ijhydene.2017.04.107
3. Fastmarkets, https://www.metalbulletin.com/lithium-prices-update; 2020 [accessed June 2020]
4. B.E. Conway and B. V. Tilak, Interfacial processes involving electrocatalytic evolution and oxidation of H_2, and the role of chemisorbed H. Electrochimica Acta **47**, 3571-3594 (2002). https://doi.org/10.1016/S0013-4686(02)00329-8
5. J. O. Bockris and B. E. Conway, Modern Aspects of Electrochemistry, Butter-worths Sci Publications 1954.
6. D. D. Eley, H. Pines and P. B. Weisz, Advance in Catalysis, Academic Press Inc. New York, 1992.
7. M. Bhardwaj and R. Balasubramaniam, Uncoupled non-linear equations method for determining kinetic parameters in case of hydrogen evolution reaction following Volmer–Heyrovsky–Tafel mechanism and Volmer–Heyrovsky mechanism. Int. J. Hydrog. Energy **33**, 2178-2188 (2008). https://doi.org/10.1016/j.ijhydene.2008.02.027
8. A. Eftikhari, Electrocatalysts for hydrogen evolution reaction. Int. J. Hydrog. Energy **42**, 11053-11077 (2017). https://doi.org/10.1016/j.ijhydene.2017.02.125
9. J. R. McKone, E. L. Warren, M. J. Bierman, S. W. Boettcher, B. S. Brunschwig, N. S. Lewis and H. B. Gray, Evaluation of Pt, Ni, and Ni–Mo electrocatalysts for hydrogen evolution on crystalline Si electrodes. Energy Environ. Sci. **4**, 3573-3583 (2011). https://doi.org/10.1039/C1EE01488A
10. D. Voiry, M. Salehi, R. Silva, T. Fujita, M. Chen, T. Asefa, V. B. Shenoy, G. Eda and M. Chhowalla, Conducting MoS_2 Nanosheets as Catalysts for Hydrogen Evolution Reaction. Nano Lett. **13**, 6222-6227 (2013). https://doi.org/10.1021/nl403661s
11. Y. Zheng, Y. Jiao, Y. Zhu, L. H. Li, Y. Han, Y. Chen, A. Du, M. Jaroniec and S. Z. Qiao, Hydrogen evolution by a metal-free electrocatalyst. Nat. Commun. **5**, 3783 (2014). https://doi.org/10.1038/ncomms4783

12. A. Laghrissi and M. Es-Souni, Layered Au-Pd-Au nanorod catalysts: Pd-layer thickness effects on catalyst performance. Int. J. Hydrog. Energy **44**, 14918-14926 (2019). https://doi.org/10.1016/j.ijhydene.2019.04.105
13. M. Es-Souni and S. Habouti, Ordered nanomaterial thin films via supported anodized alumina templates. Front. Mater. **1**, 19 (2014). https://doi.org/10.3389/fmats.2014.00019
14. N. Berger and M. Es-Souni, Understanding and shaping the morphology of the barrier layer of supported porous anodized alumina on gold underlayer. Langmuir **32**, 6985-6990 (2016). https://doi.org/10.1021/acs.langmuir.6b01732
15. P. Giannozzi, S. Baroni, N. Bonini, M. Calandra, R. Car, C. Cavazzoni, D. Ceresoli, G. L. Chiarotti, M. Cococcioni, I. Dabo, A. Dal Corso, S. De Gironcoli, S. Fabris, G. Fratesi, R. Gebauer, U. Gerstmann, C. Gougoussis, A. Kokalj, M. Lazzeri, L. Martin-Samos, N. Marzari, F. Mauri, R. Mazzarello, S. Paolini, A. Pasquarello, L. Paulatto, C. Sbraccia, S. Scandolo, G. Sclauzero, A. P. Seitsonen, A. Smogunov, P. Umari and R. M. Wentzcovitch, QUANTUM ESPRESSO: a modular and open-source software project for quantum simulations of materials. J. Phys. Condens. Matter. **21**, 395502 (2009). https://doi.org/10.1088/0953-8984/21/39/395502
16. J. P. Perdew, K. Burke and M. Ernzerhof, Generalized gradient approximation made simple. Phys. Rev. Lett. **77**, 3865e8 (1996). https://doi.org/10.1103/PhysRevLett.77.3865
17. A. Kiani and S. Hatami, Fabrication of platinum coated nanoporous gold film electrode: A nanostructured ultra low-platinum loading electrocatalyst for hydrogen evolution reaction. Int. J. Hydrog. Energy **35**, 5202-5209 (2010). https://doi.org/10.1016/j.ijhydene.2010.03.014
18. M. K. Kundu, T. Bhowmik and S. Barman, Gold aerogel supported on graphitic carbon nitride: an efficient electrocatalyst for oxygen reduction reaction and hydrogen evolution reaction. J. Mater. Chem. A **3**, 23120-23135 (2015). https://doi.org/10.1039/C5TA06740E
19. J. Durst, A. Siebel, C. Simon, F. Hasche, J. Herranz and H. A. Gasteiger, New insights into the electrochemical hydrogen oxidation and evolution reaction mechanism. Energy Environ. Sci. **7**, 2255-2260 (2014). https://doi.org/10.1039/C4EE00440J
20. J. J. Feng, L. X. Chen, P. Song, X. Wu, A. J. Wang and J. Yuan, Bimetallic AuPd nanoclusters supported on graphitic carbon nitride: One-pot synthesis and enhanced electrocatalysis for oxygen reduction and hydrogen evolution. Int. J. Hydrog. Energy **41**, 8839-88469 (2016). https://doi.org/10.1016/j.ijhydene.2016.03.108

21. B. E. Conway and L. Bai, Determination of adsorption of OPD H in the cathodic hydrogen evolution reaction at Pt in relation to electrocatalysis. J. Electroanal. Chem. Interf. Electrochem. **198**, 149-175 (1986). https://doi.org/10.1016/0022-0728(86)90033-1
22. T. Shinagawa, A. T. Garcia-Esparza and K. Takanabe, Insight on Tafel slopes from a microkinetic analysis of aqueous electrocatalysis for energy conversion. Sci. Rep. **5**, 13801 (2015). https://doi.org/10.1038/srep13801
23. Y. Y. Ma, C. X. Wu, X. J. Feng, H. Q. Tan, L. K. Yan, Y. Liu, Z. H. Kang, E. B. Wang and Y. G. Li, Highly efficient hydrogen evolution from seawater by a low-cost and stable CoMoP@C electrocatalyst superior to Pt/C. Energy Environ. Sci. **10**,788-798 (2017). https://doi.org/10.1039/C6EE03768B
24. G. Couturier and D. W. Kirk, Electrocatalysis of the hydrogen oxidation and of the oxygen reduction reaction on Pt and some alloys in alkaline medium. Electrochim. Acta **32**, 995-1005 (1987). https://doi.org/10.1016/0013-4686(87)90024-7
25. N. M. Markovic, B. N. Grgur and P. N. Ross, Temperature-dependent hydrogen electrochemistry on platinum low-index single-crystal surfaces in acidic solutions. J. Phys. Chem. **101**, 5405-5413 (1997). https://doi.org/10.1021/jp970930d
26. P. Ferrin, S. Kandoi, A. U. Nilekar and M. Mavrikakis, Hydrogen adsorption, absorption and diffusion on and in transition metal surfaces: A DFT study. Surf. Sci. **606**, 679-689 (2012). https://doi.org/10.1016/j.susc.2011.12.017
27. G. Q. Watson, R. P. K. Wells, D. J. Willock and G. J. Hutchings, A Comparison of the Adsorption and Diffusion of Hydrogen on the {111} Surfaces of Ni, Pd, and Pt from density functional theory calculations. J. Phys. Chem. B **105**, 4889-4894 (2001). https://doi.org/10.1021/jp002864c
28. M. Hu, D. P. Linder, M. G. Nardelli and A. Striolo, Hydrogen adsorption on Platinum−Gold bimetallic nanoparticles: A density functional theory study J. Phys. Chem. C **117**, 15050-15060 (2013). https://doi.org/10.1021/jp3126285
29. D. Mott, J. Luo, A. Smith, P. N. Njoki, L. Wang and C. J. Zhong, Nanocrystal and surface alloy properties of bimetallic Gold-Platinum nanoparticles. Nano Express **2**,12-16 (2007). https://doi.org/ 0.1007/s11671-006-9022-8
30. Y. S. Lee, A. Jeon, Y. D. Chung, K. Y. Lim, C. N. Whang and S. J. Oh, Charge redistribution and electronic behavior in Pd-Au alloys. J. Korean Phys. Soc. **37**,451 (2000).

31. M. Lischka and A. Groß, Hydrogen adsorption on an open metal surface: H_2/Pd(210). Phys. Rev. B **65**, 075420 (2002). https://doi.org/10.1103/PhysRevB.65.075420
32. B. Hammer and J. K. Norskov, Why gold is the noblest of all the metals. Nature **376**, 238-240 (1995). https://doi.org/10.1038/376238a0
33. B. Hammer and J. K. Norskov, Electronic factors determining the reactivity of metal surfaces. Surf. Sci. **343**, 211-220 (1995). https://doi.org/10.1016/0039-6028(96)80007-0
34. L. A. Kibler, A. M. El-Aziz, R. Hoyer and D. M. Kolb, Tuning Reaction Rates by Lateral Strain in a Palladium Monolayer. Angew. Chem. Int. Ed. **44**, 2080 -2084 (2005). https://doi.org/10.1002/anie.200462127

Supplementary materials

Au-nanorods supporting Pd and Pt nanocatalysts for the hydrogen evolution reaction: Pd is revealed a better catalyst than Pt

Institute for Materials & Surface Technology, University of Applied Sciences, Grenzstrasse 3, D-24149 Kiel, Germany.

*Correspondence: mohammed.es-souni@fh-kiel.de

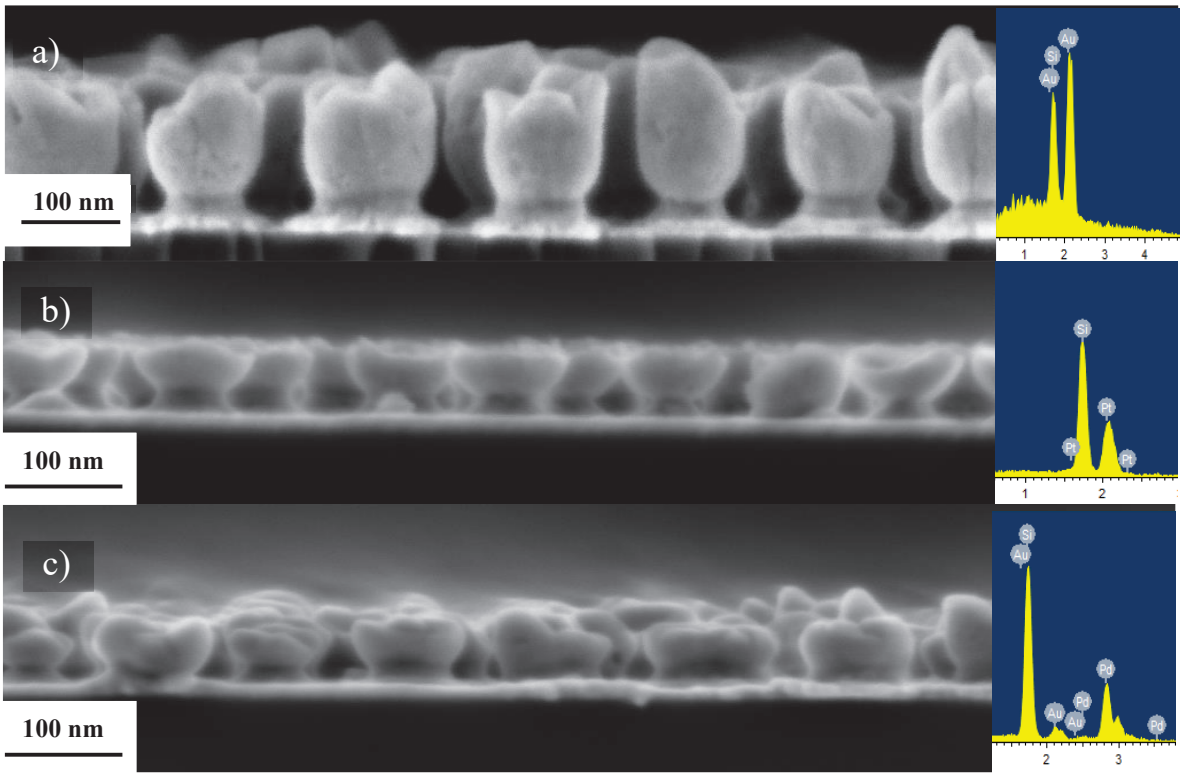

Fig. S1 SEM micrographs and EDS spectrum for monolithic structures: **a** Au-NRs; **b** Pt-NDs; **c** Pd-NDs.

Conclusions

In this thesis, the effects of nanostructure morphology and chemistry on the electrocatalytic activity and mechanisms of the platinum-group metal for fuel cell applications and hydrogen evolution reaction (HER) were examined. Because Pt and Pd are expensive and scarce, main emphasis was placed on strategies to reduce their load in the catalyst while boosting performance. Alloying and nanostructure design proved to be most promising to achieve this goal. 0D and 1D nanostructures were explored. The former was processed directly on substrate using a simple sonochemistry method while 1D nanostructures were grown in supported porous aluminum oxide templates via electrodeposition. By adopting suitable electrodeposition parameters, nanorods, nanotubes and layered structures could be obtained. Further, PVD deposition of Pd and Pt-NPs on Au-NRs was also explored for HER in order to investigate the effects of different processing methods on the electrocatalytic activity.

Bimetallic noble-metal nanoparticles (NPs) of controlled compositions were prepared by sonochemical deposition from an aqueous solution precursor onto nanocarbon and a TiN substrate in the absence of a surfactant. This facile deposition method was conducted using a laboratory ultrasonic cleaner. The formation mechanisms of NPs were investigated. The formation of reducing radicals in the cavitation on nanocarbon and TiN substrates was suggested to be responsible for the formation of noble metal and nanoalloy NPs. The synthesized AuPd NPs exhibited high activity for formic acid oxidation. Their high activity directly depends on the NP size and the ligand effects between Au and Pd.

In addition, the electrocatalytic activity of 1D palladium and Au/Pd/Au layered nanostructures for the electrooxidation of formic acid was investigated. The focus was to examine the gold interfacial effect on the electrocatalytic behavior of palladium for different Pd-layer thicknesses. For this purpose, the layered Au/Pd/Au structures were sequentially electrochemically deposited into AAO templates, followed by the removal of the AAO template to expose the structures. The layered structures were compared to monolithic Pd nanorods in terms of their activity for formic acid electrooxidation. Cyclic voltammetry behavior revealed a shift of the PdO reduction peak to more noble voltages with decreasing palladium thickness, indicative of the formation of AuPd near-interface alloys. The electrocatalytic behavior was strongly dependent on the Pd thickness with a higher activity being recorded for thinner Pd-layers. Overall, however, the

layered structures exhibited a higher activity than monolithic Pd-NRs, and a direct path for formic acid oxidation. Moreover, as the Pd layer thickness became extremely small, e.g., 15 nm, not only the electrocatalytic performance drastically increased but remained more stable over a long period in comparison to monolithic Pd-NRs. These results are interpreted in terms of the chemical interaction between Pd and Au at the interface. DFT calculation was employed to rationalize the results using a 1Au:1Pd alloy to model the interfacial Pd atoms. Modeling results suggested that the higher electrocatalytic performance of NRs is controlled by the impact of Au atoms for the oxidation of adsorbed CO and not by CO adsorption as the adsorption energy is more stable for AuPd than for Pd.

With the aim of boosting the electrocatalytic activity of Pt for the electrooxidation of methanol, 1D nanostructures were synthesized. The active surface area was considerably increased by using porous nanotubes, and the effect of Pd on Pt was investigated with a wide range of Pt concentrations of PtPd 1D nanostructures (from 5 to 100 at%). A non-ionic surfactant and negative electrodeposition voltage permitted the processing of porous nanotubes. The active chemical surface area and activity of the structures revealed a strong dependence on the Pt concentration. With the decrease in the Pt concentration to 10%, the ECSA increased. PtPd -NTs were characterized by a higher performance for the electrooxidation of methanol than monolithic Pt-NT and plain PtPd-NRs of similar chemistry. The maximum current density was 835 A/g Pt in 0.5 M H_2SO_4 and 932 A/g Pt in 0.1M $HClO_4$ for porous Pd10Pt alloy NTs. The NT structure, mesoporosity, lattice contraction, and charge transfer from Pd to Pt possibly contributed to these results. DFT calculations revealed that the charge transfer from Pd to Pt leads to the change in the preferential CO adsorption site to Pd and reduction in the CO poisoning.

Owing to the importance of hydrogen production from water electrolysis as a promising energy storage process from renewables, and based on previous observations of promising HER activity of layered Au/Pd-NRs, HER was investigated first for Pd electrodeposited on Au-NRs, and subsequently on sputtered Pd on exposed Au-NRs in order to increase the interfacial interactions between Pd and Au. For the sake of comparison, the same processes were used for Pt which is known the best catalyst for HER. Compared to the electrodeposited ones, sputtered Pt and Pd exhibited a morphological difference. The sputtered structures were formed from NPs distributed over the support surface, leading to core–shell like structures. Compared to the electrodeposited ones, the sputtered structures exhibited a substantially higher activity. The mechanisms of HER

were investigated using Tafel-plots with the Volmer-Heyrovsky being the likely operating mechanism for all structures. The most salient result, however, was the higher performance recorded for sputtered Pd/Au-NRs in comparison to sputtered Pt/Au-NRs (and electrodeposited Pt). This suggested that specific electronic interactions at the interface between Pd and Au that are different from those between Pt and Au were responsible for the higher activity obtained. DFT calculations revealed that an electronic interaction occurs at the Pt/Pd–Au interface, accompanied by the charge transfer and redistribution of the d-bands of Au, Pt, and Pd. This translated in a shift in the d-bands of Pd and Pt, indicating that hydrogen is adsorbed on all Pd sites with a marginal difference compared to Pt, leading to better surface coverage and most importantly to the barrier-free surface diffusion and recombination. Subsequently, the Pd performance is improved in comparison with that of Pt in the presence of Au.

A more extensive investigation of noble-metal-based electrocatalysts in combination with transition metals for use in fuel cells is recommended for future research. Research into 0% noble-metal electrocatalysts (with the highest performance) is also of interest. Results obtained by the modification effect of electrocatalysts combined with theoretical investigation (obtained in this work) could form a solid basis for the in-depth understanding of material interactions with fuel and help in the design and engineering of new powerful low-cost electrocatalysts.

List of publications

- **A. Laghrissi**, M. Es-Souni; ***A TiN@ Au-NR Plasmonic Structure with Tunable Surface Plasmon Resonance Depending on TiN to Au Thickness Ratio***. Plasmonics. https://doi.org/10.1007/s11468-020-01254-z
- H. Bakhti, **A. Laghrissi**, A. Roth, L. Azrar, M. Es-Souni; ***Nanomechanical characterization and modeling of anodized porous aluminum oxide thin films with photografted anti-biofouling polymer brushes on their pore walls***. Applied Nanoscience. https://doi.org/10.1007/s13204-020-01338-6
- N. Berger, **A. Laghrissi**, Y. Yan Tay, T. Sritharan, J. Fiutowski, H.-G. Rubahn, M. Es-Souni: ***Formation of Si Nanorods and Discrete Nanophases by Axial Diffusion of Si from Substrate into Au and AuPt Nanoalloy Nanorods***. Nanomaterials. https://doi.org/10.3390/nano10010068
- **A. Laghrissi**, M. Es-Souni: ***Porous PtPd Alloy Nanotubes. Towards High Performance Electrocatalysts With Low Pt-Loading***. Catalysis Science & Technology. https://doi.org/10.1039/C9CY01145E
- E. Wassel, M. Es-Souni, M. Dietze, A. Laghrissi, M. Es-Souni: ***A Non-Fouling Multilayer Structure Based On LAPONITE®/PEG-Brushes Showing High Stiffness and Hardness***. Progress in Organic Coatings. https://doi.org/10.1016/j.porgcoat.2019.03.036
- M. Es-Souni, E. Wassel, M. Dietze, **A. Laghrissi**, F. Klöhn, T. Weyrich, M. Es-Souni: ***Processing Of Nanotubes On Niti-Shape Memory Alloys And Their Modification With Photografted Anti-Adhesive Polymer Brushes. Towards smart implant surfaces***. Materials & Design. https://doi.org/10.1016/j.matdes.2019.108031
- **A. Laghrissi**, M. Es-Souni: ***Layered Au-Pd-Au Nanorod Catalysts: Pd-Layer Thickness Effects On Catalyst Performance***. International Journal of Hydrogen Energy. https://doi.org/10.1016/j.ijhydene.2019.04.105
- E. Wassel, M. Es-Souni, **A. Laghrissi**, A. Roth, M. Dietze, M. Es-Souni: **Scratch Resistant Non-Fouling Surfaces Via Grafting Non-Fouling Polymers On The Pore Walls Of Supported Porous Oxide Structures.** Materials & Design. https://doi.org/10.1016/j.matdes.2018.107542
- **A. Laghrissi**, C.-H. Solterbeck, D. Schopf, M. Es-Souni: ***Noble Metal NPs And Nanoalloys By Sonochemistry Directly Processed On Nanocarbon And TiN Substrates From Aqueous Solutions***. Ultrasonics – Sonochemistry. https://doi.org/10.1016/j.ultsonch.2018.10.034
- **A. Laghrissi**, E. Salmani, H. Ez-Zahraouy, A. Benyoussef: ***Ab Initio, Theoretical And Monte Carlo Approaches For The Magnetocaloric Effect In DyNi4Si***. Journal of Magnetism and Magnetic Materials. https://doi.org/10.1016/j.jmmm.2016.04.009

Declaration of Authorship / Eidesstattliche Erklärung

I hereby declare that the present work was independently written according to the content and form, apart from the advice from my supervisor, and that no sources and aids other than those specified therein were used. Thus far, I assure you that neither I nor anyone else has submitted this work at any other point as part of a doctoral examination procedure. Parts of this work have already been published in scientific journals or have been submitted for publication. I also declare that I have not attempted a Doctoral degree before. The elaboration was created in compliance with the Rules of Good Scientific Practice of the German Research Foundation. I further declare that no academic degree has ever been withdrawn.

Kiel, 20.11.2020

Ayoub Laghrissi